Experimental Study of Impact and Evaporation of a Droplet on a Solid Surface: Self-Assembly of Colloidal Particles and Bouncing Droplets

Submitted in partial fulfilment of the requirements
of the degree of

Doctor of Philosophy

of the

Indian Institute of Technology Bombay, India
and
Monash University, Australia

by

Laxman Kumar Malla
IITB ID: 154104004
Monash ID: 27330931

Supervisors:

Prof. Rajneesh Bhardwaj (IIT Bombay)
Prof. Adrian Neild (Monash University)

The course of study for this award was developed jointly by
Monash University, Australia and the Indian Institute of Technology Bombay, India
and was given academic recognition by each of them.
The programme was administered by The IITB-Monash Research Academy.

2020

Declaration

I declare that this written submission represents my ideas in my own words and where others' ideas or words have been included, I have adequately cited and referenced the original sources. I also declare that I have adhered to all principles of academic honesty and integrity and have not misrepresented or fabricated or falsified any idea/data/fact/source in my submission. I understand that any violation of the above will be cause for disciplinary action by the Institute and can also evoke penal action from the sources which have thus not been properly cited or from whom proper permission has not been taken when needed.

Notice 1

Under the Copyright Act 1968, this thesis must be used only under the normal conditions of scholarly fair dealing. In particular no results or conclusions should be extracted from it, nor should it be copied or closely paraphrased in whole or in part without the written consent of the author. Proper written acknowledgement should be made for any assistance obtained from this thesis.

Notice 2

I certify that I have made all reasonable efforts to secure copyright permissions for third-party content included in this thesis and have not knowingly added copyright content to my work without the owner's permission.

Laxman Kumar Malla
IITB ID: 154104004
Monash ID: 27330931

Acknowledgements

I express my sincere gratitude to my guide at IIT Bombay, Prof. Rajneesh Bhardwaj, for his endless support during my Ph.D. study. He is my primary resource of getting all my research problems completed, and I owe him for his patience, motivation, and insightful discussions provided in my research. Many thanks to my Ph.D. co-guide from Monash University, Prof. Adrian Neild. I feel privileged to be associated with him for his continuous guidance, feedback, and knowledge. My Ph.D. study has been possible for constant encouragement from both the guides, and I am indebted to them for the rest of my life.

Besides my guides, I would like to thank my Ph.D. research progress committee members, Prof. Mainak Majumder from Monash University and Prof. Janani Srree Muralidharan from IIT Bombay for their valuable inputs and advice provided during the annual progress seminars. I gratefully acknowledge the four years of funding received towards my Ph.D. fellowship from IITB-Monash Research Academy.

My heartfelt thanks to my senior lab mate, Dr. Nagesh D. Patil, and fellow lab mates, Manish, Prathamesh, and Sagar, who were always there to help me out during the difficulties in my experiments and solving constant queries. My special thanks to senior lab mates Dr. Atul Soti, Dr. Anup Kundu, and Dr. Hemanshul Garg and fellow lab mate, Rahul, for always giving moral support and being compassionate. Thanks to all for being a good support system.

I am grateful to my parents, sister, and brother-in-law, and his family for their unconditional love and affection. I thank them for understanding my goals and aspirations and always standing by my side. I wish my elder brother could have lived to see my wedding and the completion of the Ph.D. The best outcome from the past five years of Ph.D. is finding my best friend and soulmate, my beautiful wife. She is always there to instill confidence in me. I thank her and her family for believing in me and my intellect. In the end, I am thankful to all my teachers who have made me capable of reaching this point in life.

Abstract

Understanding evaporation of a droplet containing colloidal particles is useful in many technical applications such as inkjet printing, manufacturing of bioassays, medical diagnostic techniques, patterning surfaces by colloidal particles in photonics, fabrication of electronics circuit, conductive coatings, porous films, etc. In context of impact of pure liquid droplets on a microtextured surface, potential applications are in designing self-cleaning, and low drag surfaces, etc. The present thesis investigates the coupled transport phenomena of these two problems.

First, the profile and morphology of the ring-like deposits obtained after evaporation of a sessile water droplet containing polystyrene colloidal particles on a hydrophilic glass substrate is investigated experimentally. In particular, the coupled effect of particle size and concentration are studied. The deposits were qualitatively visualized under an optical microscope and profile of the ring was measured by an optical profilometer. The profile of the ring resembles a partial torus-like shape for all cases of particles size and concentration. A regime map is plotted to classify discontinuous monolayer, continuous monolayer and multiple layers formed in the ring on particles concentration-particle size plane. Both the width and height of the ring are measured and show that they scale with particle concentration by a power law for the rings of multiple layers of the particles. The effect of the interaction of growing deposit with shrinking free surface on ring dimensions and profile is briefly discussed. Evaporation of a water droplet containing graphene nanoplatelets on the non-heated glass substrate is also investigated to study the effect of the graphene nanoplatelets concentration.

Further, the pattern and profile of dried colloidal deposit formed on a non-uniformly heated glass substrate is investigated experimentally. In particular, the effects of particles size and temperature gradient across the substrate are investigated. The temperature gradient was imposed using Peltier coolers, and side visualization, infrared thermography, optical microscopy, and optical profilometry were employed to collect the data. On a uniformly heated substrate, ring with an inner deposit is obtained, attributed to axisymmetric Marangoni recirculation and consistent with previous reports. However, the dimensions of the ring formed on a non-uniformly heated substrate are significantly different on the hot and cold side of the substrate. In case of smaller particle size, the contact line of hot side de-

pins and together with twin asymmetric Marangoni recirculations, it results in a larger ring width on the cold side. In contrast, the contact line remains pinned in case of larger particles, and the twin asymmetric Marangoni recirculations advect more particles on the hot side, resulting in a larger ring width at the hot side. A larger gradient significantly increases or decreases the ring width depending on the particle size, due to a stronger recirculation.

Second, the impact dynamics of a microliter water droplet on a microgrooved surface is investigated. The surface is fabricated using photolithography, and highspeed visualization is employed to record the time-varying droplet shapes in the transverse and longitudinal directions. The effect of the pitch of the grooved surface and Weber number on the droplet dynamics and impact outcome are studied. At low pitch and Weber number, the maximum droplet spreading is found to be greater in the longitudinal direction than the transverse direction to the grooves. The preferential spreading inversely scales with the pitch at a given Weber number. In this case, the outcome is no bouncing; however, this changes at larger pitch or Weber number. Under these conditions, the following outcomes are obtained as a function of the pitch and Weber number: droplet completely bounces off the surface, bouncing occurs with droplet breakup, or no bouncing because of a Cassie to Wenzel wetting transition. In later two cases, the liquid partially or completely penetrates the grooves beneath the droplet as a result of the wetting transition. The droplet breakup results alongside bouncing, while the Cassie to Wenzel wetting transition suppresses the bouncing. These outcomes are demarcated on the Weber number-dimensionless pitch plane, and the proposed regime map suggests the existence of a critical Weber number or pitch for the transition from one regime to the other. Complete bouncing and Bouncing with droplet breakup are quantified by plotting the coefficient of restitution of the bouncing droplet and the volume of the daughter droplet left on the surface, respectively. The critical Weber number needed for the transition from complete bouncing to bouncing with droplet breakup is estimated using an existing mathematical model and is compared with the measurements. The comparison is good and provides insights into the mechanism of liquid penetration into the grooves. The present results on microgrooved surfaces are compared with published results on micropillared surfaces in order to assess the water-repelling properties of the two surfaces.

Contents

List of Figures

List of Tables

Chapter 1

Introduction

1.1 Applications

The interfacial phenomena play a pivotal role in many technical applications. Applications include liquid manipulation for microfluidics and lab-on-chips, inkjet printing [25], manufacturing of plastic and flexible electronics [26, 27] electronic circuits [28], organic thin-film transistors [29], depositing proteins and DNA [30, 31], surface coatings [32], rapid spray cooling of hot surfaces such as turbine blades, spray deposition [33], plasma spraying, and crop spraying [34]. Many authors have shown interest in the study of the superhydrophobic surfaces because of their potential applications in low drag, self-cleaning, and electrowetting properties. In nature, several animals and plants utilize isotropic and anisotropic textured surfaces for drag reduction and self-cleaning. Examples include lotus leaf, rice leaf [35], anisotropic textures on shark skin or butterfly wing for low-drag locomotion, etc. A lotus leaf exhibits microscale isotropic structures on its surface for lower wettability [36]. Outside the natural world, anisotropic wettability can be utilized to provide directional fluid transport in microfluidics. The textured surfaces can be used in engineering self-cleaning, low drag, and de-icing surfaces. The interfacial phenomena revolve mainly around two areas of study that is evaporation of a sessile droplet on a solid surface, and a droplet impact on a solid surface. Some of the applications of these two areas of study are shown in Figure 1.1. In the following section, the physics of interfaces, sessile droplet evaporation, and droplet impact dynamics on a solid surface are explained in detail.

1.2 Basic concepts

1.2.1 Interfaces

The interface is a geometrical surface between two fluid domains without any thickness and roughness. At the interface, due to the dissymmetry in the molecular interactions be-

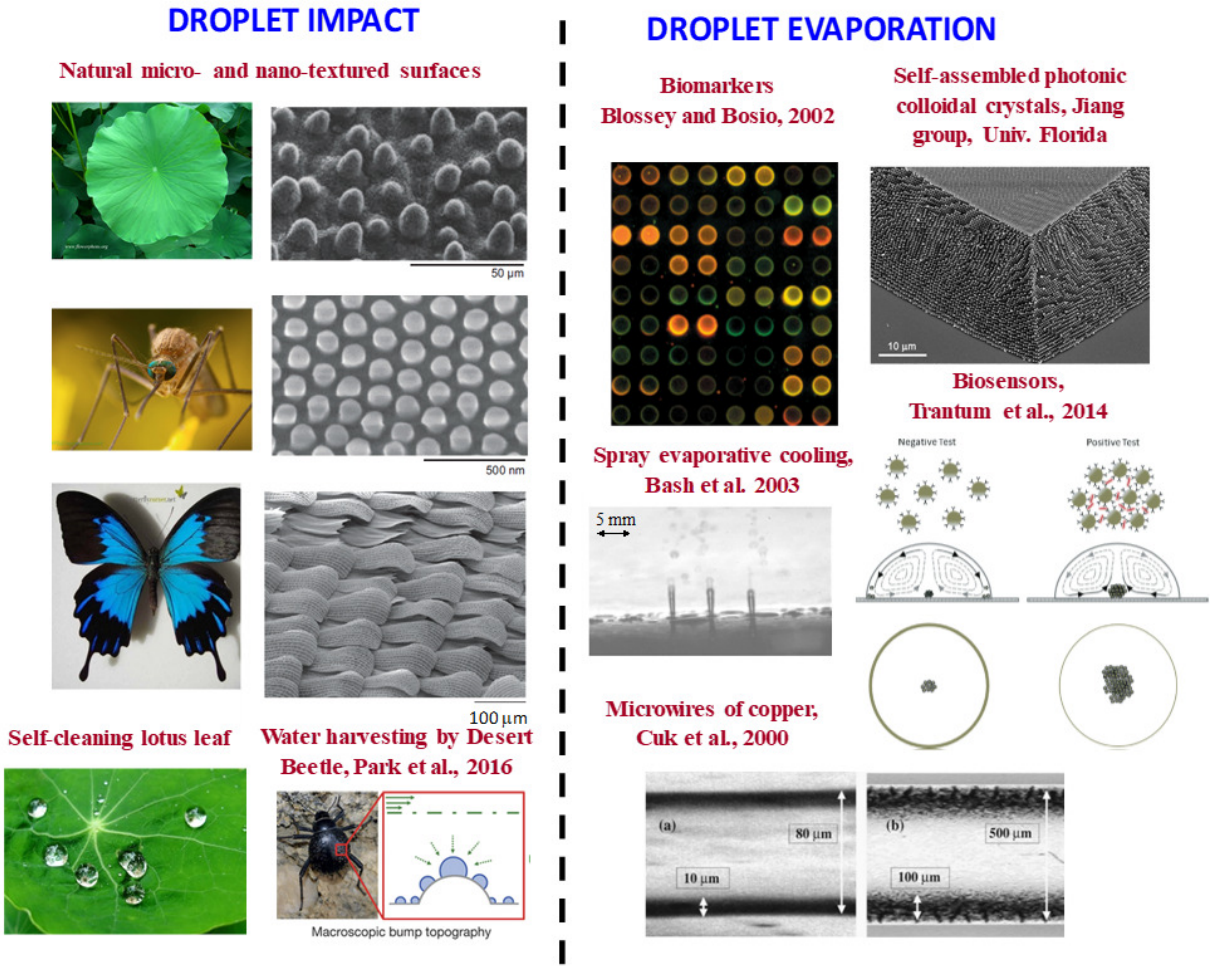

Figure 1.1: Present thesis considers two much-studied major areas of research in the interfacial phenomena shown on left and right. (left) Textured surfaces in nature and their manifestations in plants and animals. The image on the left show plant/animal and corresponding SEM is shown on the right. Lotus leaf keep itself clean i.e. self-cleaning due to microtextures on its surface. A mosquito maintains its vision by de-wetting properties on the surface of its eye. Nano-pillars shown in the right frame confirm this finding (right frame). The skin of a butterfly wing exhibit anisotropy in the microtextures, which helps them faster locomotion. The SEM shown are taken from Refs. [1, 2]. (right) Technical applications of droplet evaporation on a solid surface. Biologists routinely print bioassays and would like to avoid coffee-ring pattern. Self-assembled colloidal particles are useful in photonics. Evaporating droplets are used as vehicles to use as biosensors as well as manufacturing thin copper microwires.

tween the two fluids, there are unbalanced forces on the molecules at the interface. The surface molecules are pulled inward by their neighboring molecules, which gives rise to surface tension at the interface. The surface tension is defined as the total surface energy per unit surface area, and its unit is J/m^2 or N/m. Surface tension can be measured by calibration with another known force, for example, using pressure force in the bubble pressure method, using capillary force in the Wilhelmy plate method, or using gravity in the pendant drop method [19]. Surface tension influences the shape of the interface, where the liquid tries to minimize the surface area to maintain the lowest surface energy. For example, a liquid droplet or bubble maintains a spherical shape, since a geometrical sphere has the smallest surface area for a given volume.

The fundamental law, which governs the interfaces is Laplace's law. According to the Laplace law, the pressure difference across a curved interface is given as [34],

$$\Delta P = \gamma H \tag{1.1}$$

where, ΔP, γ, and H are the pressure difference, surface tension, and the interface mean curvature, respectively. The mean curvature is defined as follows,

$$H = \frac{1}{2}(\kappa_1 + \kappa_2) = \frac{1}{2}(\frac{1}{R_1} + \frac{1}{R_2}) \tag{1.2}$$

where, κ_1, and κ_2 are the two principal (maximum and minimum) curvatures and R_1 and R_2 are two principal radii of curvatures. For example, consider a sphere of radius R, both the two principal curvatures are $1/R$, and therefore, the mean curvature is also $1/R$. Whereas, for a cylinder of base radius R, the maximum curvature is R, and the minimum curvature is zero, therefore, the mean curvature is $1/2R$. Similarly, for a plane surface, the two curvatures are zero, and hence the mean curvature is zero.

A liquid spreads differently on different solid surfaces depending on the surface properties of the solid, and the liquid as well as the properties of the surrounding fluid medium. When a liquid droplet rests on a solid surface in another fluid environment, then the contact line of the droplet where the three-phase that is a solid surface, liquid droplet, and the atmospheric fluid interacts is called the triple contact line. A static droplet on an ideal solid surface is characterized by the contact angle that is defined as the angle, which the tangent to the drop surface at the contact line subtends on the horizontal surface as shown in Figure 1.2. Surface tension represents a tangential force exerted on an interface. Due to the presence of a fluid on the triple contact line (Figure 1.2), the resultant of the different forces must be zero at equilibrium. Therefore, the Young's law to calculate the contact angle (θ_E) of a sessile drop is given by the relation [34],

$$cos\theta_E = \frac{\gamma_{SG} - \gamma_{SL}}{\gamma_{LG}} \tag{1.3}$$

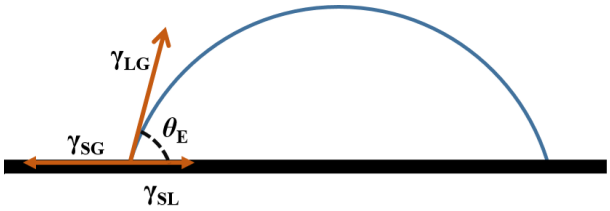

Figure 1.2: A sessile droplet on a solid surface with associated surface forces.

The shape of the drop surface on the solid substrate depends on the surface energy of the fluid-fluid interface and two fluid-solid interfaces. The spreading parameter, S, that is used to define whether a drop has wetted a surface or not is represented by the following expression [34],

$$S = \gamma_{SG} - (\gamma_{SL} + \gamma_{LG}) \tag{1.4}$$

where, γ_{SG} is the surface energy per unit surface area of the dry solid surface, γ_{SL} is the surface energy per unit surface area of the wetted solid surface, and γ_{LG} is the surface energy per unit surface area of the interface between the liquid and surrounding fluid medium. If $S > 0$, then the drop is said to wet the surface totally, and if $S < 0$, then the drop is said to wet the surface partially. In totally wetting case, the contact angle is zero, and in the partially wetting case, the contact angle can take values from 0° to 180°. If $\theta_E < 90°$, then the surface is hydrophilic, and if $\theta_E > 90°$, then the surface is hydrophobic.

1.2.2 Droplet evaporation dynamics

The evaporation of a sessile droplet on a solid substrate is a coupled transport phenomenon affected by many factors such as conduction in the substrate, convection inside the droplet, liquid-vapor diffusion into the ambient, and receding of the contact line. The evaporation is driven by the diffusion of liquid vapor into the ambient. If the surrounding gaseous medium is saturated with the liquid-vapor, then evaporation of the droplet liquid does not occur. For example, a water droplet does not evaporate at the dew point temperature for water. Generally, the droplet is assumed to be a spherical cap that is the droplet wetted radius is less than the capillary length (κ^{-1}) (explained in detail in section 1.2.4). For instance, κ^{-1} for a water droplet is around 2.7 mm. The initial conditions considered in a study are the droplet initial wetted diameter, initial height, initial contact angle, and the substrate condition that is whether it is at the ambient or heated condition.

The contact angle of the droplet is determined by the Young's relation, mentioned earlier. The mass flux of the evaporation is largest near the contact line [37, 38], as shown in Figure 1.6 (a), and the contact line is pinned due to the contact angle hysteresis, which induces an outward radial flow inside the droplet. Due to the small length scales of the

microliter droplets, Laplace forces govern the liquid-gas interface, and the receding of the contact line may occur during evaporation, according to the Young-Dupre's law [34]. The evaporation of a sessile droplet on a substrate can be observed in different modes called as constant contact radius (CCR), constant contact angle (CCA) mode, or mixed mode, as shown in Figure 1.3 (a). In CCR mode, the contact line remains pinned, and the contact angle decreases with time during evaporation. In CCA mode, the contact line depins and recedes with time with a constant contact angle. Whereas, in the mixed mode, both the contact radius and contact angle decreases with time. The variation of the droplet parameters with time in CCR and CCA mode is shown schematically in Figure 1.3 (b). For a hydrophilic case such as water on a glass, the contact line is pinned to the surface for a maximum time of the evaporation, and the height and the contact angle of the droplet decrease due to the evaporation. Towards the end of the drying process, depinning of the contact line occurs and thereafter, CCA mode of evaporation occurs. Generally, on a hydrophobic surface, the CCA mode of evaporation is observed.

1.2.3 Self assembly of colloidal particles

Self-assembly of colloidal particles in an evaporating sessile droplet on a solid surface is a much-studied problem in interface science in the last two decades [39] and is also known as the coffee-ring effect. Some of the examples of the self-assembly of colloidal deposits through coffee-ring effect published in recent works are shown in Figure 1.4. A schematic of a sessile droplet containing colloidal particles is shown in Figure 1.5(a). As pointed out by Goldstein [40] recently, Brown [41] was the first researcher to visualize the advecting particles towards the contact line in an evaporating droplet on a solid surface. In a seminal paper, Deegan et al. [37] explained that the capillary flow inside the droplet (bulk flow) caused by non-uniform evaporation of a sessile droplet is the reason of formation of a ring-like colloidal deposit after the evaporation. The evaporation mass flux is the largest near the contact line, and the bulk flow is radially outward that is towards the contact line [37], as shown in a schematic in Figure 1.5(b). This flow advects most of the suspended colloidal particles to the contact line, consequently forming a ring-like deposit at the contact line (Figure 1.6 (a)).

It is this transport phenomenon and the nature of the pinning of the contact line, which determines the shape of the final deposit. The accumulation of suspended particles near the contact line creates an energy barrier for receding of the contact line, which leads to pinning of the contact line and thus a ring of particles forms at the edge of the droplet [42]. Also, a finite distance exists between the pinned contact line and the boundary of the coffee-ring [43]. The coffee-ring effect is pivotal to designing several technical applications. As discussed in previous reviews [44, 45], applications include inkjet printing, manufactur-

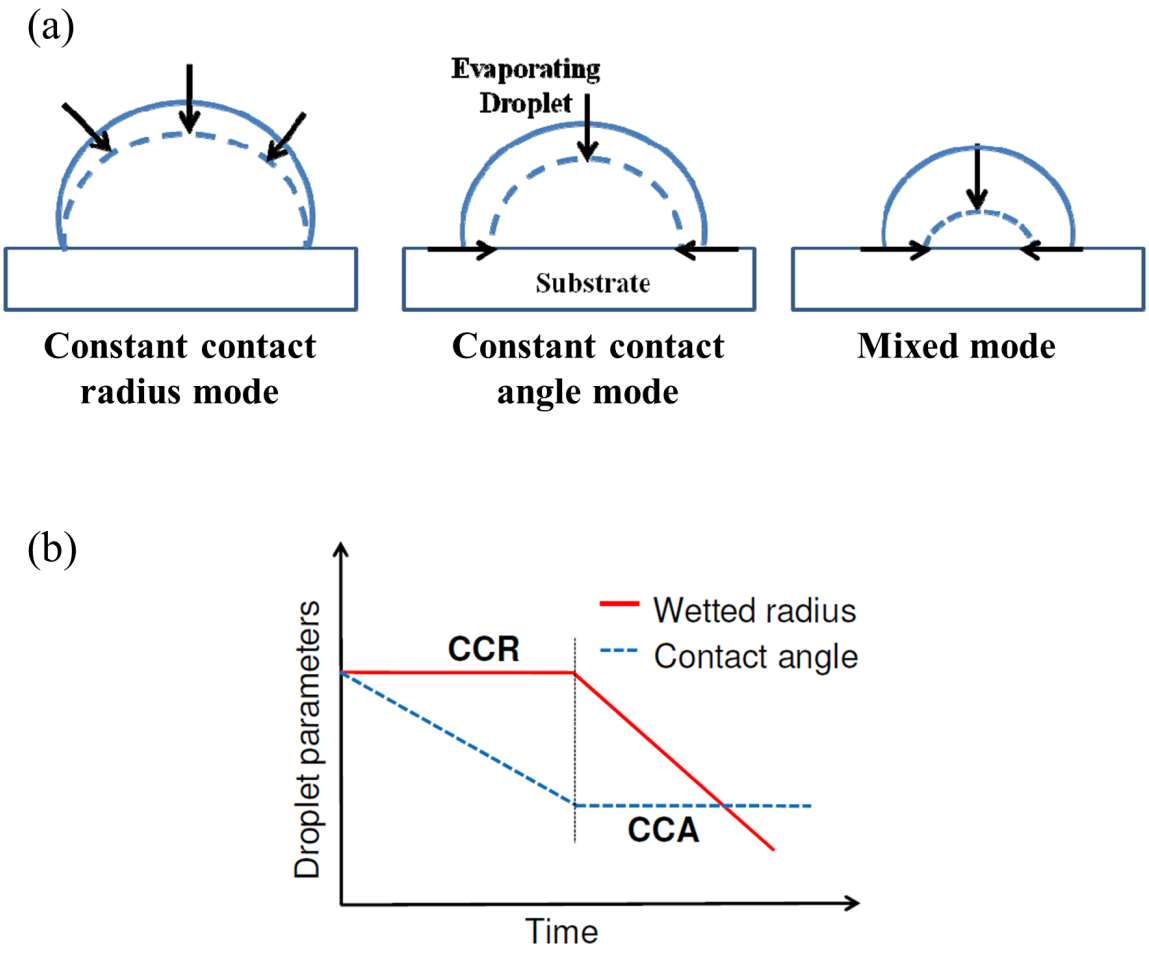

Figure 1.3: (a) Schematic of droplet evaporation modes on a solid surface: Constant contact radius (CCR), constant contact angle (CCA), and mixed mode. Image is taken from [3]. (b) Variation of the droplet wetted radius and contact angle with time during evaporation of sessile droplet on a solid surface. Image is taken from [3].

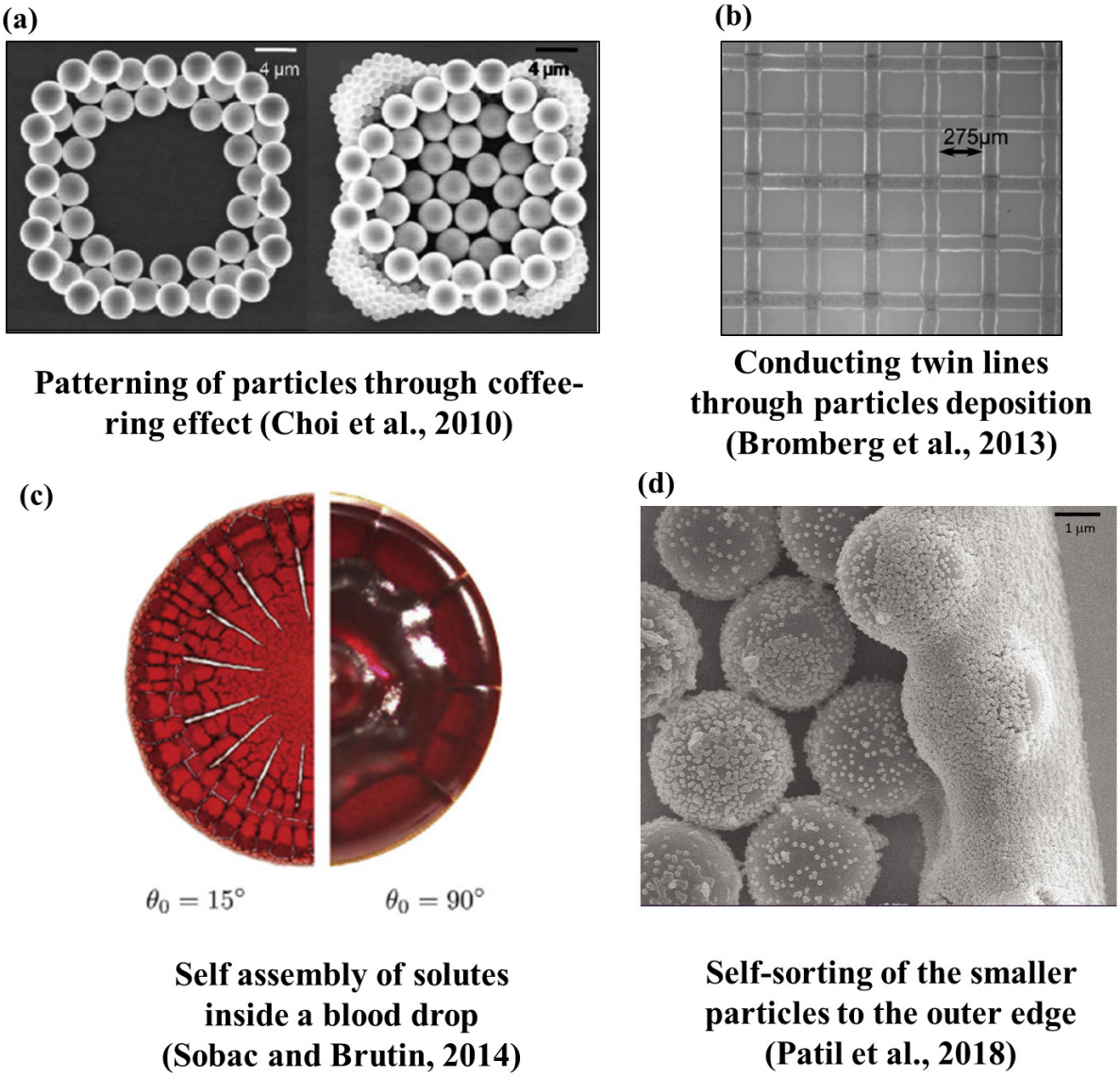

Figure 1.4: Some of the examples of self assembly of colloidal particles through coffee-ring effect (a) Patterns formed with particles of diameters (1 and 3 μm). Adapted from Ref. [4](b) Patterned grid of conducting twin lines of silver nanoparticles. Adapted from Ref. [5] (c) Dried deposits of a blood drop on substrates of different wettabilities. Adapted from Ref. [6] (d) Self-sorting of smaller particles to the outer edge in the evaporation of a water droplet containing bidispersed particles (0.1 and 3 μm). Adapted from Ref. [7]

ing of bioassays, medical diagnostic techniques, patterning surfaces by colloidal particles in photonics, fabrication of electronics circuit, conductive coatings, porous films, etc. The final deposit pattern and shape may be crucial to design an application. For instance, a uniform deposit is desired in inkjet printing, as compared to a ring-like deposit.

The non-uniform evaporation flux on the liquid-air interface creates a temperature gradient over the interface since the liquid-gas interface cools non-uniformly due to the latent heat of evaporation. The temperature gradient, in turn, creates a surface tension gradient on the interface leading to an axisymmetric Marangoni recirculation inside the droplet (Figure 1.5(c)). This phenomenon is observed mostly in the evaporation of volatile liquids (alcohol-based suspensions). The resultant deposit shows suppression of the coffee-ring as observed after the evaporation of a microliter octane droplet containing PMMA particles (1 g/100 mL) on a glass coated with perfluorolauric acid [46] and after the evaporation of nanoliter isopropanol droplet containing polystyrene spheres on a PDMS substrate forming a central bump pattern [32]. The suppression of the coffee-ring also occurs on substrates having smaller contact angle hysteresis (CAH), where depinning of the contact line occurs [47]. Generally, on a hydrophobic surface, a ring-like inner deposit is observed due to initial depinning and later pinning of the contact line [48]. The radius of such deposit is smaller than the initial wetted radius [48].

The Marangoni recirculation inside the droplet can also be established in non-volatile liquids, such as water, by heating the substrate. Due to the heated substrate, the temperature of the interface near the contact line will be higher than the temperature of the interface at droplet apex. Therefore, a temperature gradient is established on the interface, which in turn invokes the Marangoni recirculation inside the droplet bringing the colloidal particles towards the center of the wetted region [9, 20, 49], as shown schematically in Figure 1.6 (b). The evaporation time also decreases with an increase in the substrate temperature due to the increase in the conduction heat transfer from the substrate. The conduction heat transfer to the droplet may cease due to bubble formation in between the liquid droplet and the substrate due to a large increase in the temperature until Leidenfrost point, where a thin vapor film is formed in between the droplet and substrate decreasing the conduction heat transfer and increasing the evaporation time [50].

1.2.4 Droplet impact dynamics

On a solid surface, an impacting droplet spreads under the influence of kinetic energy enabling a large deformation of the liquid-air interface. Consider a droplet of diameter, D_0, with initial impact velocity, U_0, impacting on a flat solid surface with the help of gravity, g, as shown in Figure 1.7. During spreading of the droplet, the kinetic energy gets converted to the potential energy due to the surface tension and viscous energy [33]. The advancing

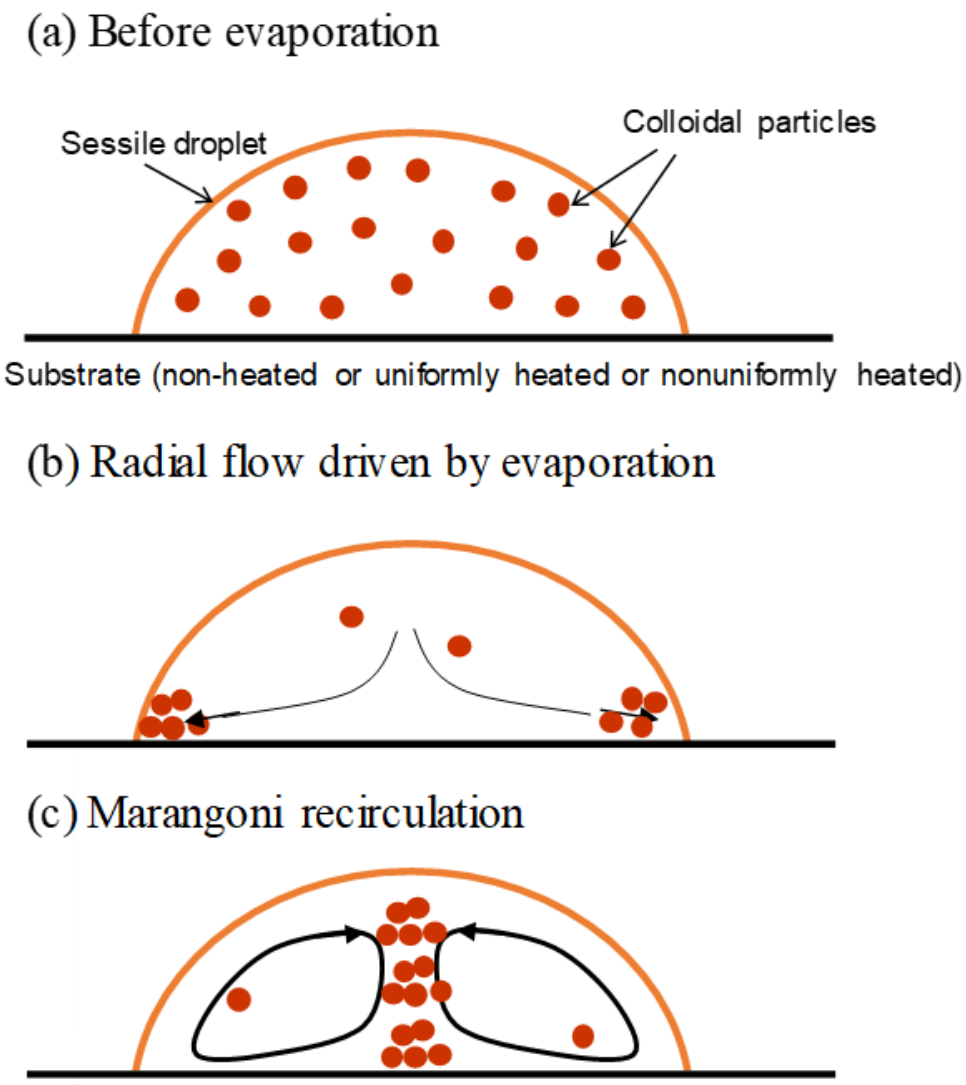

Figure 1.5: (a) Schematic of a sessile droplet loaded with colloidal particles on a solid surface. (b) Radially outward bulk flow advects all the particles to form a ring-like deposit. (c) Axisymmetric Marangoni flow recirculation in the presence of thermal gradient across the liquid-gas interface. The recirculation brings the particles from the contact line region to near the axis of symmetry. Adapted from Bhardwaj et al. [8]. Copyright, 2010, American Chemical Society.

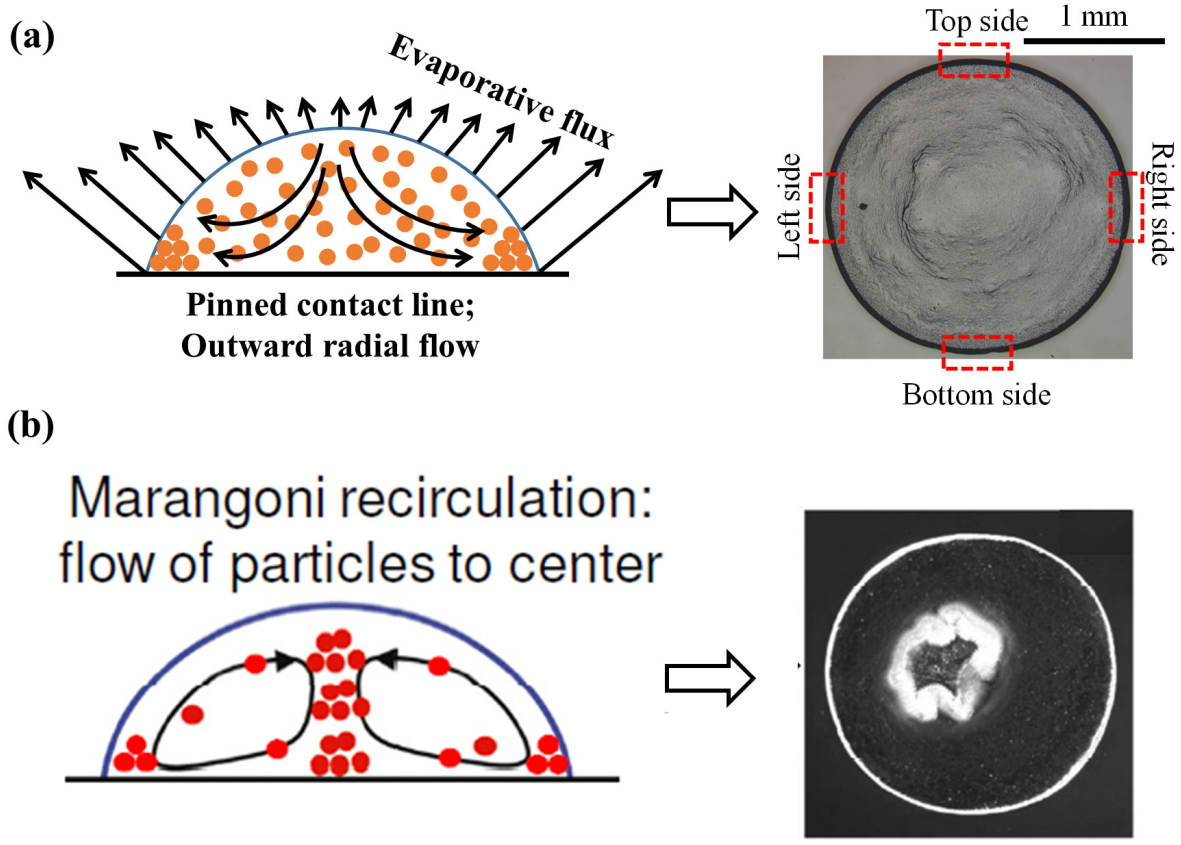

Figure 1.6: (a)Schematic representation of the evaporation-induced outward radial fluid flow and ring-like deposit on a hydrophilic substrate with a pinned contact line of the sessile droplet. The profile of the ring is measured at four locations (shown as a red dashed square) in order to get an averaged profile. (b) Marangoni recirculation inside the droplet bringing the particles towards the center of the wetted region [8, 9]. Image is adapted from Ref. [3, 8].

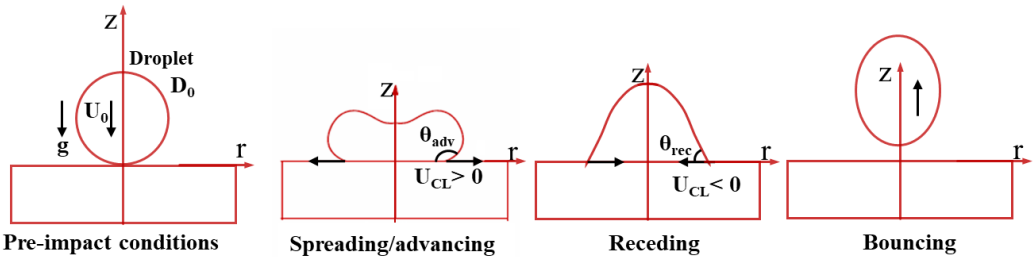

Figure 1.7: Schematic of the droplet impact dynamics to be studied. Image is taken from Ref. [3].

of the contact line during spreading, with velocity, U_{CL} is aided by the momentum or inertia force. The increase of the surface energy in comparison to the inertial energy impedes the droplet from spreading. The impending action results in the inward movement of the liquid in the axial direction, increasing the droplet height. The droplet bouncing occurs (as shown schematically in Figure 1.7) if the total energy of the droplet at the instance of the maximum receding exceeds the combined initial surface energy and gravitational energy [51, 52]. For instance, the impact of a water droplet on a superhydrophobic flat surface at an impact velocity of 0.83 m/s bounces off the surface [10], as shown in Figure 1.8. The liquid viscosity and the internal vibrations inside droplet during lifts-off are the primary sources of dissipation for a bouncing droplet [53]. The droplet oscillates with spreading and receding of the contact line around the axis of symmetry until reaching the steady state. For instance, Fukai et al. [33] observed three cycles of oscillation of water droplet impacting a flat surface at Weber number (We) around 2 and Reynolds number (Re) of 100. The droplet spreading and receding in the first cycle is larger than the subsequent cycles of oscillation [54].

The contact line motion is governed by the dynamic contact angle and also affects the spreading process [11, 55]. The dynamic contact angle (θ) is the instantaneous angle, which the triple contact angle subtends during the contact line motion. The spreading occurs if the dynamic contact angle is larger than the advancing contact angle, $\theta > \theta_{adv}$ and $U_{CL} > 0$, as shown schematically in Figure 1.9. After reaching the maximum spreading, the droplet recoils due to the dominance of surface energy over kinetic energy and the contact line recedes in this process. The receding occurs if the dynamic contact angle (θ) is lesser than receding contact angle, $\theta < \theta_{rec}$, and $U_{CL} < 0$. The contact line is pinned if, $\theta_{rec} < \theta < \theta_{adv}$. The dynamic contact angle (instantaneous contact angle of the droplet) oscillates around θ_E with the same frequency and amplitude for all the cases of impact velocities [54]. The difference between θ_{adv} and θ_{rec} is defined as the contact angle hysteresis (CAH), and U_{CL} = 0. In a notable study, Bayer and Megaridis [12] reported that at the maximum spreading condition, the contact angle of a water droplet decreases from 125° to 40° in about 5 ms for impact on a Surevent PVDF (polyvinylidene fluoride) surface. This is due to the dy-

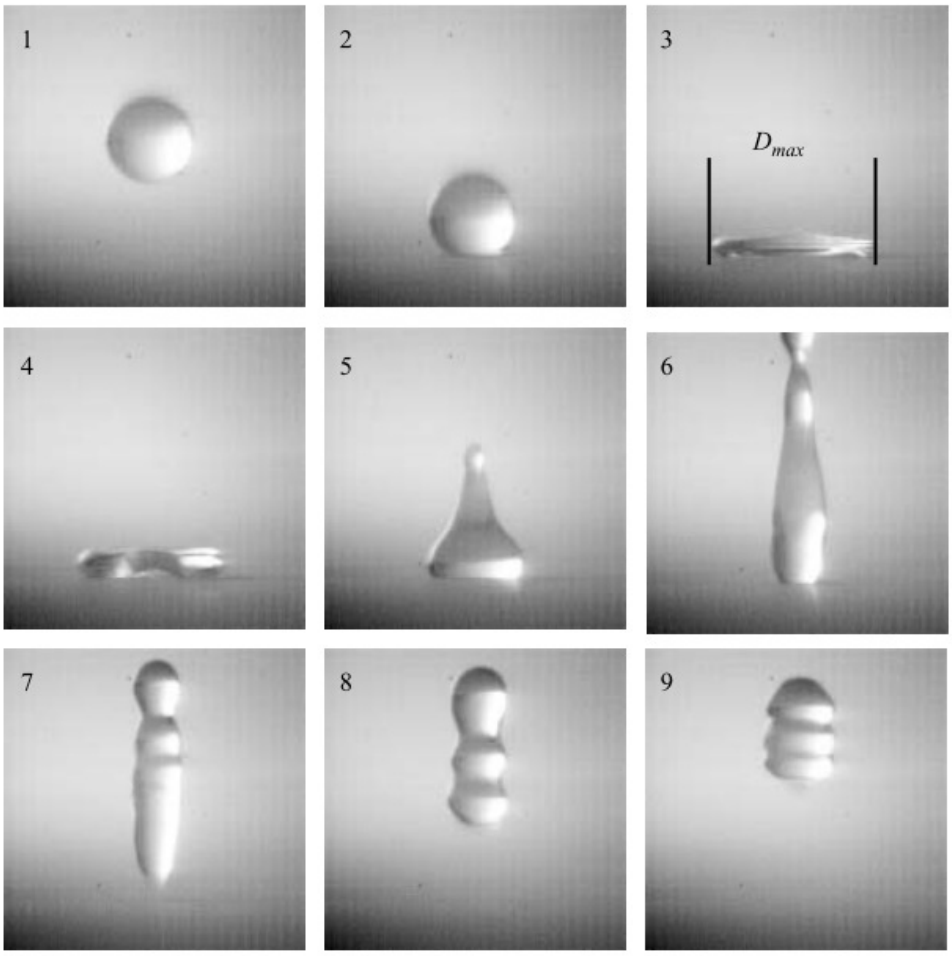

Figure 1.8: Bouncing of a water droplet of initial diameter 2.5 mm, on a superhydrophobic surface at impact velocity of 0.83 m/s. Images are taken from Clanet et al. [10].

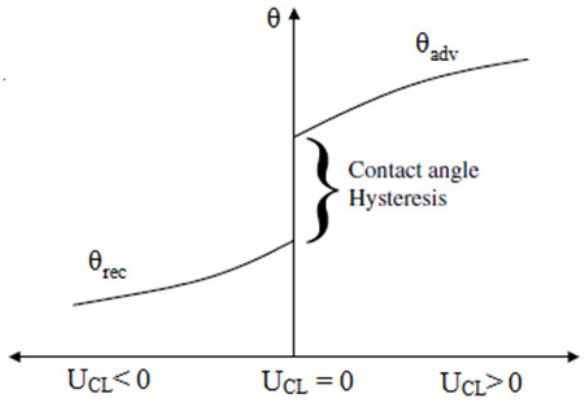

Figure 1.9: Relationship between the advancing contact angle, receding contact angle and the contact line velocity. Image is taken from Ref. [11].

namic contact angle hysteresis, as shown in Figure 1.10. CAH gives us an understanding of the surface wettability that is smaller the CAH, larger the surface hydrophobicity. CAH is negligible for a non-wettable surface ($\theta_E > 150°$).

When a droplet of diameter, D_0, with density, kinematic viscosity and surface tension, ρ, ν, and γ, respectively, impact on a solid surface with velocity, U_0, with speed of sound, C, thermal diffusivity, a, and acceleration due to gravity, g, then different time scales can be devised that are characteristics of convection, $t_{conv} = D_0/U_0$, compressibility effects, $t_{comp} = D_0/C$, thermal effects, $t_{therm} = {D_0}^2/a$, surface tension effects, $t_{surf} = \sqrt{\rho {D_0}^3/\gamma}$, viscous effects, $t_{vis} = {D_0}^2/\nu$, and gravitational effects, $t_{grav} = \sqrt{D_0/g}$ [56]. The ratio of these time scales yield five characteristics non-dimensional numbers, which govern the impact phenomena, for example, the Mach number, $Ma = t_{comp}/t_{conv} = U_0/C$, the Weber number, $We = (t_{surf}/t_{conv})^2 = (\rho {U_0}^2 D_0)/\gamma$, the Reynolds number, $Re = t_{vis}/t_{conv} = D_0 U_0/\nu$, the Peclet number, $Pe = t_{therm}/t_{conv} = D_0 U_0/a$, and the Froude number, $Fr = (t_{grav}/t_{conv})^2 = {U_0}^2/g D_0$. Another non-dimensional number, which shows the relative importance of surface tension effects and gravitational effects is the Bond number, $Bo = (t_{surf}/t_{grav})^2 = We/Fr$. The characteristic length below which the gravity effects can be neglected is called as capillary length (κ^{-1}), and is defined by the ratio of the Laplace pressure (γ/κ^{-1}) and the hydrostatic pressure ($\rho g \kappa^{-1}$). When the two pressures are of equal order, characterizing the shape of the droplets, then κ^{-1} is given by the following relation,

$$\kappa^{-1} = \sqrt{\frac{\gamma}{\rho g}} \tag{1.5}$$

If a droplet placed on a plane substrate having radius, R, less than κ^{-1}, then gravity is assumed to have negligible influence on the system, capillarity is the only influencing effect, and the droplet liquid and surrounding fluid interface is assumed to be a spherical cap. If R is greater than κ^{-1}, then the interface is flattened by the gravity and is considered as a

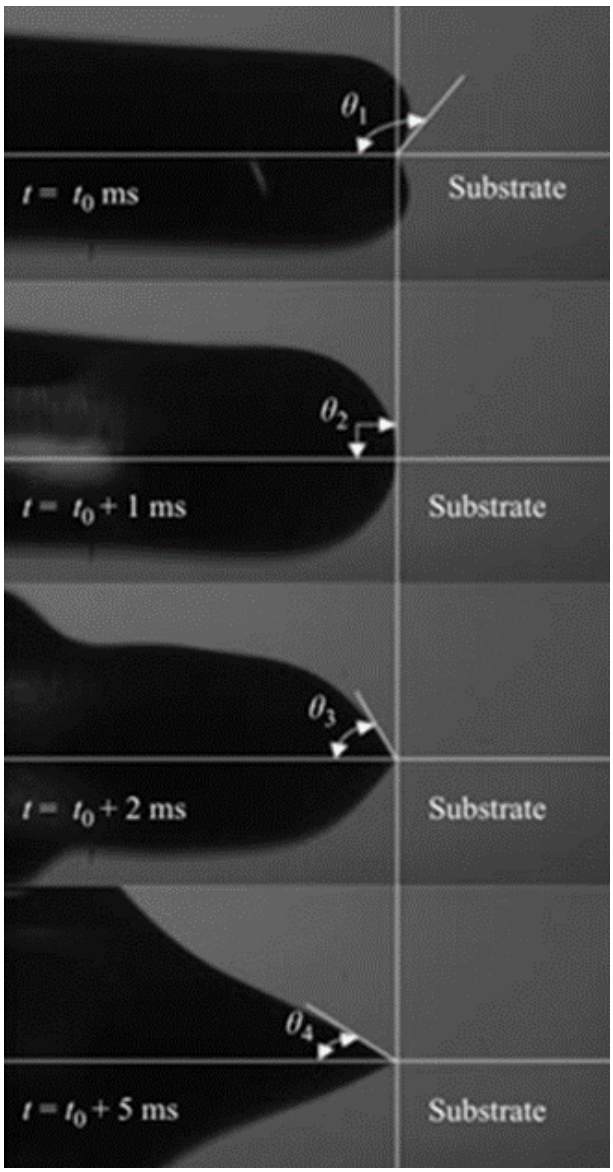

Figure 1.10: At $t = t_0$, the angle subtended by the droplet is advancing contact angle and at $t = t_0 + 5ms$, the angle is receding contact angle. The difference between them is called contact angle hysteresis. Image is taken from Ref. [12].

puddle.

The droplet impact dynamics is characterized mainly by the Weber number (We) and Ohnesorge number ($Z = t_{surf}/t_{vis} = \sqrt{We/Re^2} = \mu/\sqrt{(\rho\gamma D_0)}$) and Schiaffino and Sonin [23] proposed four impact regimes on $Z-We$ scale. These four regimes are categorized as follows, (a) inviscid, impact-driven in which spreading is aided by dynamic pressure and resisted by inertia (b) inviscid, capillary-driven in which spreading is aided by imbalance of capillary force at contact line and resisted by inertia; (c) highly viscous, capillary driven in which spreading is resisted by droplet viscosity; and (d) highly viscous, impact-driven in which spreading is resisted by viscous shear. If the impact velocity is much higher, sideways jetting of the liquid around the axis of symmetry and bubble formation at the center of the droplet due to air entrapment at the liquid cusp may occur [50].

The impact process is highly transient and the spreading time scales as D_0/U_0 [57]. For instance, the time taken for a millimeter size droplet with an impact velocity of 0.4 m/s, to spread on a hydrophilic surface is around 8 ms as shown in Figure 1.11 [11, 13]. Clanet et al. [10] reported a analytical model between the maximum spreading of the droplet and We of the impact, which is $D_{max} \sim D_0 We^{0.25}$. The impact on a heated solid surface increases the cyclic spreading and receding of the contact line and the maximum spreading of the droplet [58, 59]. The maximum spreading is also increased if the initial temperature of the droplet is increased, however, the period of the oscillation decreases due to decreased viscosity of the droplet liquid [11]. The maximum spreading can also be increased with the addition of surfactant in the droplet [57]. Pasandideh-Fard et al. [57] reported that if $We > \sqrt{Re}$, then the capillary effects can be neglected.

Superhydrophobic surfaces have attracted many studies in the recent past. The surfaces like Teflon, PDMS, SU8, are hydrophobic, whereas glass or other hydrophilic surfaces can be made hydrophobic through chemically depositing hydrophobic coatings. In nature, several plants and animals have textures on their surfaces at the micrometer level, which enable the surfaces to be superhydrophobic such that water droplets roll off the leaves (for example, lotus leaf, rice leaf) or do not stick to the skin (for example, butterfly wings). The microtextures on the surfaces also help in low drag locomotion, for example, shark skin. Mimicking the wettability of such plants/animals and recreating the superhydrophobic surfaces in labs has been the objective of numerous studies. Researchers have developed artificial patterned textures, which increases the roughness of the surfaces, thereby increasing the hydrophobicity. These surfaces are fabricated using techniques like photolithography and etching. Various microtextured surfaces studied for superhydrophobicity is shown in Figure 1.12. The contact angle on these microtextured surfaces generally, follow the Cassie-Baxter theory [60] or Wenzel theory [61]. Figure 1.13 shows the two states of the droplet on the microtextured surface. If the droplet liquid penetrates in between the roughness/textures of the surface, then it is said to be at Wenzel state, and the Wenzel

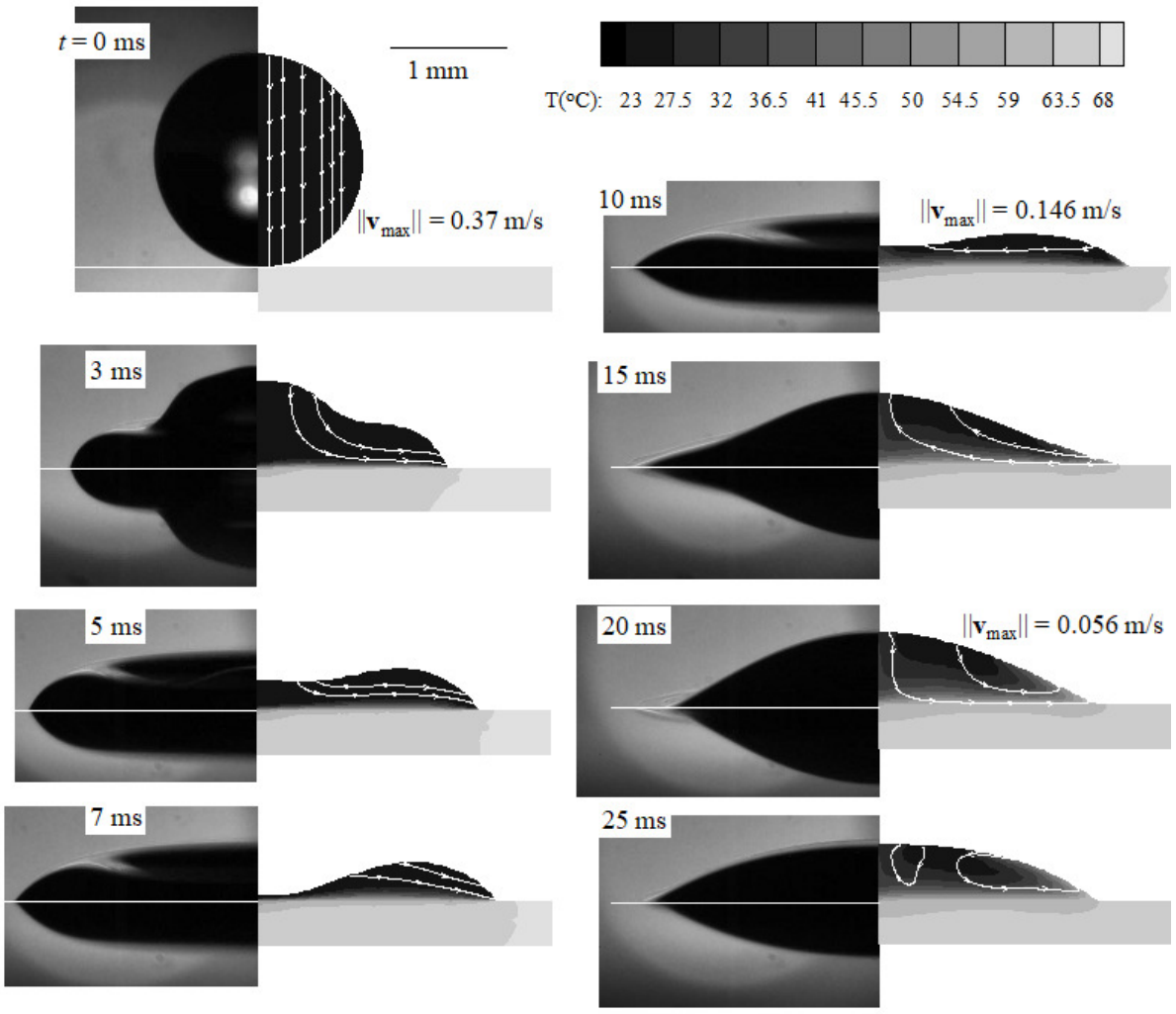

Figure 1.11: Dynamics of a 3μL isopropanol droplet impact on a heated fused silica substrate. Comparison of droplet shapes from experiments (left) with simulated streamlines and temperature field (right). Images are taken from Ref. [13].

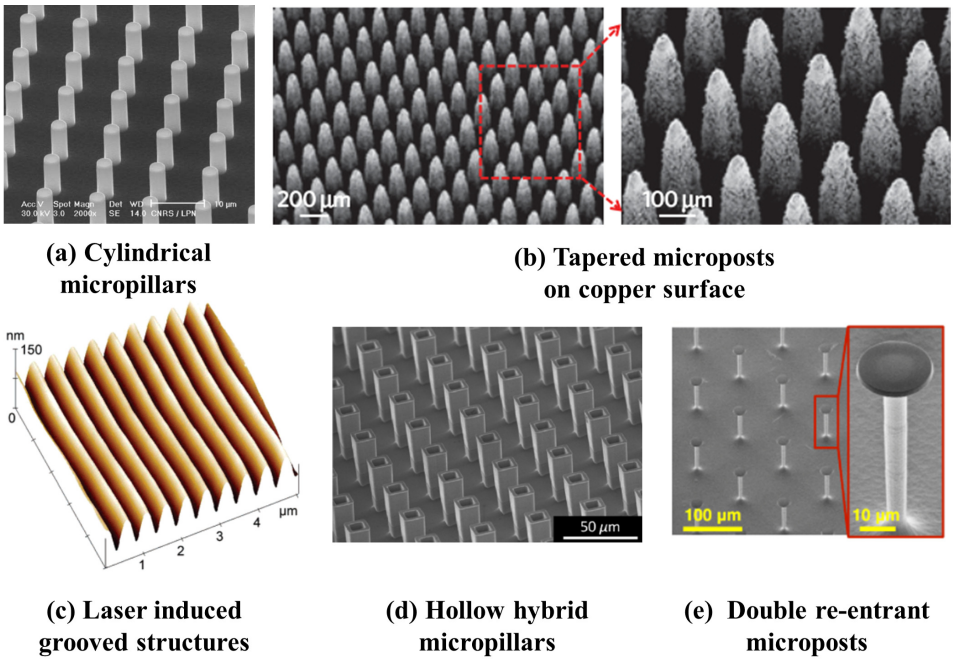

Figure 1.12: Various microtextured surfaces studied for superhydrophobicity. (a) Scanning electron microscope (SEM) image of cylindrical micropillars made of silicon (both pillars and base surface), prepared using photolithography and deep reactive ion etching (DRIE) technique. Adapted from Ref. [14]. (b) SEM image of tapered microposts on copper surface, prepared using wire cutting machine followed by chemical etching and a thin polymer (trichlorosilane) coating. Adapted from Ref. [15]. (c) 3D AFM image of laser-induced grooved structures on azobenzene-containing polymer film. Adapted from Ref. [16]. (d) SEM image of hollow hybrid structures, fabricated using photolithography and DRIE technique. Adapted from Ref. [17]. (e) Double re-entrant SiO_2 microposts, fabricated using DRIE technique. Adapted from Ref. [18].

wetting angle (θ_W) is given by the following relation,

$$cos\theta_W = r\,cos\theta \tag{1.6}$$

where, r is the roughness (created because of the textures) of the surface. If the droplet liquid does not penetrate the textures and sits on the top surface of the microtextures, then it is said to be at Cassie state. The Cassie wetting angle (θ_C) is given by the following relation,

$$cos\theta_C = -1 + f\,cos\theta \tag{1.7}$$

where, f is the solid fraction of the top of the microtextured surface.

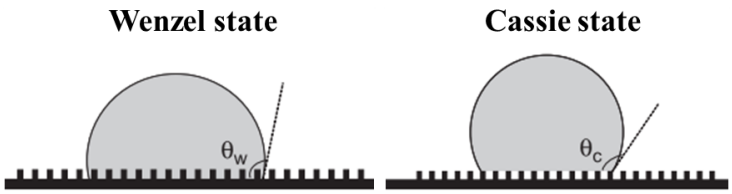

Figure 1.13: Wenzel state in which the droplet penetrates in between the textures and Cassie state in which the droplet sits on the top of the textures. Image is taken from [19].

1.3 Scope and objectives of the present work

The interfacial phenomenon is influenced by many factors such as temperature and humidity of the air, thermal and physical properties of the substrate, and droplet shape, size, and surface tension. Understanding the fluid dynamics, mass transfer, and heat transfer at the micro scale, taking into account the wide range of properties of the liquid, solid, and gaseous environment is the ultimate objective. From the available literature (described in the following chapter), evaporation of a sessile droplet suspended with colloidal particles, on non-heated substrates has been studied extensively. However, most of the studies have reported with either single particle size or concentration. Although the axisymmetric Marangoni recirculation inside the droplet due to the uniformly heated substrate is well-developed, the non-axisymmetric Marangoni recirculation due to non-uniform temperature on the substrate is not yet explored. The coupled effect of particle size and concentration on the morphology of the ring formed on a non-heated substrate and the pinning and depinning of the contact line with respect to the particle size on either uniformly or nonuniformly heated substrate is yet to be explored. In the context of impact dynamics, the droplet impacting on a hydrophilic surface has been studied extensively both experimentally and numerically. Whereas, the droplet impact study on the microtextured surfaces is still in development. Therefore, in the present Ph.D. research work, the evaporation of a sessile water droplet containing colloidal particles on a solid surface, and droplet impact dynamics on microtextured surfaces are proposed to be studied.

1.4 Organization of thesis

This thesis presents five chapters, which are presented as follows,

Chapter 1 - Introduction: It introduces the droplet evaporation and impact dynamics problem. The scope and motivation for the present study are presented.

Chapter 2 - Colloidal Deposit of an Evaporating Aqueous Droplet on a Non-heated Substrate: This chapter presents the colloidal solution preparation and experimental methods to measure the deposits. The different deposition patterns obtained from the evaporation

of a droplet suspended with colloidal particles, the ring morphology, and profile as a function of colloidal particles size and concentration is reported and proposed a regime map classifying regimes of the discontinuous monolayer ring, continuous monolayer ring, and multiple layers ring on particle concentration - particle size plane

Chapter 3 - Colloidal Deposit of an Evaporating Aqueous Droplet on a Non-uniformly Heated Substrate: This chapter presents the experimental methods to obtain non-uniform temperature on the substrate using Peltier coolers and visualization technique from the top with an infrared camera and side visualization using the high-speed camera as evaporation proceeds with time. The different deposition patterns obtained as a function of temperature gradient on the substrate and particles size are discussed.

Chapter 4 - Impact Dynamics of a Pure Aqueous Droplet on Microgrooved Surfaces: This chapter introduces droplet impact on microtextured surfaces, reviews the literature on experimental droplet impact study on micropillared and microgrooved surfaces, studies the effect of the pitch of the grooves and Weber number on the impact dynamics and proposed a regime map for different outcomes of the droplet impact study such no bouncing, complete bouncing, bouncing with droplet breakup.

Chapter 5: Conclusions and Future Scope of Work: This chapter explains the conclusions drawn from the present work for the three problems presented from chapter 2-4, and finally, present the scope of future work.

Part I

Self-Assembly of Colloidal Particles

Chapter 2

Colloidal Deposit of an Evaporating Aqueous Droplet on a Non-heated Substrate[1]

The profile and morphology of the ring-like deposits obtained after evaporation of a sessile water droplet containing polystyrene colloidal particles on a hydrophilic glass substrate is investigated. The coupled effect of particle size and concentration are studied. The evaporation of a sessile water droplet containing graphene nanoplatelets on a glass substrate was also investigated independently, to study the effect of the concentration of dispersed graphene nanoplatelets in water. The final deposits were qualitatively visualized under an optical microscope and profile of the ring was measured by an optical profilometer. In the case of polystyrene particles as colloidal suspensions, the profile of the ring resembles a partial torus-like shape for all cases of particles size and concentration. The cracks on the surface of the ring were found to occur only at smaller particle size and larger concentration.A regime map is plotted to classify discontinuous monolayer, continuous monolayer and multiple layers formed in the ring on particles concentration-particle size plane. There exists a critical concentration (particle size) for a given particle size (concentration) at which the monolayer forms. For the larger particle sizes, the immersion capillary forces between the particles dominate aiding the formation of a monolayer of particles. The relative mass of the particles accumulated in the ring is lesser in cases of the monolayer. Both the width and height of the ring is measured and show that they scale with particle concentration by a power law for the rings of multiple layers of the particles. This scaling corroborates with an existing continuum based theoretical model. The effect of the interaction of growing deposit with shrinking free surface on ring dimensions and profile is briefly discussed. In the case of graphene

[1] **LK Malla**, R Bhardwaj, A Neild, "Analysis of Profile and Morphology of Colloidal Deposits obtained from Evaporating Sessile Droplets" *Colloids and Surfaces A : Physicochemical and Engineering Aspects*, 567 (2019) 150-160. https://www.sciencedirect.com/science/article/pii/S0927775718316157

nanoplatelets as colloidal suspensions, the same coffee-ring like final deposits were obtained, however, the 2D flakes type graphene nanoplatelets remained as a coating on the substrate that is minimal ring height in comparison to the ring width.

Graphical Abstract: The evaporation dynamics of a microliter water droplet containing polystyrene colloidal particles on a non-heated glass substrate, recorded by high-speed visualization and optical microscopy to study effect of the particles diameter and concentration on the profile and morphology of the ring formed.

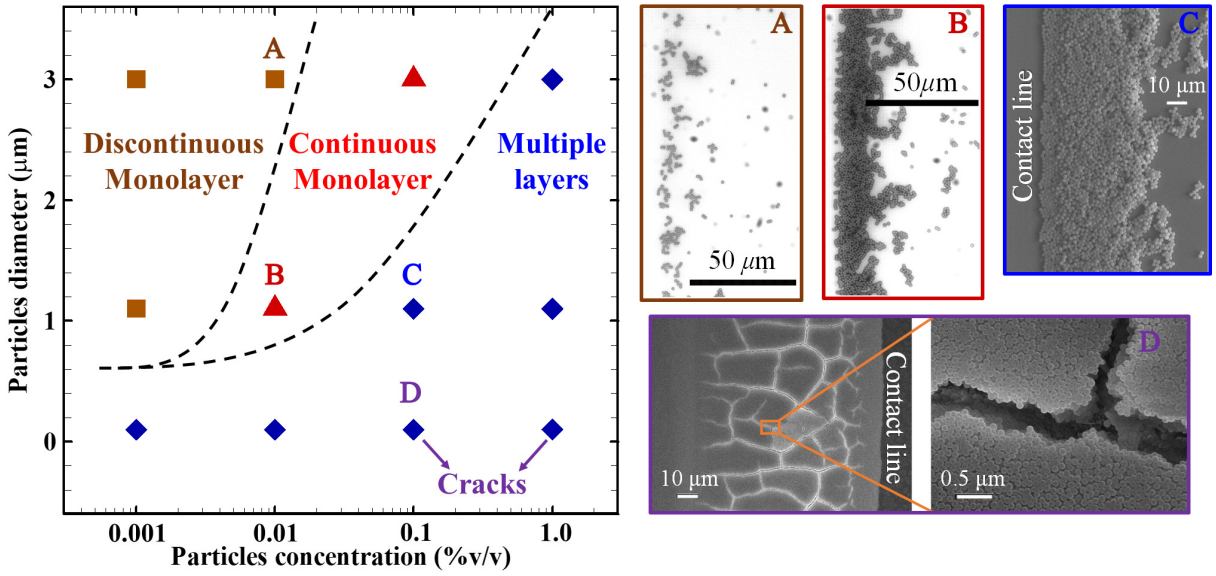

2.1 Introduction

Recent reviews by Routh [62] and Parsa et al. [45] identified a multitude of parameters, which could play a role in determining the pattern of the final deposit: Marangoni convection, pH of the suspension, particle size, particles shape, particle concentration, substrate temperature, substrate wettability, particles hydrophobicity, relative humidity, electrowetting etc. In particular, Marangoni convection has been shown to reverse the coffee-ring effect [9, 20, 32, 46] and an inner deposit with a much smaller radius than the initial wetted radius is the final outcome instead of the ring. By lowering the pH [8] or by using ellipsoidal particles [63], or by applying electrowetting [64, 65] the particles deposit uniformly across the wetted area. Indeed, the deposit pattern could alter substantially depending upon the system used and some examples of the patterns include, a uniform deposition [66], an inner deposit [67], a stick-slip pattern resulting in multiple rings [68], fingering-like pattern [69], patterns displaying cracks [70], a crystalline pattern [71] , a ring with an inner deposit [20] and patterns combining more than one of these features. In the following section, some studies on the colloidal deposits influenced remarkably by particles size, concentration,

shape, and wettability are extensively reviewed.

2.2 Literature review

2.2.1 Effect of particles size

There has been numerous previous studies, which reported the effect of particle size on the deposit patterns. For example, the evaporation of an aqueous polystyrene particles suspension on mica substrate produce ring with smaller inner rings for 0.1 μm particles while three zones, namely, ring, arches and radial lines with half arches form for 1 μm particles [42]. Chon et al. [72] studied evaporation of droplet containing different diameters of particles, namely, Au (2 nm), Al_2O_3 (11 nm and 47 nm), and CuO (30 nm), with 0.5% concentration. They found that the droplet containing smaller particles form a wider ring with central deposition while larger particles droplet form a distinct narrower ring. Perelaer et al. [73] investigated the deposition behavior of silica particles of different sizes [0.33 - 5] μm and reported that the diameter of the dried deposit is slightly smaller than the initial wetted diameter and difference between the two diameters increases with an increase in particle diameter due to wedge shape of the interface at contact line.

Bhardwaj et al. [32] studied evaporation of colloidal droplet containing 0.1 and 1 μm polystyrene particles at 1.0 % particles concentration. They reported partial torus-like ring profiles for smaller particles size, whereas monolayers were formed for larger particle size. Marin et al. [74] studied the ordered to disordered transition of the particles packing at the contact line for different particles sizes of 0.5 - 2 μm. This transition occurs during the last stages of evaporation, when the shrinking interface leads to a sudden increase in the outward radial velocity, the resulting rush-behavior of the particles leads to disorder arrangement of the particles at the inner edge of the ring. Weon and Je [75] explored self-pinning characteristics of a decalin droplet suspended with PMMA particles and found that the colloidal droplet pins at the initial contact line irrespective of particles size, with the capillary force experienced by the particles at the contact line retarding the spreading of the droplet due to pinning. Subsequently [69], they showed that small PMMA colloids of $d = 0.1$ μm tend to form coffee-ring at contact line, whereas, large colloids of $d = 1.0$ μm tends to form a central bump for the decalin droplet and with an increase in particles concentration the ring and central bump increases.

Yang et al. [76] recorded different deposits - multi-ring, radial spokes, spider web, foam, and islands - using droplets containing sulfate-modified polystyrene particles of different size ([20-200] nm) and concentrations over a very small range ([0.1-0.5] % v/v). They attributed these deposits to competition between the receding contact line velocity and the particle deposition rate at the contact line. Ryu et al. [77] observed rings for 0.1, and 1.0 μm

particles and bumps for 5 and 10 μm particles. The absence of flocculation of the larger particles in the droplet hinders ring formation. Patil et al. [7] studied the deposition patterns of polystyrene particles of different sizes (0.1, 0.46, 1.1, and 3 μm) on a silicon wafer. They reported that an inner deposit and a thin ring with inner deposit form for smaller and larger particles, respectively. The formation of the deposits was explained by early depinning and self-pinning of the contact line in the two cases, respectively. Hence, a wide range of behaviour has been identified as a result of changing particle size, but these studies consider only a single concentration or a very limited range of concentrations.

Graphene has become a prominent subject in the field of colloidal sciences due to its importance in producing electronic circuits [28], organic thin film transistors [29], etc. in the printed electronics field. Kim et al. [28] reported the effect of the size of the graphene oxide nanosheets on forming a uniform film when drop cast. A droplet containing graphene oxide nanosheets forms a uniform deposition at a critical temperature of the substrate, and that critical temperature is smaller for larger size graphene nanosheets. Nayak and Prabhu [78] studied the wettability characteristic of the graphene-based nanofluids and reported the increase in heat transfer capabilities of such fluids with an increase in solute concentrations.

2.2.2 Effect of particles concentration

In the context of the effect of particles concentration on the ring-like deposits, Sefiane [79] varied Al_2O_3 particle concentration (0.1, 0.5, 1.0, and 2.0 %) and found ring thickness increases with concentration and radial spoke-like patterns became evident at the higher concentrations studied. Orejon et al. [80] reported that suspended TiO_2 nanoparticles in a water droplet induce stick-slip motion of the contact line and that with an increase in the TiO_2 concentration, the depinning time of the contact line increases on both hydrophilic and hydrophobic surface. Brutin [81] observed a ring without any inner deposits for a critical concentration of 1.15 vol% of 24 nm size polystyrene particles, and above that a flower-like inner deposit was observed. Nguyen et al. [82] observed the formation of inner deposit with organic pigment nanoparticles during the evaporation of sessile water droplets on smooth hydrophobic surfaces. The radius of this inner deposit is smaller than the initial wetted radius and as it increases with increase in the particle concentration.

Ryu et al. [77] reported that the increase in the concentration of polymer (PEO) to the water colloidal solution of PMMA, suppresses the ring in case of smaller colloids, however, enhances in case of larger colloids. The aggregation of the small colloids with the addition of polymer prevents the outward radial flow of the particles, however, for large colloids, ring-induced hydrodynamics is more predominant than colloid-polymer interactions [77]. Lee et al. [83] observed uniform deposits of Al_2O_3 particles (0.1 μm) on glass substrates at

concentrations of greater than equal to 1%. They reported that ring forms on a less wettable surface and the ring widths are larger for smaller particles. In a recent study, Patil et al. [20] measured ring profiles for 460 nm particles at 0.1% and 1% concentration and reported an increase in ring width and height with the concentration. Sondej et al. [84] used white light interferometry to measure the ring profiles obtained after evaporation of a sessile water droplet containing sodium benzoate particles and reported the increase in ring height and reduction of drying rate with increase in the particles concentration. Again, whilst there is a large number of studies on the effect of concentration, they focus on a single particle size. Zhong and Duan [85] reported the effect of concentration of graphene nanoparticles as a solute with water and water plus ethanol as solvents, on evaporation rate and pinning effect. The addition of ethanol to water results in a relatively lower surface tension of the water-ethanol binary fluids, and a smaller initial contact angle and a longer wetted diameter for the nanofluid droplets [85]. Due to non-uniform distribution of ethanol in the mixture, Marangoni flow occurs inside the droplet, the flow becomes chaotic, and vortices are observed over the liquid-air interface with a concentration of graphene nanoparticles and ethanol at 1.5 g/L and [0-50] % v/v, respectively [85].

2.2.3 Effect of particles shape

A uniform deposition of the particles is obtained after evaporation of water droplet suspended with ellipsoidal shape particles on a glass substrate, whereas ring is formed with spherical shape particles [63]. Anisotropic particles such as of ellipsoidal shape move towards the liquid-air interface during evaporation and interlock among themselves forming an arrested structure at the interface, which reduces the mobility of the particles and leading to lower outward radial flow [63].

2.2.4 Effect of particles wettability

The particle hydrophobicity can also influence the morphology, as reported by Shao et al. [86]. They showed that the hydrophobic particles result in a spoke-like deposit as compared to a typical ring-like deposit due to stronger capillary forces between them [86].

2.2.5 Cracks on the ring

Regarding the morphology of the rings formed, cracks on the surface of the ring have been previously reported, for example, Pauchard et al. [87] observed a radial crack pattern at regular intervals on the ring of the dried deposit of aqueous silica solution (particles diameter of around 30 nm) with the addition of small quantity of salt. Brutin et al. [88] observed distinct crack patterns on the periphery of the ring of a dried blood drop on glass

($\theta_{eq} = 21°$), which is more wettable, whereas, on Gold ($\theta_{eq} = 92°$) and Aluminium ($\theta_{eq} = 96°$) surfaces, no cracks are observed. Carle and Brutin [89] investigated the different crack patterns formed on the dried patterns of different nanofluid droplets with different surface functional groups on substrates of different surface energy. They reported that the crack spacing/deposit height ratio is a linear function of the substrate surface energy, irrespective of the surface functional groups of the nanofluid. Zhang et al. [90] reported radial crack patterns on the ring of PTFE deposits with an increase in crack length and crack spacing with an increase in PTFE concentration. They also reported that the surface wrinkling of the gel phase of the drying droplet to be one of the reasons for the initiation of cracks.

Ghosh et al. [91] reported the effect of the substrate wettability on the dynamics of the cracks formed on the dried rings of an aqueous droplet containing polystyrene nanoparticles ($d = 53$ nm). They reported the crack length from its tip at the outer ring periphery, and the crack rupture thickness decreases and increases, respectively, with the increasing hydrophobicity of the substrate. Kim et al. [92] studied the crack formation mechanism on drying of a colloidal droplet of PMMA particles and observed that the crack initiation mechanism is favorable in small colloids (0.1 μm diameter) than that to the large colloids (1 μm diameter) due to air invasion inside the ring in the former. Lama et al. [70] studied crack formation in the ring using silica nanoparticles and polystyrene particles (0.1 μm diameter) of different concentration of [0.1-2.0] % wt and observed larger crack density and ordered cracks on the ring at a larger substrate temperature due to lesser ring height. Dugyala et al. [93] reported on the effect of particles shape on the cracks formed in the ring and observed radial and concentric crack patterns for spherical and ellipsoidal particles, respectively. A recent review by Giorgiutti-Dauphiné and Pauchard [94] identified several factors affecting crack patterns on the dried droplet, such as initial contact angle of the droplet, relative humidity, mechanical properties of the solute, shape of the solute, external force, etc. They also reported that the capillary pressure in a random close packing of monodisperse particles scale as 5.3γ/d, that is, dried patterns of a droplet containing smaller size particles are more prone to cracking. Here, too though, there has been little work on examining the occurrence of cracks in a single system over a wide range of concentrations and particle sizes, or quantitative studies of the rings formed.

2.3 Objectives

While the influence of either particle size or concentration on the deposit formation has been studied, there has been no paper reporting on the combined effect of these two key parameters, to the best of our knowledge, with exception of the work of Weon and Je [69]. However, in this paper, authors investigated the deposition patterns for a system (decalin/glass) that exhibits Marangoni effect while the focus of the present work is to consider a system

(water/glass) without Marangoni effect. Note that the evaporating water droplets in ambient temperature do not exhibit Marangoni effect [46]. The second issue in this arena is that the quantitative measurements of ring profile or dimensions as a function of particle size and concentration have not been reported, to the best of our knowledge.

The present work investigates the cross-sectional profile of the ring as a function of particle size and concentration. In the context of the ring morphology, it is not clear under which conditions the deposit would comprise of mono or multiple layers of particles and how cracks on the surface of the ring-like deposit would be influenced by particles size and concentration. It has been shown in the literature that the particle size influences the deposit pattern and shape significantly. For instance, larger colloids (20 μm polystyrene microspheres) deposit inside the ring as compared to smaller colloids (2 μm polystyrene microspheres) that deposit in the ring, explained by a larger capillary force on the larger colloids [95]. In addition, it is well-known that larger colloids exhibit strong capillary forces among them during drying [96]. However, the monolayer ring formed for large colloids below a critical particle concentration and the dynamics in its formation have not been explored in the literature. Therefore, the overall objective in this chapter's work is to quantitatively investigate the coupled effect of the particles size and concentration on the profile, dimensions, and morphology of the ring.

Also previous studies on the evaporation of graphene-based nanofluids focussed only on wettability characteristic study, and formation of a uniform film of deposit digressing towards its electrical application part. Graphene nanoplatelets are 2D flakes type structure and the evaporation dynamics of water-based graphene nanoplatelet solution has not been studied extensively in literature to the best of the author's knowledge. The effect of the concentration of the graphene nanoplatelets in the solvent and substrate heating on the deposit patterns is investigated.

2.4 Experimental methods

Aqueous colloidal suspensions of 10 % v/v of uniformly monodispersed polystyrene latex beads of diameter $d = 0.1$ μm (LB1), 1.1 μm (LB11), and 3.0 μm (LB30) were obtained from Sigma Aldrich Inc. The standard deviation of the particles diameter in the suspension is on the order of 5-15% of the mean diameter and the particles density is around 1005 kg/m^3, as per the manufacturer's data sheet. Solutions over a wide range of concentrations, $c = 0.001$, 0.01, 0.1, and 1.0 % v/v, were prepared by diluting with deionized water. The graphene nanoplatelet dispersed in water concentration of 1 mg/ml, was also obtained from Sigma-Aldrich Corporation, USA (799092, Graphene 0.1 wt%, and water 99.9 wt%). The original solution concentration regarding volume percentage is 0.1 %v/v. This solution was further diluted with deionized water to prepare concentrations of c = [0.01 - 0.1] %v/v. After di-

	0.001 % v/v	0.01 % v/v	0.1 % v/v	1.0 % v/v
0.1 μm	34°	34°	33°	33°
1.1 μm	36°	36°	35°	34°
3.0 μm	42°	41°	39°	42°

Table 2.1: Measured initial static contact angles (in degrees) of the droplets containing polystyrene particles for different cases of particles concentration (c) and particle size (d). The uncertainty in these measurements is around ±1°.

	0.001 % v/v	0.01 % v/v	0.1 % v/v	1.0 % v/v
0.1 μm	1.4	1.4	1.5	1.4
1.1 μm	1.3	1.3	1.4	1.3
3.0 μm	1.4	1.3	1.3	1.3

Table 2.2: Measured initial wetted radius (in mm) of the droplets containing polystyrene particles for different cases of particles concentration (c) and particle size (d). The uncertainty in these measurements is around ± 0.1 mm, respectively.

lution, sonication of the solutions was performed for about 30 minutes to ensure uniform suspension of the particles in the solutions. The droplets of the colloidal suspensions were generated using a micropipette (Prime, Biosystem Diagnostics Inc.) of the volume of 1.1 ± 0.2 μL. The droplets were gently deposited on the substrate.

Glass slide (Sigma Aldrich, S8902) with dimensions of 75 x 25 x 1 mm^3 served as the substrate in all experiments. The glass slide was washed with isopropanol and was allowed to completely dry in the ambient conditions for few minutes before the droplet was deposited on it. A fresh slide was used to repeat or to perform a new experiment. The droplet wetted radius (R) and height (H) for the experiments of polystyrene particles as colloidal suspensions were measured using images obtained from a side view. Since the wetted diameter of the deposited droplet was below the capillary length of water (≈ 2.7 mm), the droplet displays a spherical cap and the initial static contact angle is given by, $\theta = 2tan^{-1}(H/R)$ [13]. The measured values of the contact angle and wetted radius based on three experimental runs are listed in Table 2.1 and Table 2.2, respectively. The uncertainties in these measurements are around ±1° and ± 0.1 mm, respectively. While the measured initial static contact angle does not show significant variation with particle concentrations there is a slight increase in the contact angle with an increase in particle size.

The dried patterns of the colloidal particles were visualized from the top by an optical microscope (Olympus Corp. Inc., BX53F, with a magnification of 10X to 40X). The final dried patterns obtained after evaporation of the aqueous graphene nanoplatelets were visualized from the top by a high-speed camera (Motion Pro, Y-3 classic) mounted on a tripod. A LED light acted as a back-light source for the camera and was placed inside the hollow transparent base. During the evaporation, particle motion was visualized by a high-speed camera (IDT Inc, Motion- Pro Y-3 classic) mounted on the optical microscope. Field

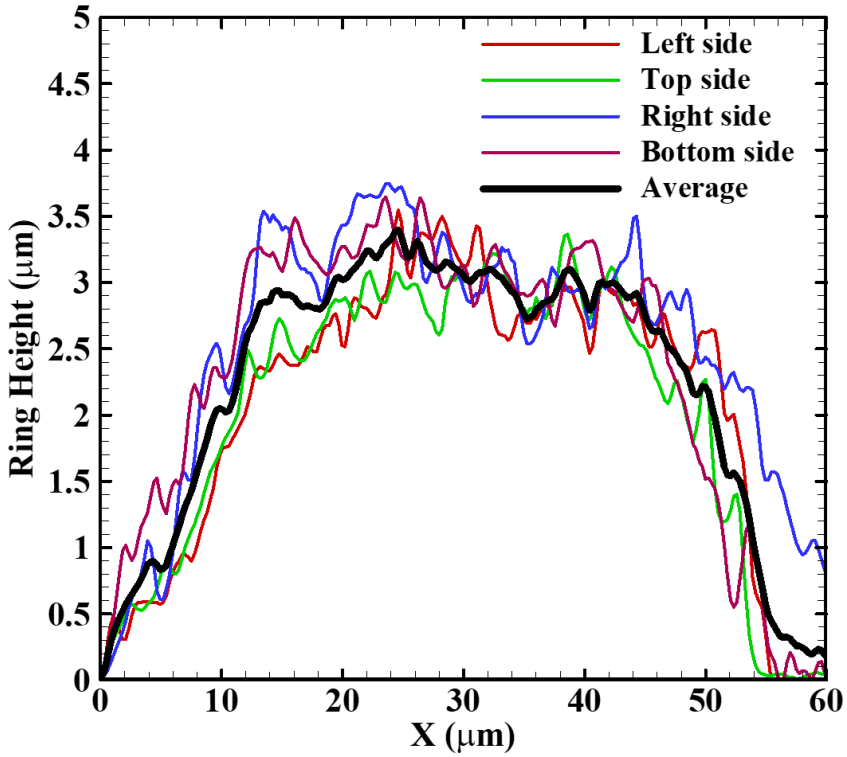

Figure 2.1: Measured ring profiles obtained after evaporation of 1.1 μL droplet containing 1.1 μm polystyrene particles with 0.1 %v/v concentration on a glass surface with an averaged profile (thicker black line).

emission gun scanning electron microscope (JSM-7600F, Jeol Inc) was employed to record a high-resolution view of the ring morphology. The ring profiles were quantitatively measured by a 3D optical profilometer (Zeta-20, Zeta Instruments Inc., optical resolution ~ 0.1 μm). The ring profile was measured at four locations (the left, top, right, and bottom side) around the periphery of the ring as shown in Figure 1.6 (a), which is the case for $d = 1.1$ μm, and $c = 0.1$ %v/v. The average profile was obtained using the profiles at these four locations, as shown by a thick black line in Figure 2.1. All experiments were performed three times to ensure repeatability. The ambient temperature and relative humidity were 27 $\pm$ 2°C and 35 $\pm$ 5%, respectively.

2.5 Results and discussions

2.5.1 Polystyrene particles

The results for the evaporation of 1.1 $\pm$ 0.2 μL water droplets containing polystyrene particles on hydrophilic glass substrate for three cases of particle diameter ($d = 0.1$, 1.1, 3.0 μm) and four cases of particle concentrations ($c = 0.001$, 0.01, 0.1 and 1.0 %v/v) is presented.

2.5.1.1 Deposit patterns and morphology of the ring

Figure 2.2 shows the top view of dried deposits obtained after the evaporation of the droplet for different cases of particle size and concentration. Each row and column in Figure 2.2 represent a constant particle size and constant particle concentration, respectively. The deposit is predominantly a ring in all cases and its formation is explained as follows. The contact line remains pinned during the evaporation for the aqueous droplet considered here, as reported in our previous work [20]. The ring forms due to advection of the particles by the evaporation-driven outward flow [37]. As reported by Hu and Larson [46], the Marangoni flow is absent during evaporation of a water droplet at ambient temperature, consistent with our observations here. Note that the substrate thickness is large enough not to induce a thermal gradient on the liquid-gas interface due to the latent heat of evaporation [97]. At larger particles concentration and larger particle diameter ($c = 1.0$ % for $d = 1.1$ μm and 3 μm), alongside the formation of the ring, particles are also deposited in the inner region of the droplet.

The settling velocity of the particles can be estimated using Stokes's law as follows,

$$U_s = d^2(\rho_p - \rho)g/18\mu, \tag{2.1}$$

where d, ρ_p, ρ, g and μ are particles diameter, particle density, the density of water, gravitational acceleration, and viscosity of water, respectively. The evaporation-induced advection velocity is estimated as follows [8],

$$U_e = j_{max}/\rho, \tag{2.2}$$

where j_{max} is the maximum evaporation rate at the pinned contact line. The estimated values of U_e/U_s for 0.1, 1.1, and 3.0 μm are 25310, 215, and 24, respectively, implying that evaporation-induced advection overwhelms gravitational sedimentation of the particles. Therefore, the main mechanism of the particles deposition in the ring in the present work is the same as reported in classical "coffee-ring" deposition [37]. The ring width increases with the increase in the concentration for a particular size as observed qualitatively in 2.2.

Figure 2.3 shows the zoomed-in view of the ring, exhibiting morphology, for all cases. The contact line is on the left of each frame. Note that few out-of-focus marks seen in some images (specifically seen in the image of the case of $d = 1$ μm) are experimental artefacts. With the increase of particle concentration more particles are deposited in the ring, resulting in it being both thicker and more densely packed, this is observed qualitatively in Figure 2.3. In Figure 2.3 (second row) for $d = 1.1$ μm, a discontinuous and continuous monolayer of the particles are observed at $c = 0.001$, and 0.01 %, respectively (the ring height is confirmed through quantification in section 3.5.2). Similarly, at $d = 3.0$ μm and for $c = 0.001$ and 0.01 %, discontinuous monolayer ring forms while for $c = 0.1$ %, continuous mono-

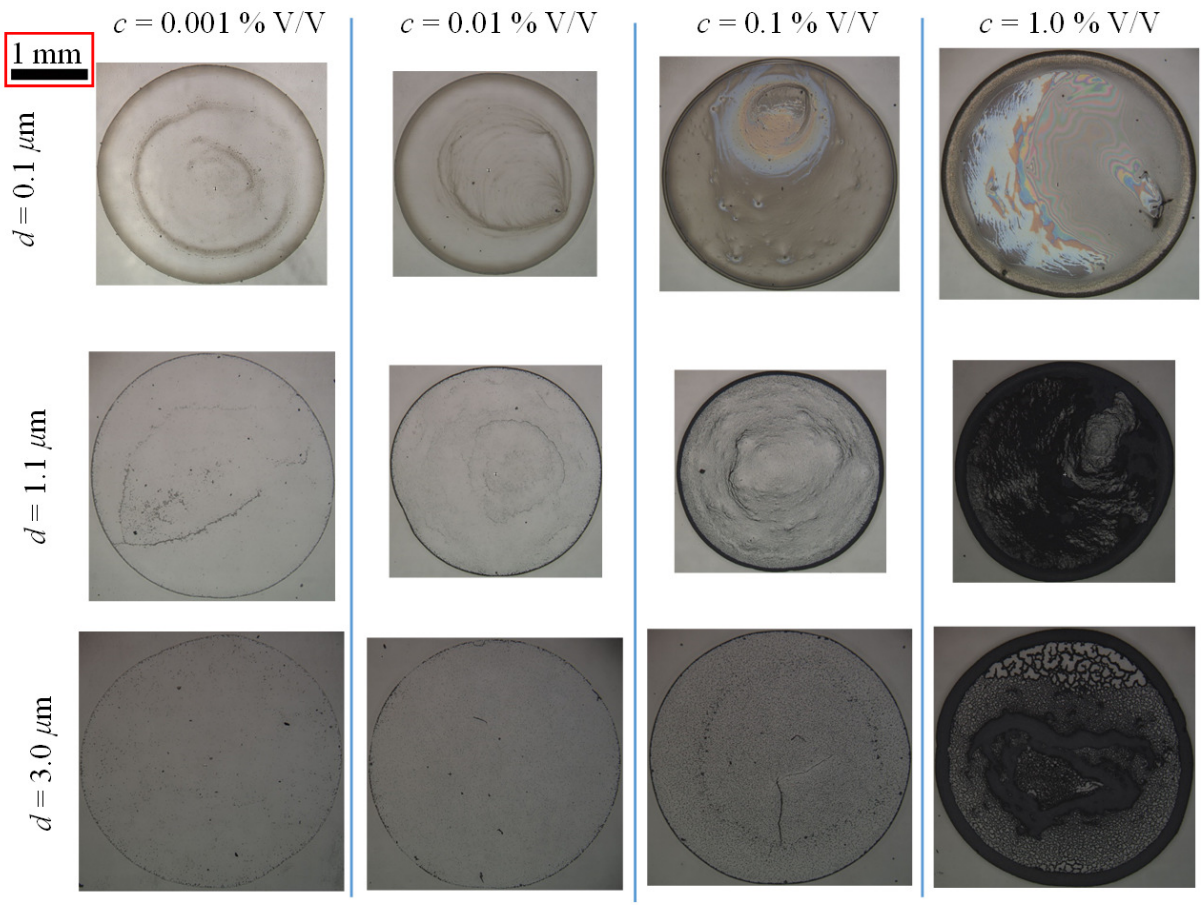

Figure 2.2: Ring-like deposit patterns obtained after the evaporation of 1.1 μL water droplets containing polystyrene particles on a hydrophilic glass substrate. Particle size is kept constant in three rows ($d = 0.1$, 1.1, 3.0 μm) and particle concentration is kept constant in four columns ($c = 0.001$, 0.01, 0.1 and 1.0 %). The scale is shown in the top left.

$c\%v/v$	Crack spacing (μm)	Cracks per unit length (μm^{-1})
0.1 μm	13.33 ± 2.2	0.0825
1.1 μm	17.63 ± 4.3	0.0588

Table 2.3: The crack spacing and the number of cracks per unit length for spherical particles of the size, $d = 0.1$ μm and concentrations, $c = 0.1$, and 1.0 % v/v.

layer rings forms. As c increases, the particles stack up in the ring at $c = 0.1$, and 1.0 % for $d = 1.1$ μm and at $c = 1.0$ % for $d = 3.0$ μm and rings with multiple layers of the particles form.

The formation of the monolayer ring can be attributed to the increase in the inter-particle capillary forces at larger particle size, as these forces scale with d^2 [96]. The deposits of $d = 1.1$ μm (Figure 2.3, $c = 0.01$ to 1%) and $d = 3$ μm (Figure 2.3, $c = 0.1$ to 1% and Figure 2.4(b)) show ordered crystal-like morphology near to the contact line while disordered random aggregates form closer to inner boundary of the ring and in the inner region (Figure 2.4(b)). As explained by Marin et al. [74], these different morphologies exist due to a rather slow deposition of the particles in the initial stage of the evaporation, due to which particles get enough time to order themselves by Brownian motion into a crystal-like structure.

For the more complex stacked structures which can be deposited, under certain conditions, cracking occurs during ring formation for $d = 0.1$ μm at $c = 0.1$ % and $c = 1.0$ % (last two frames of the first row of Figure 2.3). At $c = 0.1$ %, disordered and dendritic-like cracks are obtained, whilst for $c = 1.0$ % the cracks are ordered along the radial direction and aligned along the direction of the drying front. An SEM image of the cracks at $d = 0.1$ μm, $c = 0.1$ % (Figure 2.4(a)) shows a dense packing of the particles at the two interfaces of the crack. As pointed to in Refs. [6, 70, 93, 98], a growing ring exhibits a gel-like behavior with a dense packing of the particles.

As the liquid evaporates in the final drying stage, the ring tries to shrink, and the pinned contact line obstructs such shrinkage. This results in stresses in the deposit and consequently, it induces cracks in the ring. The cracks appear only in the last stages of the evaporation as confirmed by the time-varying images in Figure 2.5 (a) showing particles deposition in the ring for $d = 0.1$ μm, $c = 0.1$ %. The cracks spacing and the number of cracks per unit length for $d = 0.1$ μm, $c = 0.1$, and 1.0 % are calculated from the zoomed-in images of Figure 2.3 and are reported in Table 2.3. With an increase in the particles concentration, the spacing between two consecutive cracks increases and the number of cracks per unit length decreases, consistent with previously reported data by Dugyala et al. [93] for ellipsoidal particles.

The cracks are not observed for larger colloidal particles because air entrainment occurs in the gaps between the particles as confirmed by SEM image for $d = 1.1$ μm in Figure

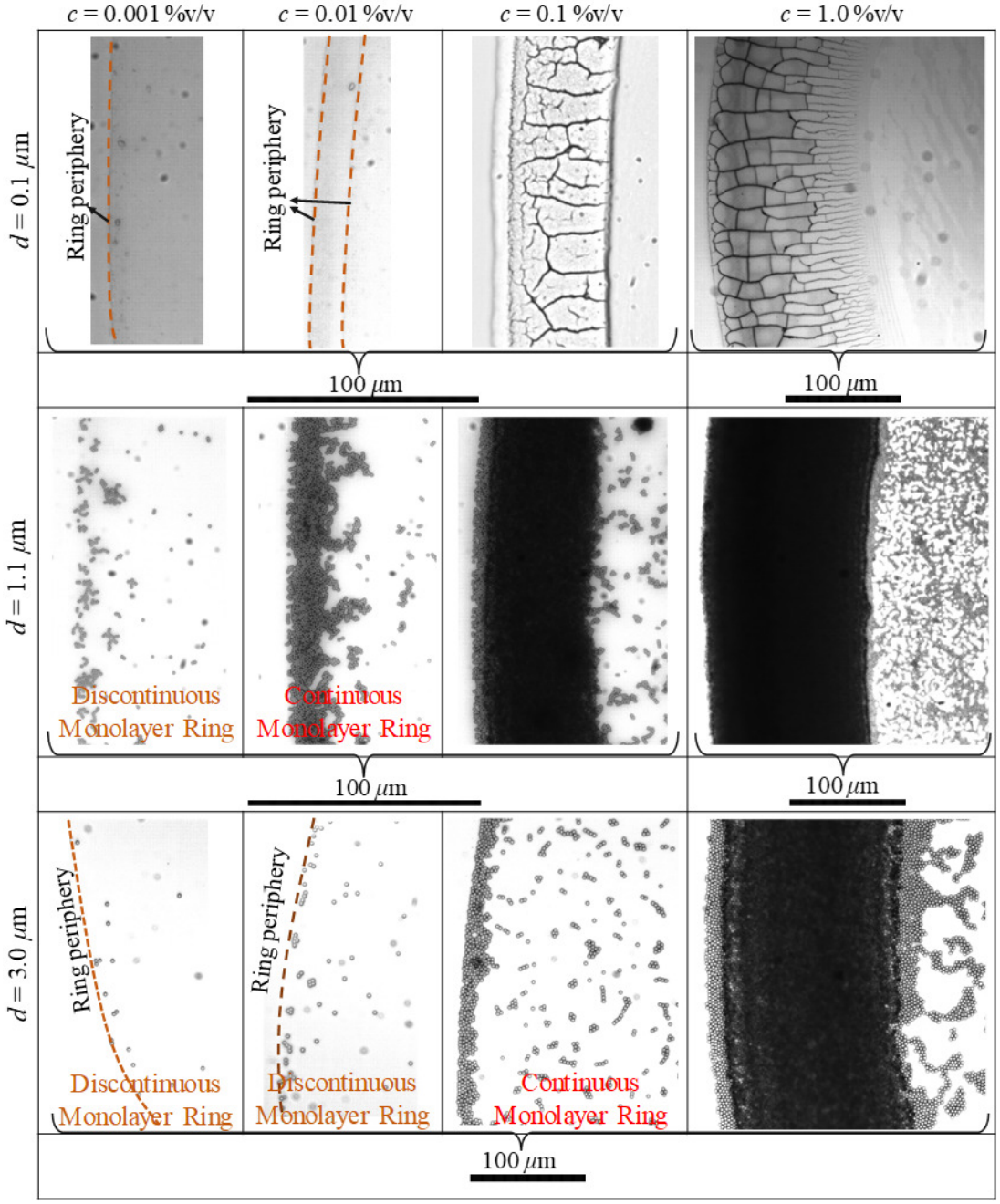

Figure 2.3: Morphologies of the rings for the cases plotted in Figure 2.2 are shown by the zoomed-in view of the ring for the respective case. Scale bars are given below the respective images.

2.4(b). This finding is consistent with data reported by Kim et al. [92]. Since larger colloidal particles have larger inter-particles air gaps, stress is not induced between them. In the inner region of the deposit, the disordered deposit of particles at larger particle size is recorded, as shown on the right-hand side of the frames in Figure 2.3 (second row and third row) and in the SEM image in Figure 2.4(b). This occurs due to the drying and breakup of the thin liquid film containing particles in the last stages of the evaporation. Singh and Tirumkudulu [99] reported the minimum film deposit height required for the crack propagation, which is,

$$h_{min} = 0.41\sqrt{(GMpR^3/2\gamma)}, \tag{2.3}$$

where G, M, p, R, γ are the particles shear modulus, coordination number, particles packing fraction, spherical particle radius, and air/liquid surface tension, respectively. The ring heights obtained for $c = 0.001$ and 0.01 % are below the critical film cracking thickness [99] for polystyrene beads of $d = 0.1$ μm ($h_{min} \approx 1$ μm) and thus, no cracks are observed for these cases in Figure 2.3.

The dynamics of the particle deposition process is compared for different cases of particle size and plot time-sequence images recorded by microscopy showing time-varying particles deposition in the ring for particle sizes of $d = 0.1$, 1.1 and 3.0 μm in Figure 2.5(a), (b) and (c), respectively, at $c = 0.1$ %. The focal plane is on the substrate surface in all cases and out-of-focus particles are visible in case of $d = 1.1$ and 3.0 μm in Figure 2.5(b) and (c), respectively. The contact line is pinned during the evaporation and particles advect towards the ring in all cases. The ring front shows a significant growth for 0.1 μm and 1.1 μm particles in Figure 2.5(a) and (b), respectively and the particles stack up in multiple layers in these two cases (also confirmed in Figure 2.4(b)).

Cracks are visible on the ring surface at $t_0 + 150$ s for 0.1 μm particles in Figure 2.5(a) and Figure 2.4(a). In Figure 2.5(c), 3.0 μm particles form a monolayer of particles in the ring instead of stacking up in the multiple layers. During initial stages of the evaporation ($t < t_0$), the particles are blocked in a wedge-like region of the contact line and deposits few micrometers away from the contact line (Figure 2.5(c)), consistent with findings reported by Patil et al. [7] for 3.0 μm particles. At later times ($t > t_0 + 40$ s), other incoming particles to the contact line adhere to the ones, which are already present near the contact line due to large immersion capillary forces [96], that scale with the square of particle diameter. In the last stages of the evaporation, some particles also deposit in the inner region as the contact line recedes and the remaining liquid film dries out.

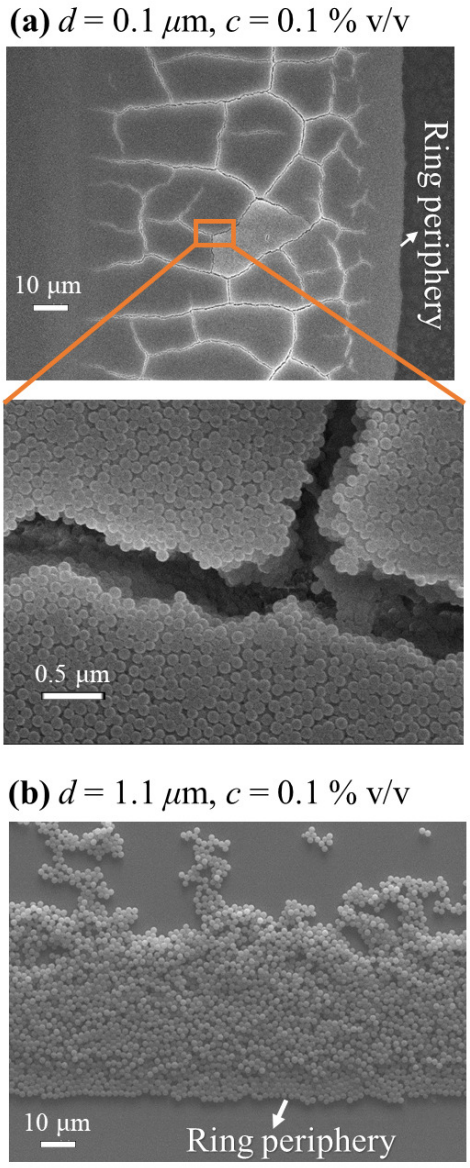

Figure 2.4: (a) SEM of the surface of the ring for 0.1 μm at concentration of 0.1 %v/v. (b) SEM of the surface of the ring for 1.1 μm at concentration of 0.1 %v/v.

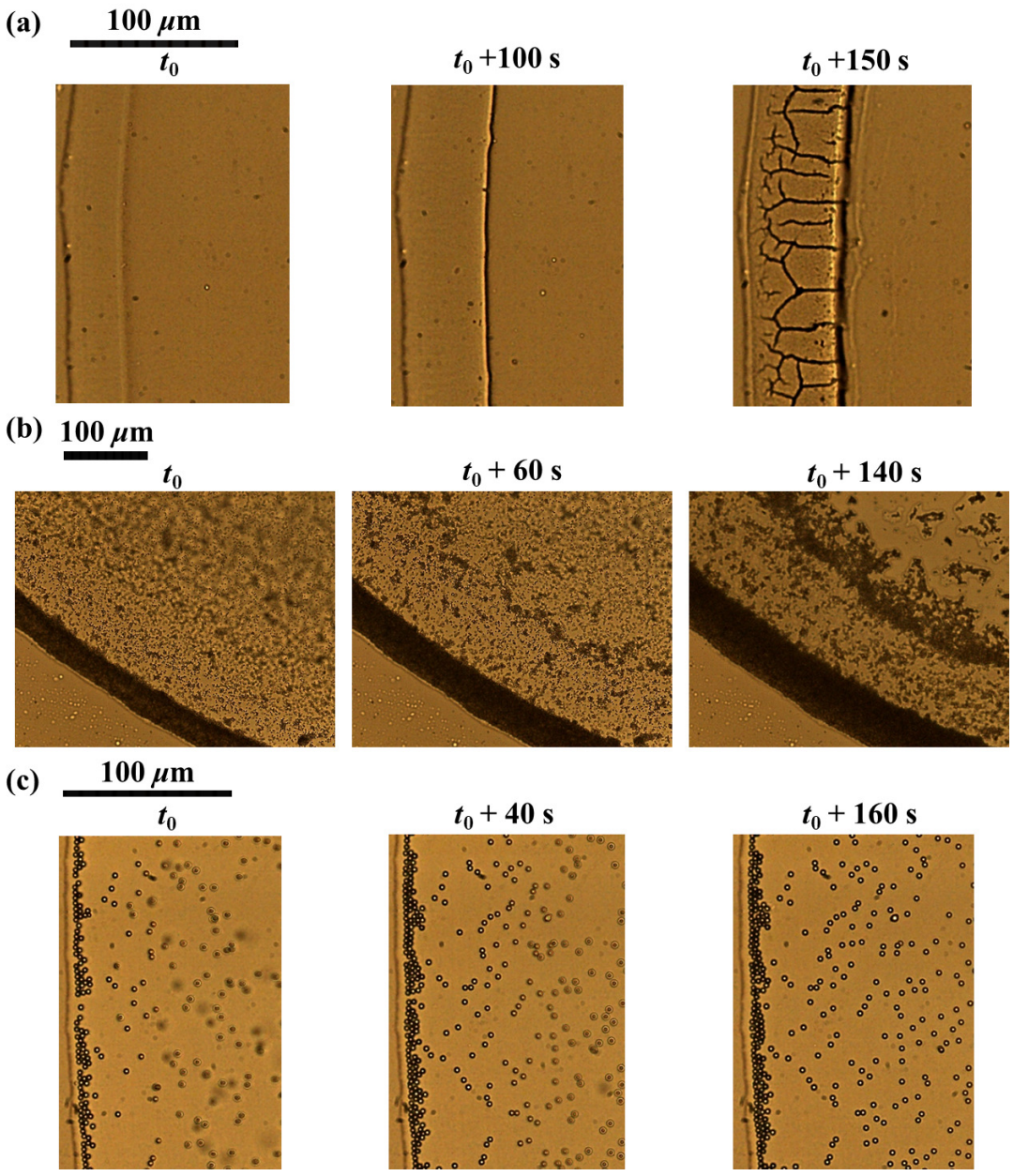

Figure 2.5: Time-sequence of images showing ring formation in last stage of evaporation at $c = 0.1$ % for three cases of particles size (a) $d = 0.1$ μm (b) $d = 1.1$ μm (c) $d = 3.0$ μm. The ring periphery is on the left in each frame. Respective scale bar is shown on the top of each row.

2.5.1.2 Measurement of ring profiles

Figure 2.6 compares the measured ring profiles for different particle concentration (c = 0.001, 0.01, 0.1 and 1.0 %v/v), keeping particle size constant. Note that the origin is located at the outer periphery of the ring. An isometric view of the ring obtained by optical profilometer is plotted in the insets of Figure 2.6. In Figure 2.6(a), at $d = 0.1$ μm, the ring profile resembles a partial torus-like shape and such a profile is attributed to a build-up of particles at the contact line due to the outward flow in the initial stages of the evaporation [37] and depinning of the contact line from growing deposit in last stages of the evaporation. The ring height (h) and width (w) increase with the particle concentration (c). Since the maximum ring height (h) is larger than the particle size in all cases of concentration, the particles are clearly stacked in multiple layers in the ring. The increase in the ring width with concentration at $d = 0.1$ μm is qualitatively confirmed in the first row of Figure 2.3. In Figure 2.6(b), at $d = 1.1$ μm, the maximum ring height is almost equal to particle size ($h \approx 1.1$ μm) for $c = 0.001$, and 0.01 %. However, for $c = 0.1$, and 1.0 %, the ring height is larger than the particle size ($h > 1.1$ μm). Therefore, the particles form a monolayer (a single layer of the particles) in the ring at $c = 0.001$, and 0.01 % for d = 1.1 μm.

The monolayer is discontinuous and continuous at $c = 0.001$, and 0.01 %, respectively, as confirmed from optical microscopy images in Figure 2.3 (first two frames in the second row). At $c = 0.1$ and 1.0 %, the ring width increases with an increase in particle concentration. In Figure 2.6(c), at $d = 3.0$ μm, the maximum ring height (h) is same as the particle diameter for $c = 0.001$, 0.01, and 0.1 %, corresponding to a monolayer ($h \approx d$). At $c = 1.0$ %, the ring height and width increase with an increase in the particle concentration, qualitatively shown in the third row of Figure 2.3. The monolayers are discontinuous for $c = 0.001$, 0.01 % while the monolayer is continuous for $c = 0.1$ %. The mechanism of the formation of the monolayer in Figure 2.6(b) and (c) at low concentration was explained earlier in section 3.5.1. However, for larger concentrations at larger particle sizes, there is a sufficient number of particles available in the droplet which stack up as multiple layers near the contact line.

Further the deposit profile is quantified by measuring the slope at the outer edge (contact line). Table 2.4 lists the measured angle using the profiles and the cases in which monolayer forms are not listed. As expected, the higher the concentration the larger the slope, as these structures can be built quicker, before the dynamic contact angle drops due to evaporation. The slope is slightly larger for $d = 1.1$ μm, as compared to $d = 0.1$ μm since the initial contact angle in the former and latter cases are 35° and 33°, respectively.

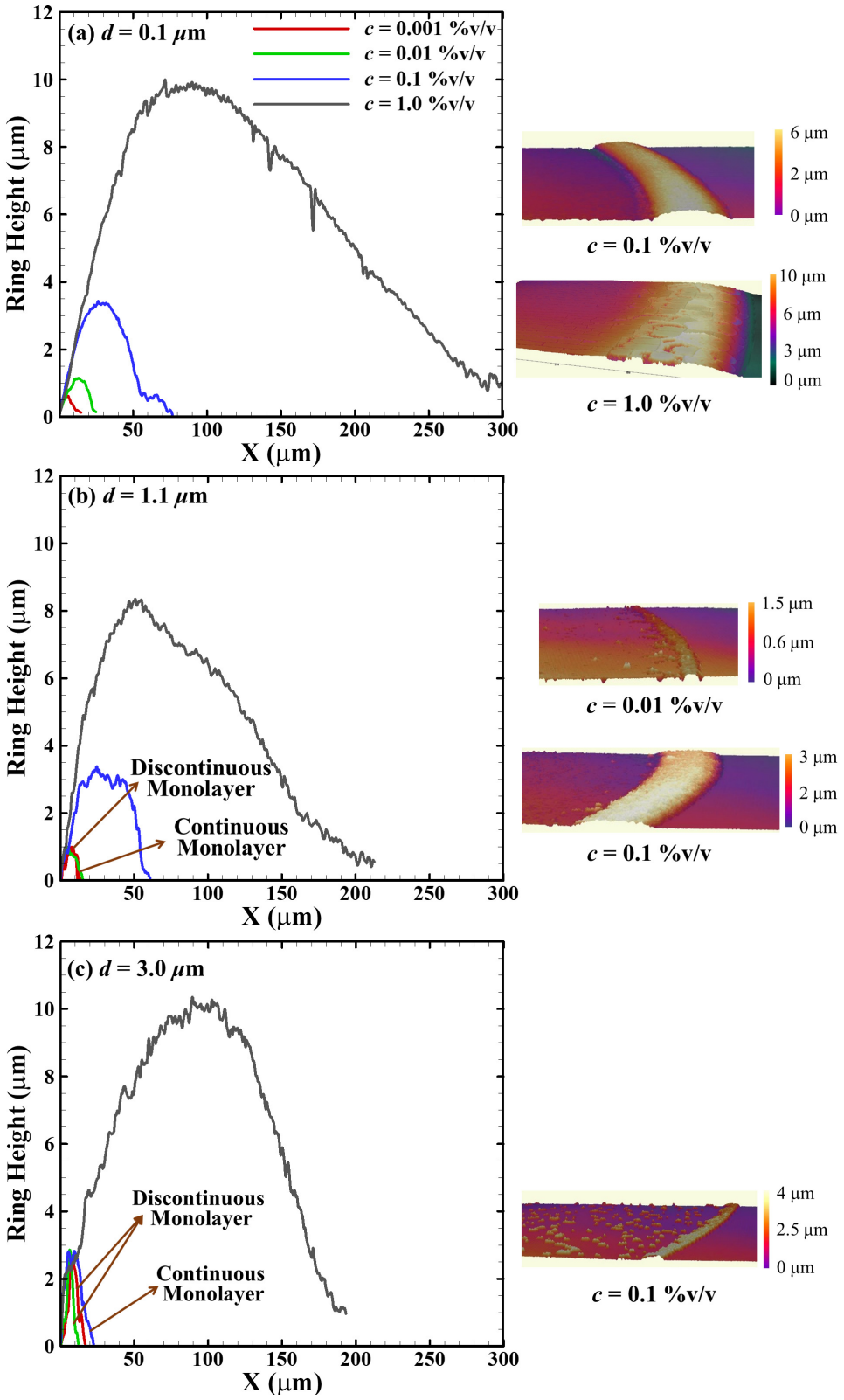

Figure 2.6: Average ring profiles plotted for different cases of particles size (a) $d = 0.1\ \mu$m, (b) $d = 1.1\ \mu$m, and (c) $d = 3.0\ \mu$m. For each case, different cases of concentrations, c = 0.001, 0.01, 0.1 and 1.0 % are plotted. X represents the radial coordinate and X = 0 is the contact line. 3D ring profiles obtained from an optical profilometer for some cases are shown in the right column.

Cases	$d = 0.1$ (μm)	$d = 1.1$ (μm)
$c = 0.001$ %	8.6°	
$c = 0.01$ %	8.5°	
$c = 0.1$ %	10.7°	12.6°
$c = 1.0$ %	11.3°	14.7°

Table 2.4: Measured slope (in degrees) of the deposit profiles at outer edge of the ring for different cases of particles concentration (c) and particle size (d).

2.5.1.3 Regime map

A regime map is plotted to classify monolayer and multiple layer ring formation on particle concentration-particle size plane in Figure 2.7. The discontinuous or continuous monolayer ring occur for larger particle size combined with low concentration, while deposits of multiple layers form at smaller particle size and larger concentration. Dashed line demarcates qualitatively the three regimes and the cracks form in two cases of multiple layers, as shown in Figure 2.7. Our measurements show that the formation of the monolayer occurs at a critical concentration at a constant particle diameter or a critical particle diameter at a constant particle concentration.

The percentage of the mass of the particles present in the ring with respect to the total mass of the particles in the droplet (ξ) is also estimated for cases of continuous monolayer and multiple layers. The mass of the ring ($M_{ring,exp}$) is estimated by the following expression,

$$M_{ring,exp} = \int_{R_w - \triangle R}^{R_w} \rho\, p\, f(R) 2\pi R\, dR, \tag{2.4}$$

where ρ, $p\ f(R)$, R_w, $\triangle R$ are particle density, particle packing fraction, ring profile, wetted radius, and ring width, respectively. The ring profile is obtained by fitting a second-order polynomial curve using the least-square fitting method to the measured ring profile. Figure 2.7 shows the values of ξ for all cases except those for discontinuous monolayer ring. At smaller particle size, a large amount of particle mass deposits in case of multiple layers, as shown in Figure 2.7. The continuous monolayer ring cases show a lesser deposition as compared to multiple layers due to the deposition of the particles in the inner region in the continuous monolayer ring. For example, the minimum ξ (around 27%) corresponds to the case of $d = 3.0$ μm and $c = 0.1$ %v/v, in which a monolayer ring forms and multiple rings are observed along with the outer ring (Figure 2.2).

2.5.1.4 Scaling of ring dimensions with particles concentration

A comparison study is done on the scaling of the ring dimensions with predictions of a model, proposed by Popov [100], based on the conservation of the mass of droplet liquid

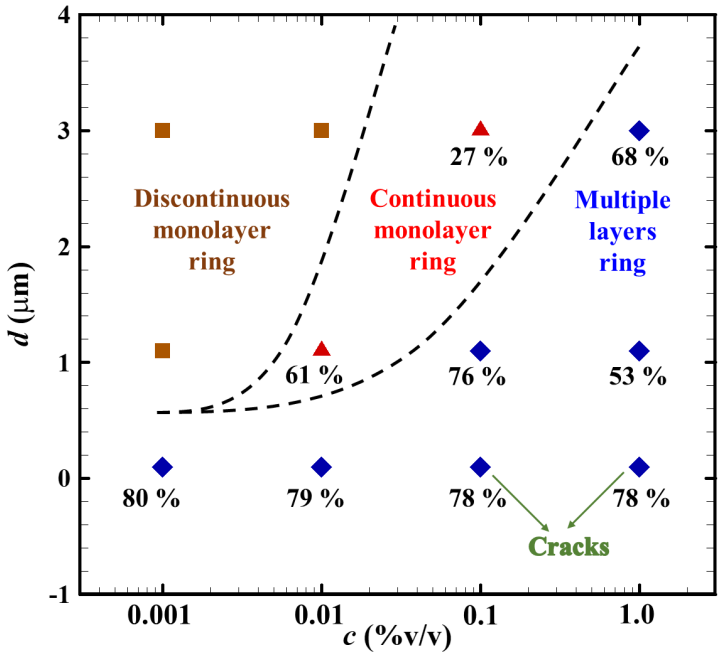

Figure 2.7: Regime map for classifying regimes of the discontinuous monolayer, continuous monolayer and multiple layers on particle size - particle concentration plane. Dashed lines serve as a guide to the eye to demarcate the regimes. Percentage of the mass of particles deposited in the ring is given for each case except in regime of the discontinuous monolayer.

and particles during the evaporation. The model treats the particles as continua and ignores immersion capillary forces among the particles during the formation of the monolayer ring. Therefore, the comparison of the data of $d = 1.1$ μm and $d = 3.0$ μm is not done against the model since monolayer rings form in this case at low concentrations. In this model, the non-dimensional ring width (W) and height (H) are expressed, respectively, as follows,

$$W = w/R = 0.6\sqrt{(c/p)} \tag{2.5}$$

$$H = h/R = 0.3\theta_c\sqrt{(c/p)} \tag{2.6}$$

where w, h, c, p, θ_c, R are ring width, ring height, particle concentration, particle packing fraction, static contact angle, and initial droplet wetted radius, respectively. The value of p is taken as 0.656 from Ref. [42].

Figure 2.8(a) and (b) shows the qualitative comparison between the present measurements for $d = 0.1$ μm and model predictions for W and H, respectively, as a function of particle concentration (c) on a log-log scale. The measurements of $d = 1.1$ μm and $d = 3.0$ μm including those result in the monolayer are also plotted in Figure 2.8. The model predicts the same value of W for all particle sizes, whilst H varies slightly with size due to the dependence of the H on θ_c ($H = h/R = 0.3\theta_c\sqrt{(c/p)}$), due to the assumption of a wedge-like contact line region in the model (Figure 2.9). The measured width and height of the ring scales non-linearly with particle concentration i.e. $W \sim c^m$ and $H \sim c^n$. The values of m and n obtained using least squares curve fitting method for $d = 0.1$ μm are 0.55 and 0.41, respectively, both values are closer to 0.5, as predicted by the model.

Interestingly, the model underpredicts and overpredicts the width (Figure 2.8(a)) and height (Figure 2.8(b)) as compared to the measurements, respectively. This is attributed to the fact that the model presents the shape of the ring profile as a wedge-like region near the contact line (Figure 2.9) and it does not account for the interaction of the shrinking free surface with the growing deposit in the last stage of the evaporation [32], which results in a typical partial torus-like profile of the ring. To verify this hypothesis, the mass of the particles in the ring obtained in the measurements ($M_{ring,exp}$) and predicted by the model ($M_{ring,model}$) are compared at different particles size and concentrations for multiple layer ring cases. $M_{ring,exp}$ was estimated, as explained previously. $M_{ring,model}$ was calculated by approximating a wedge-like area to a triangle and integrating it over the wetted radius as the following expression,

$$M_{ring,model} = \rho_p p \pi R w h, \tag{2.7}$$

Figure 2.10 shows the comparison between $M_{ring,exp}$, and $M_{ring,model}$ at different par-

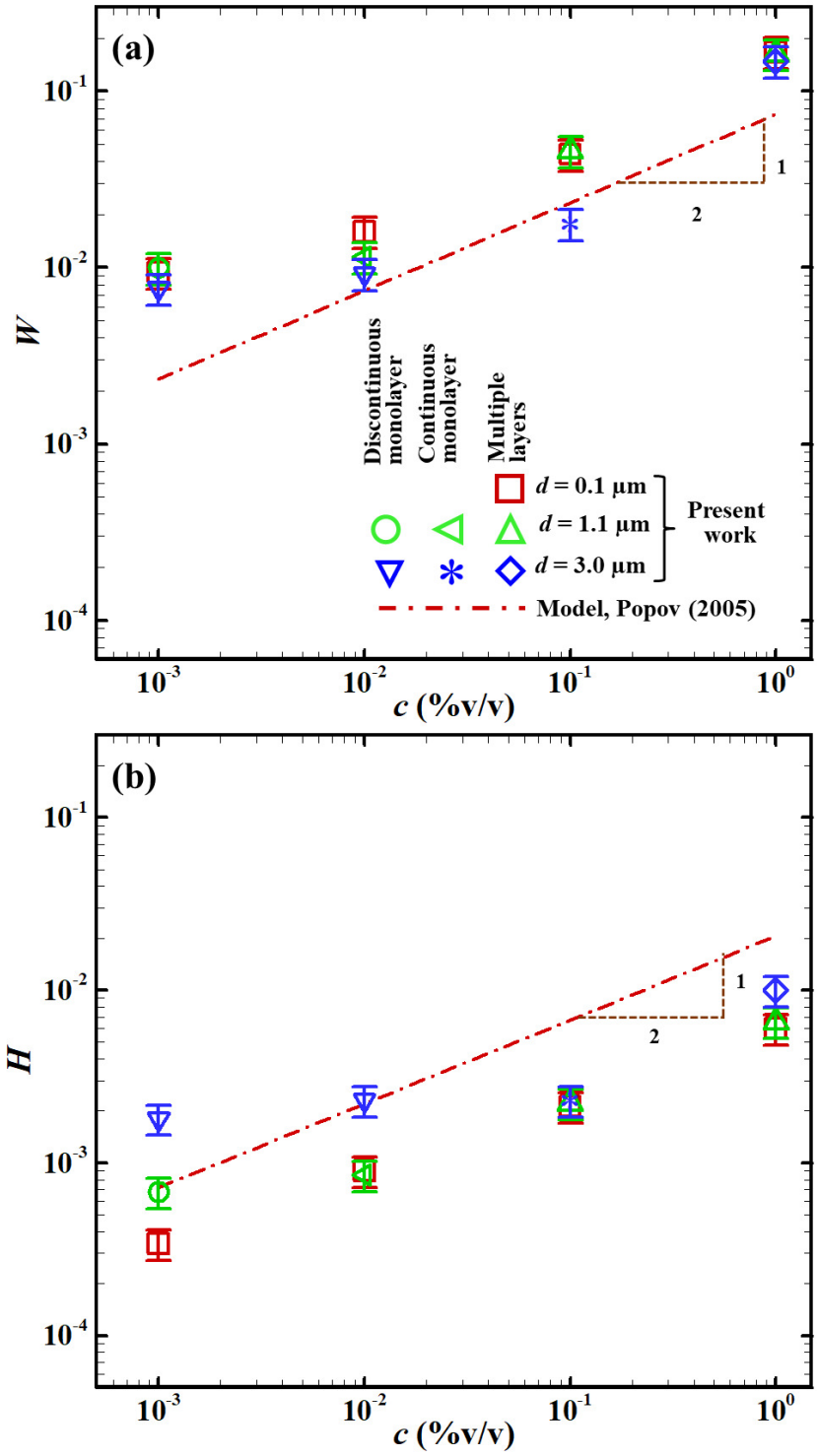

Figure 2.8: Comparison of measured ring dimensions with model predictions at different particles size, d and particles concentration, c. (a) Non-dimensional ring width (W) (b) Non-dimensional ring height (H). Symbol and broken line represent measurement and model prediction, respectively.

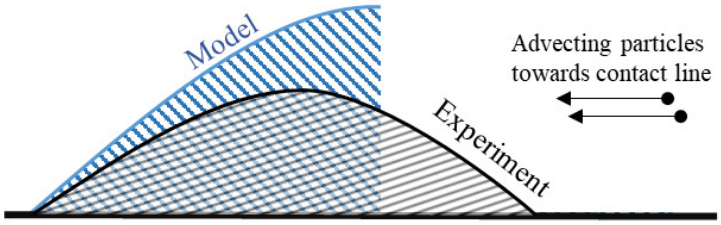

Figure 2.9: Schematic showing a comparison between assumed ring-profile in the model and measured profile.

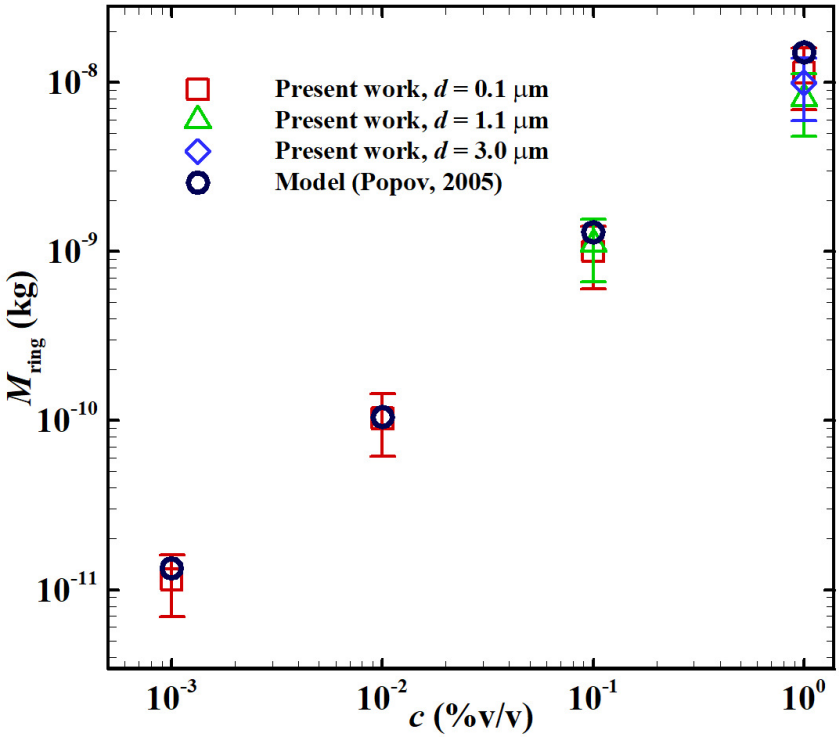

Figure 2.10: Comparison between the mass of the particles in the ring obtained by the measurements and the model at $d = 0.1$, 1.1, and 3.0 μm and different concentrations for multiple layer ring cases.

ticles size and concentrations for multiple layer ring cases. The measured mass is on the same order of the mass predicted by the model. Therefore, in the last stage of drying, the spreading of the ring at the expense of its height is noted and is explained by the interaction of the growing deposit with shrinking free surface. The interaction is not captured by the model proposed by Popov [100].

This hypothesis is further verified by comparing dynamics of the deposition of the particles for the formation of the monolayer for $d = 3$ μm, with predictions of a model, proposed by Deegan et al. [101]. In this model, the number of particles migrating towards the contact line at a given time, t, follows a power law given by, $N \sim t^{2/1+\lambda}$ [101], where λ is a function of the initial static contact angle (θ_c), $\lambda = (\pi - 2\,\theta_c)/(2\,\pi - 2\,\theta_c)$. The number of particles migrating towards the contact line is measured for case $d = 3.0$ μm and $c = 0.1$ % (visual-

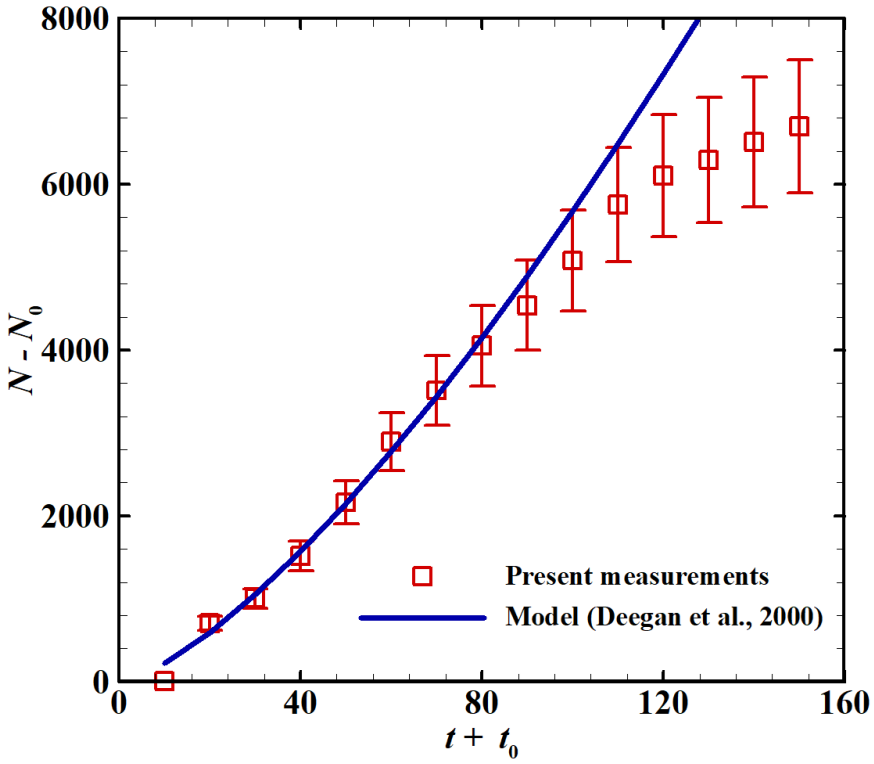

Figure 2.11: Count of particles advecting near the contact line as a function of time at $d = 3.0\ \mu$m and $c = 0.1$ %

ization of the particle motion of this case is plotted in Figure 2.5). Figure 2.11 shows that the present measurements agree well with the $N - t$ relationship predicted by the model, where $\lambda = 0.35$, at $t \leq 80$ s. The model does not account for the interaction of the growing deposit with shrinking surface and the difference between the model prediction and measurement start to increase at $t > 80$ s. As explained earlier, the ring spreads at the expense of its height during this interaction. The contact line recedes at t $\approx$ 120 s, resulting in the formation of a monolayer of particles in the ring.

2.5.2 Graphene nanoplatelets

The results of evaporation of sessile water droplet containing graphene nanoplatelets are presented. The concentration (c) of the graphene nanoplatelets is varied from [0.01 - 0.1] %v/v. The diluted solutions of the graphene nanoplatelets are characterized by measuring the thermal conductivity (k) of each solution. Thermal analyzer KD2 Pro (Decagon devices) is used for thermal conductivity measurements. Figure 2.12 shows the k (W/m-K) values measured for the graphene nanoplatelet dispersed in water solutions of various concentrations [0.0001 - 0.1] %v/v. The k (W/m-K) values indicate that there is little variation in the thermal conductivity of the solution due to the presence of graphene nanoplatelets in comparison to deionized water. This signifies that individual graphene flake in the di-

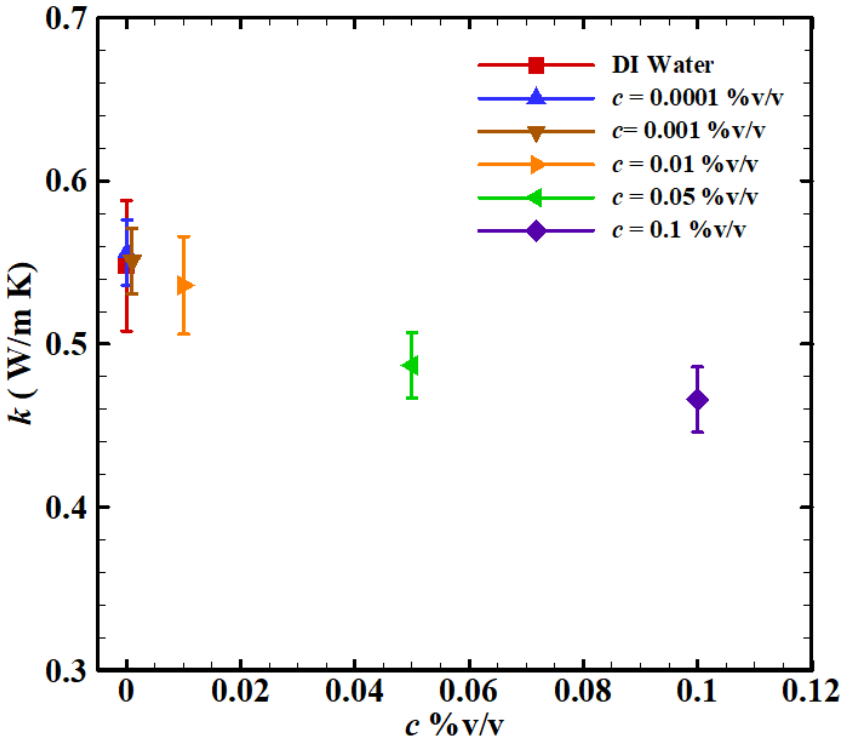

Figure 2.12: Thermal conductivity characterization of the water-based graphene nanoplatelet solutions of different concentrations

luted solution remains isolated without any percolation. The k value of all the solutions lies around 0.5 W/m-K.

The final deposit patterns obtained after the evaporation of 1.1 ± 0.2 μL, sessile water droplets containing graphene nanoplatelets of various concentrations at ambient conditions are studied in this section. Figure 2.13(a) shows the final deposit pattern images obtained by high-speed camera, for the concentrations, c = [0.01, 0.03, 0.07, and 0.1] %v/v. The final dried patterns show the coffee-ring [37], similar to the polystyrene particles. Since the evaporating flux is maximum at the contact line owing to the largest surface area; the ring is formed by convection inside the droplet bringing the inner particles to the outer area. With the increase in the concentration of the graphene nanoplatelets, the coffee-ring width and the distribution of the graphene nanoplatelets inside the coffee-ring increases. As seen in Figure 2.13(a) for c = 0.1 %v/v, a larger amount of graphene nanoplatelets are deposited in the inner region of the ring. Figure 2.13(b) shows the isometric view of a coffee-ring section of the dried patterns shown in Figure 2.13(a). Figure 2.13(c) compares the coffee-ring profiles of graphene nanoplatelets at various concentrations. X = 0 μm indicates the contact line from where ring growth starts. At c = [0.01 and 0.03] %v/v, ring height is around 0.6 μm, and ring width is around 22 μm. At higher concentrations, c = [0.07, and 0.1] %v/v, ring height remains the same i.e., around 0.6-0.7 μm. However, the ring width increases to around 60 μm. Thus, excess graphene nanoplatelets in the larger

concentration solutions tend to increase the ring width. Smaller ring heights are observed in case of graphene suspensions, contrary to the ring heights obtained from polystyrene particles (greater than 2-3 μm) that remain on the substrate as a monolayer or stacked. The graphene nanoplatelets are 2D flakes type structures and by the time the liquid evaporates, the bulk of the suspensions have deposited as a coating on the surface. With the increase in the concentration, the rest of the suspensions, which have not radially flown with the liquid towards the contact line, tends to sediment on the inner region due to the shrinking liquid-air interface with the evaporation.

2.6 Closure

The ring-like deposits obtained after the evaporation of a sessile water droplet containing polystyrene colloidal particles on a glass substrate is studied. The coupled effect of the particle size (d) and particles concentration (c) on ring dimensions and morphology have been investigated. The range of d and c in the experiments are [0.1, 3] μm and [0.001, 1] %v/v, respectively. The effect of particles concentration on the dried patterns of the aqueous droplet containing graphene nanoplatelets is also investigated. The concentration of the graphene nanoplatelets is varied from $c = [0.01 - 0.1]$ % v/v. The dried patterns were visualized under an optical microscope and the ring profiles were measured by an optical profilometer. The measured ring profiles resemble a partial torus-like shape for all cases of d and c. Cracks on the surface of the ring for $d = 0.1$ μm and $c = 0.1$, and 1.0 % are visualized and their formation is briefly explained. Three types of deposits are classified on particles concentration - particle size plane, namely, discontinuous monolayer ring, continuous monolayer ring, and multiple layers ring. In the case of multiple layers, the ring width and height increases with an increase in particles concentration and relative mass of the particles accumulated in the ring is the largest at the lowest particle size.

The monolayer ring forms due to larger immersion capillary forces among the particles at larger particle size and measured particle motion near the contact line qualitatively confirm the interaction among the particles. A critical particle concentration exists at a given particle size to achieve its formation. The qualitative measured variation of the ring dimensions with particles concentration is consistent with the predictions of an existing theoretical model at $d = 0.1$ μm. The measured dimensions of the ring scale with particles concentration by a power law and in general, the scaling agrees with the predictions of the model. The time-varying ring dimensions is compared with the model and the conclusion is that a growing ring spreads in the last stage of drying at the expense of its height due to its interaction with shrinking free surface. The graphene nanoplatelets are having 2D flakes type structure that remain on the substrate as a coating. The ring heights obtained from the graphene nanoplataelts are lesser than that obtained from the polystyrene particles. With

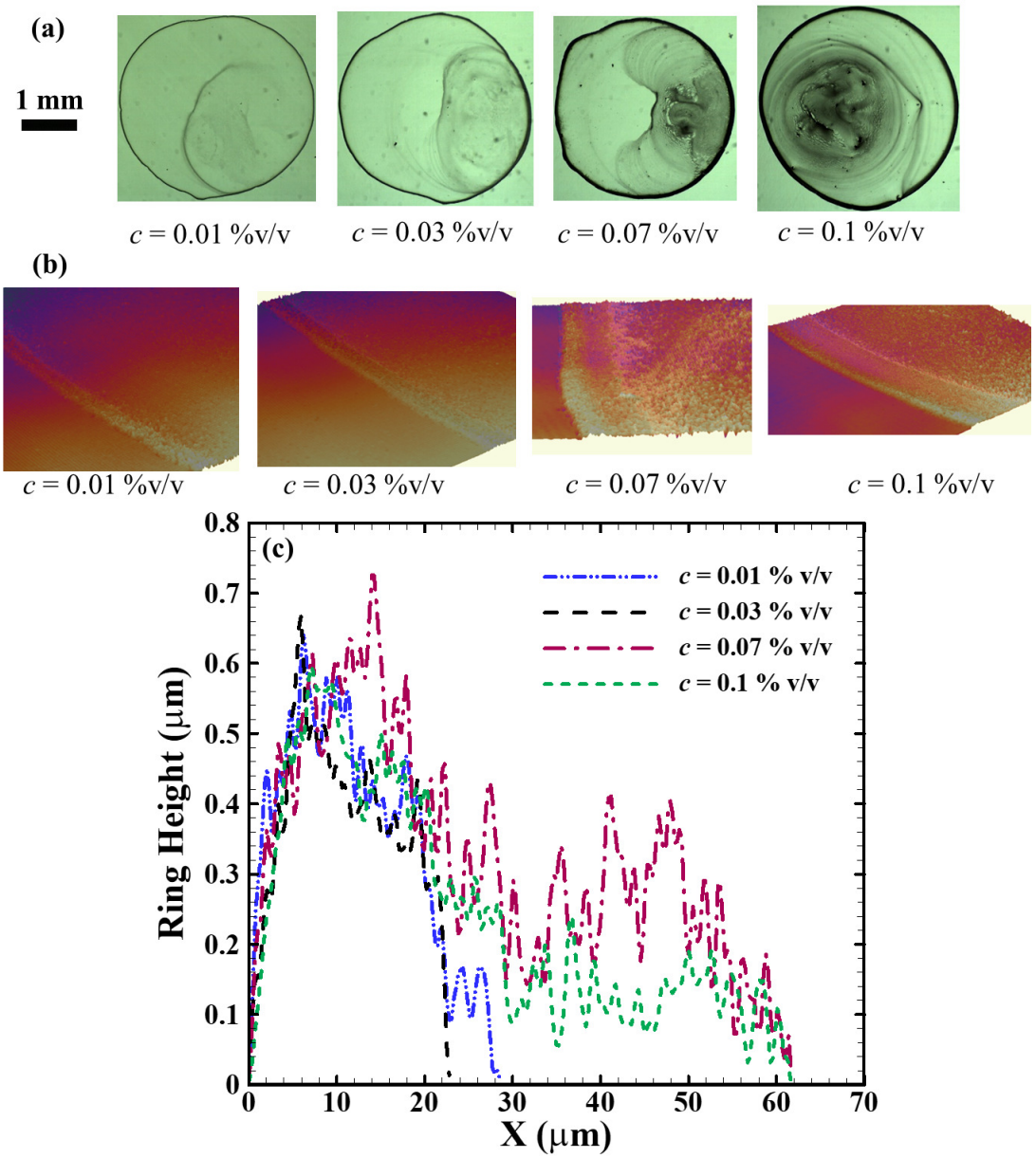

Figure 2.13: (a) Dried patterns obtained after the evaporation of the water-based graphene nanoplatelet solutions of concentrations, c = [0.01 - 0.1] %v/v. The scale is shown in the left side. (b) Isometric view of the ring profiles for the above cases, taken by a 3D optical profilometer. (c) Ring profiles measured for evaporation of water-based graphene nanoplatelets solutions of different concentrations.

increase in the graphene nanoplatelets concentration, the ring width and intensity of inner deposits also increases. Overall, the present study provides fundamental insights into the dependence of the ring profile and dimensions on particle size and particles concentration. Our results will help to design technical applications such as inkjet-printing and manufacturing of bioassays.

Chapter 3

Colloidal Deposit of an Evaporating Aqueous Droplet on a Non-uniformly Heated Substrate[1]

The pattern and profile of a dried colloidal deposit formed after evaporation of a sessile water droplet containing polystyrene particles on a non-uniformly heated glass are investigated experimentally. In particular, the effects of temperature gradient across the substrate and particles size are investigated. The temperature gradient was imposed using Peltier coolers, and side visualization, infrared thermography, optical microscopy, and optical profilometry were employed to collect the data. On a uniformly heated substrate, a ring with an inner deposit is obtained, which is attributed to axisymmetric Marangoni recirculation and consistent with previous reports. However, the dimensions of the ring formed on a non-uniformly heated substrate are significantly different on the hot and cold side of the substrate and are found to be a function of the temperature gradient and particles size. In the case of smaller particle size, the contact line on hot side depins and together with twin asymmetric Marangoni recirculations, it results in a larger ring width on the cold side as compared to the hot side. In contrast, the contact line remains pinned in case of larger particles, and the twin asymmetric Marangoni recirculations advect more particles on the hot side, resulting in a larger ring width at the hot side. A mechanistic model is employed to explain why the depinning is dependent on the particle size. A larger temperature gradient significantly increases or decreases the ring width depending on the particle size, due to a stronger intensity recirculation. A regime map is proposed for the deposit patterns on temperature gradient-particle size plane to classify the deposits.

[1] **LK Malla**, R Bhardwaj, A Neild, "Colloidal deposits obtained after evaporation on a non-uniformly heated surface." *Colloids and Surfaces A : Physicochemical and Engineering Aspects*, doi: 10.1016j.colsurfa2019.124009. https://www.sciencedirect.com/science/article/pii/S0927775719310003

Graphical abstract: The evaporation dynamics of a microliter water droplet containing polystyrene colloidal particles on a heated glass substrate at nonuniform temperature, recorded by high-speed visualization, infrared thermography and optical microscopy to study effect of the particles diameter and temperature gradient on the morphology and dimensions of the ring formed.

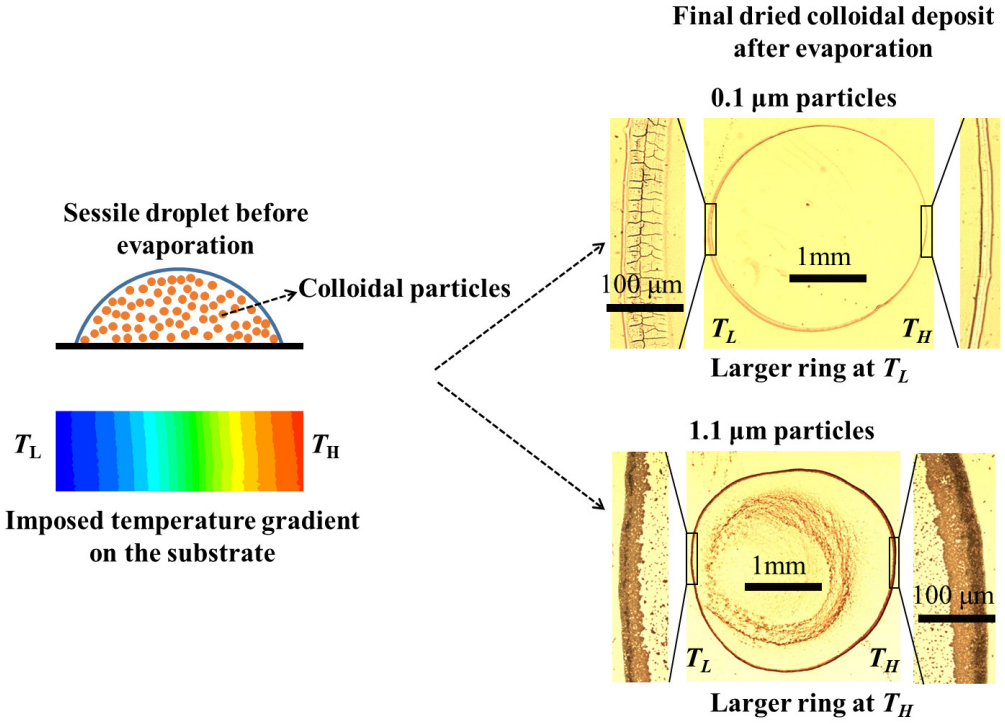

3.1 Introduction

In order to engineer the deposit pattern and shape, previous studies have reported the effect of several parameters on final deposit pattern such as particles size, particles shape, concentration, hydrophobicity of the particles, pH of the colloidal suspension, substrate temperature, substrate wettability, relative humidity, electrowetting, etc (see discussion notable reviews [44, 45, 62, 102–104]). One important parameter in this arena is substrate temperature that has gained significant attention since 2015 [9, 20, 49]. The focus of the present work is a non-uniformly heated substrate, that could help to design innovative applications. For example, droplet migration caused by Marangoni stresses on a surface with a temperature gradient is useful for developing microfluidic or lab-on-a-chip technologies, such as one demonstrated in Ref. [105]. In the following, previous studies that tackled the coffee-ring effect on a uniformly non-heated and uniformly heated substrate have been discussed. In order to provide context to the non-uniformly heated substrate, previous studies on evaporation of droplets of pure liquid on such a substrate have also been discussed.

3.2 Literature review

3.2.1 Studies on uniformly heated substrate

The role of Marangoni flow on the particle deposition on a uniformly non-heated substrate has been studied extensively. Hu and Larson [46] reported the inner deposits near the center of a dried microliter octane droplet. Ristenpart et al. [106] reported the dried patterns with inner deposits obtained on evaporating isopropanol, chloroform, methanol, and ethanol droplet containing colloidal suspensions on PDMS surface. They also showed the dependency of the direction of the Marangoni flow on the substrate and liquid thermal conductivity ratio. Bhardwaj et al. [32] reported a central bump pattern obtained on evaporating nanoliter isopropanol droplet on a PDMS substrate. Xu et al. [107] showed that the Marangoni flow reverses direction at critical contact angle, which is dependent on the ratio of substrate to liquid thermal conductivity and the ratio of substrate thickness to wetted radius of droplet. Weon and Je [69] showed that small colloids ($d = 0.1$ μm) and large colloids ($d = 1.0$ μm) tends to form ring and ring with an inner deposit, respectively, for a decalin droplet and in a bi-dispersed mixture solution, fingering-like ring patterns are formed due to the competition between the outward radial flow and the inward Marangoni flow. Similarly, Trybala et al. [108] reported a spot-like and ring-like dried patterns for the evaporation of aqueous solutions of carbon and TiO2 nanoparticles on a polyethylene film, respectively. The former pattern was attributed to the Marangoni recirculation.

In the context of a uniformly heated substrate, Girard et al. [109] mapped the time-varying liquid-air interface temperature of an evaporating pure water droplet using infrared thermography. They reported that the temperature difference between the contact line and the droplet apex decreases with time. Regarding colloidal suspensions, Li et al. [9] reported the deposition patterns obtained after evaporation of a droplet containing 0.25% v/v polystyrene nanoparticles on a glass substrate heated from 30°C to 80°C. They found that due to the inward flow of the particles owing to Marangoni convection on a heated substrate, the “coffee-ring” changes to “coffee-eye”. Parsa et al. [49] reported the formation of a dual-ring pattern at the elevated substrate temperatures of 47, 64, and 81°C due to the ring-like cluster built-up of the particles on the liquid-air interface, owing to the Marangoni flow. They reported that a further increase in the temperature to 99°C led to the formation of multiple rings due to the stick-slip motion of the contact line. Zhong and Duan [110] also reported the formation of dual-ring patterns with the same mechanism for the evaporation of aqueous droplets containing graphite nano-powders on silicon wafers, heated at 50°C. In a follow-up study [111], they reported the suppression of dual ring at 84°C due to the enhanced outward radial flow in comparison to the Marangoni flow.

Patil et al. [20] studied the deposition patterns of polystyrene particles on glass and silicon wafers heated from 27°C to 90°C at different particles concentrations in an aqueous

droplet. They reported the thinning of the ring width with an increase in the substrate temperature. In a follow-up study, Patil et al. [7] reported that with an increase in the substrate temperature, the receding angle of an aqueous droplet containing smaller polystyrene particles ($d = 0.1\ \mu$m) reduces on a silicon wafer, which helps in pinning of the contact line and formation of a thin ring along with an inner deposit due to the Marangoni recirculation. Regarding bi-dispersed colloidal suspensions, Parsa et al. [112] reported the self-sorting of 1.0 μm particles towards the outer edge of the ring in the evaporation of a bi-dispersed solution containing 1.0 and 3.2 μm particles on a uniform heated substrate. Similarly, the self-sorting of the smaller particles near the contact line was reported by Patil et al. [7] during the evaporation of a bi-dispersed solution containing smaller (0.1 and 0.46 μm) and larger particles (3.0 μm) on a heated silicon wafer.

3.2.2 Studies on non-uniformly heated substrate

In the context of the non-uniformly heated substrate, several studies reported migration of a pure liquid droplet on the surface with low contact angle hysteresis (CAH) and attributed this migration to Marangoni stresses. Brzoska et al. [113] reported PDMS droplet movement form hot side to cold side on silanized Si wafers which have a low contact angle hysteresis (around 2°). They theoretically found that for a given temperature gradient, droplets above a critical wetted radius will move. The temperature gradient on the substrate was varied from 0.35 to 1.08°C/mm. Notably, they reported that the internal flow direction is from the hot side to the cold side along the liquid-gas interface. Tseng et al. [114] numerically studied silicone droplets (0.1 – 2 μl) movement towards the cold side on a hydrophobic surface having a temperature gradient of 100 °C/mm. They reported that the movement is due to the difference in the momentum transfer owing to asymmetry in the Marangoni vortices. Chen et al. [115] studied the thermocapillary migration of the droplets on DTS- and OTS-coated Si wafers. The droplets were having low contact angle hysteresis (less than 3°) on the substrates and the droplet migration speed decreases with the increase in the hysteresis.

Nguyen and Chen [116] numerically found that the migration diminishes for the droplet with a smaller static contact angle (SCA) and is larger for droplets with SCA greater than 90°. They reported the two asymmetric Marangoni vortices inside the droplet, which is larger on the hot side in comparison to the cold side. Nguyen and Chen [117] reported that the effect of buoyancy convection on smaller droplets (wetted radius less than 2 mm) is negligible in comparison to thermocapillary convection due to an imposed temperature gradient. Bakli et al.[118] simulated the thermocapillary migration of a nanoliter droplet and observed that the droplet moves toward the colder surface on the large wettable surface whereas, the reverse occurs on the less wettable surface. Foroutan et al. [119] through

molecular dynamics simulations reported the translational as well as rotational motion of a nanodroplet on a graphene substrate when subjected to a temperature gradient. Recently, Ouenzerfi and Harmand [120] observed the opposite migration of water-3% butanol binary droplet, i.e., from the cold side to the hot side, on a substrate with 0.5°C/mm gradient. Authors attributed it to increase in surface tension of the binary liquid with temperature beyond a critical temperature.

In contrast, the droplet does not migrate on a nonuniform heated surface with larger CAH. Recent studies have measured flow-field in an evaporating droplet on low CAH surface. The surface tension is lower on the air-liquid interface at the higher temperature side of the contact line of the droplet than at the lower temperature end. The surface tension gradient creates a twin Marangoni recirculation, in which the flow direction is from the hot side to the cold side along the interface, as experimentally visualised by Pradhan and Panigrahi [121] in a droplet with 1.9 mm wetted diameter with an imposed temperature gradient of 1.8°C/mm. Similarly, such twin recirculations were visualized through infrared thermography by Askounis et al. [122] in an evaporating water droplet on a copper substrate, locally heated by a laser at a point near the contact line.

3.3 Objectives

A brief literature review shows while the effect of the temperature gradient across the substrate on thermocapillary migration and internal flow fields inside pure liquid droplets is well-established, there are no reports of the evaporation of the droplets of colloidal suspensions on a non-uniformly heated substrate, to the best of our knowledge. Therefore, the primary objective of the present work is to investigate the pattern and profile of dried colloidal deposits on the non-uniformly heated substrate. In particular, the effect of particle size and intensity of temperature gradient on the deposits are presented. The present work utilizes the system with large contact angle hysteresis in order to avoid droplet migration.

3.4 Experimental details

3.4.1 Generation of droplets of colloidal suspensions on glass

Aqueous colloidal suspensions of 10 %v/v of uniformly dispersed polystyrene latex beads of diameter $d = 0.1$ (LB1), 1.1 (LB11), and 3.0 μm (LB30) were obtained from Sigma Aldrich Inc. The suspensions were used as procured from the manufacturer and were diluted by deionized water (resistivity of 18.2 MΩ·cm) to prepare a solutions of concentrations, $c =$ 0.05, 0.1, and 0.5 %v/v. Once dilution was complete, solutions were sonicated for about

30 minutes to ensure a highly disperse sample. The properties of these suspensions are available through the manufacturer product information sheet [123] and are briefly given as follows. The standard deviation of the diameter of the particles in the solution is on the order of 5-15% of the mean diameter. The density of the particles is around 1005 kg/m^3, implying they are neutrally buoyant and do not sediment on the substrate. The particles are hydrophilic and the contact angle, when attached to the air-water interface, is around 43° [124]. The measured zeta potential (measured through instrument ZetaSizer NanoZs, Malvern Instruments Ltd.) for the 1.1 μm particles in an aqueous solution with concentration of 0.1 % v/v is -26.1 mV. The surface charge density of the 1.1 μm particles in an aqueous solution is around -2 μC/cm^2, as reported in previous measurements [125]. Droplets of volume 1.0 $\pm$ 0.3 μL were generated using a micropipette (Prime, Biosystem Diagnostics Inc.) and were gently placed on the substrate. Pre-cleaned glass slides (Sigma Aldrich Inc., S8902 [126]) with dimensions of 75 x 25 x 1 mm^3 served as the substrate. The glass slide was washed with isopropanol and was allowed to completely dry in the ambient conditions for a few minutes before the droplet was deposited on it. A fresh glass slide was used to repeat or to perform a new experiment. The roughness of the slide was measured using AFM (MFP-3D Origin, Asylum/Oxford Instruments Inc.) in non-contact mode and root mean square value (R_a) is around 2.9 nm. The surface potential of the glass surface is around -40 to -15 mV, as reported in previous measurements [8, 127].

3.4.2 Non-uniform heating of the substrate

In order to impose a temperature gradient on the glass slide, two Peltier coolers (TEC-12706) were used, which were maintained at different temperatures by a microprocessor-based controller (TEC-1122-SV, Meerstetter Engineering GmbH, Switzerland), as schematically shown in Figure 3.1. The temperature controller utilized a DC power supply (Tektronix Inc, USA, 0-32 V, 6A). A thin copper plate of 0.4 mm thickness was mounted between the glass slide and the Peltier cooler using thermal paste. An aluminum block with fins served as a heat sink beneath the Peltier coolers. A similar approach was employed by Pradhan and Panigrahi [121]. An actual photograph of the experimental setup is shown in Figure 3.2.

We calculated the Soret coefficient (S_T) for polystyrene beads in a water solvent case, where S_T is defined as the ratio of the thermal diffusion coefficient (D_T) to the mass diffusion coefficient (D_M) [128–130]. The thermal diffusion coefficient (D_T) is given by the following expression [130],

$$D_T = \frac{2\beta_0 A_{131}}{9\pi\mu d} \tag{3.1}$$

where β_0, A_{131}, μ, d are thermal expansion coefficient of the solvent (210 x 10^{-6} 1/K), Hamaker constant between the particles in the solvent (1.0 x 10^{-20} J), dynamic viscosity of the solvent

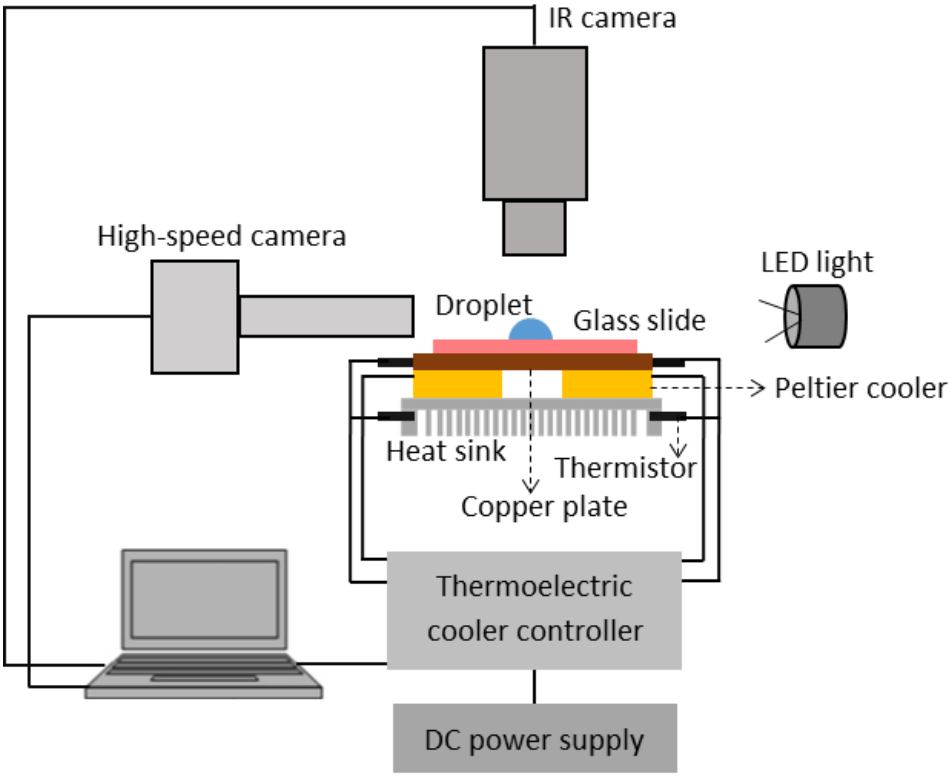

Figure 3.1: Schematic of the experimental setup used in the present study. Two Peltier coolers were used to impose a thermal gradient on the substrate. Infrared thermography and high-speed visualization were employed to map the temperature field on the liquid-gas interface and to record time-varying droplet shapes during the evaporation.

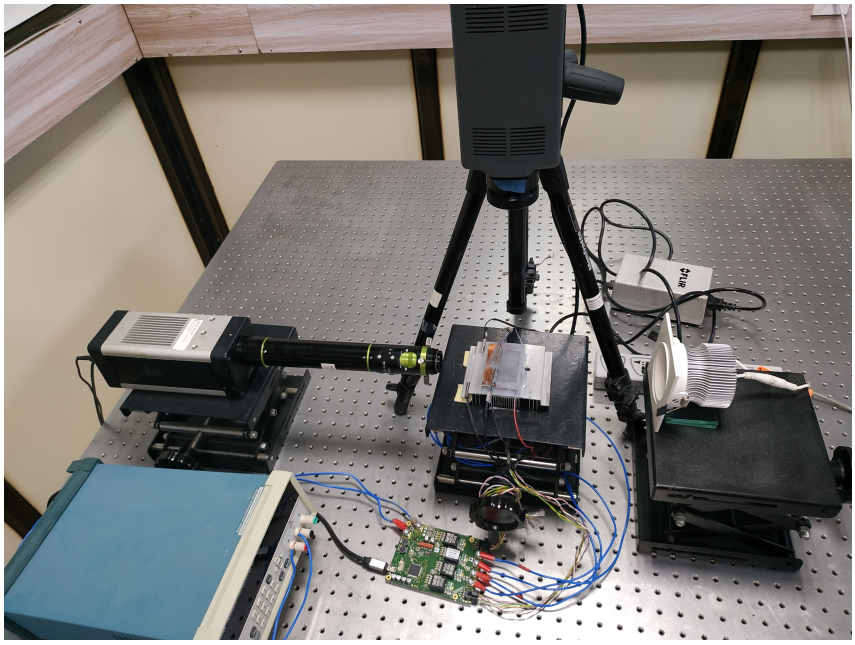

Figure 3.2: Photograph of the experimental setup

(8.9 x 10^{-4} Pa-s), and the particles diameter, respectively. The mass diffusion coefficient (D_M) is given by the Stokes-Einstein equation [8, 130] as follows,

$$D_M = \frac{k_B T}{3\pi\mu d} \tag{3.2}$$

where k_B, and T are Boltzmann constant (1.38 x 10^{-23} m^2.kg/s^2K) and temperature, respectively. The calculated S_T for the particles diameter [0.1 – 3.0] μm, lies in the order of 10^{-4}, which is considered negligible [131] and therefore, Soret effect is excluded in the present measurements.

3.4.3 Thermal imaging

The temperature field on the top of the substrate was measured using an infrared (IR) camera (A6703sc, FLIR Systems Inc.), with a 25 mm (f/2.5) IR lens (Figure 3.1 and Figure 3.2). For the droplet, the measured temperature is at the liquid-gas interface temperature since water is generally opaque to the infrared radiation. The working distance, pixel resolution, and fps of the IR camera were 22 cm, 15.3 μm per pixel and 50, respectively. The emissivity of water and glass were taken as 0.97 and 0.95, respectively, for the estimation of the temperature field by IR camera. In an earlier work of our lab group using same infrared camera, Patil et al. [20] have calibrated the infrared (IR) camera (same as used in the present experiments) through comparing the measured temperature from IR camera ($T_{IRcamera}$) with calibrated K-type Chromel-Alumel thermocouples measurements (T_{actual}) for the temperature range from 25 to 95°C. T_{actual} was measured using a multimeter. Figure 3.3 shows the infrared camera calibration equations and graph for water ($\varepsilon = 0.97$), glass ($\varepsilon = 0.95$) and wet-oxidized silicon surfaces ($\varepsilon = 0.78$). The uncertainty in the temperature measured through the infrared camera is around ±0.6°C.

Three cases of the temperature gradient (dT/dX) prescribed on the surface were considered. The lower temperature (T_L) was maintained at 25°C, and the larger temperature (T_H) was maintained at either 60, 50, or 40°C to obtain dT/dX = 4.2, 2.8, or 1.7°C/mm, respectively. Measured isotherms on the surface are shown for these three cases in Figure 3.4 (a-c). The temperature profiles along X at $Y = 3$ mm are plotted in Figure 3.4 (d), along with their linear fits ($R^2 \sim 0.97$). The temperature field obtained from the IR camera was interpolated along X at $Y = 3$ mm using Tecplot®. This software uses bilinear interpolation to get the data along a line. The temperature data points were linearly fitted based on the least square based method using Microsoft Excel software. The R-squared value of the fitted regression line was 0.97, which determines the goodness of the fit. Then the slopes of the linear fits were obtained as 4.2, 2.7 and 1.7, which were taken as the temperature gradient value. The droplet was placed approximately at (X, Y) = (3 mm, 3 mm) and the

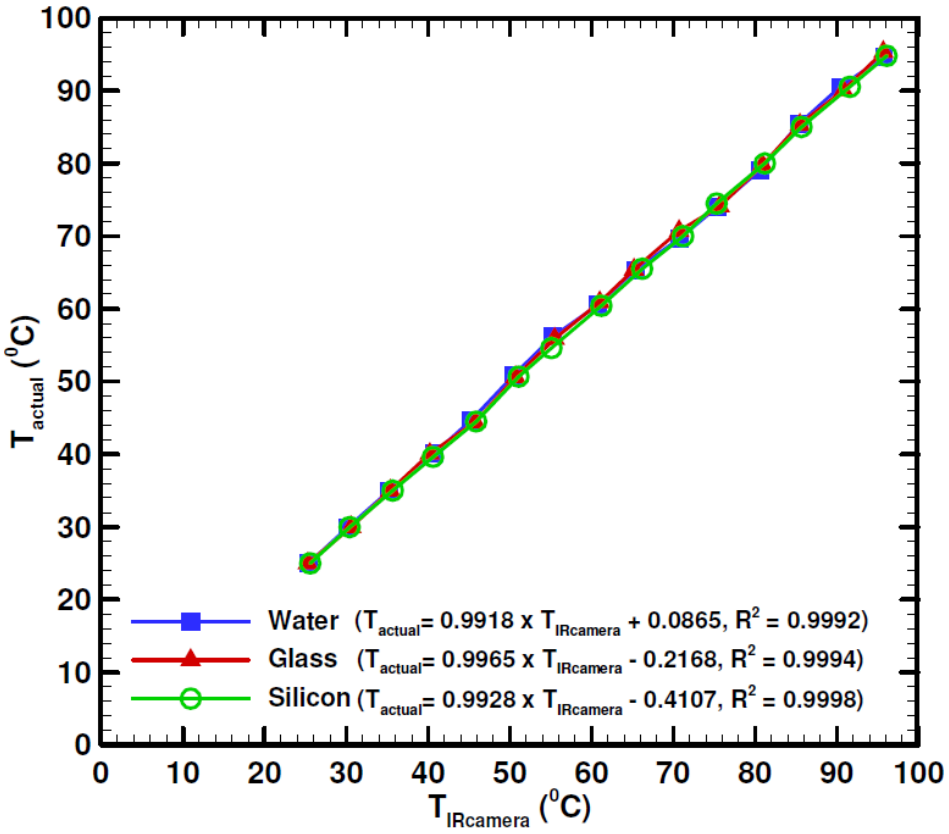

Figure 3.3: Infrared camera calibration graph for water, glass and silicon surface temperatures measurements. Reprinted (adapted) with permission from (Patil et al. [20]). Copyright (2016) American Chemical Society.

dT/dX	1.7°C/mm		2.8°C/mm		4.2°C/mm	
d	θ_i	θ_{rec}	θ_i	θ_{rec}	θ_i	θ_{rec}
0.1 μm	24°	10°	22°	10°	19°	11°
1.1 μm	21°	9°	23°	8°	26°	8°
3.0 μm	38°	7°	41°	7°	42°	5°

Table 3.1: Measured initial static (θ_i) and receding (θ_{rec}) contact angles (in degrees) for different cases of particles diameter (d) and temperature gradient (dT/dX). The particles concentration is fixed at $c = 0.1$ %v/v. The uncertainty in these measurements is around ±2-3°.

approximate temperature at this location before the droplet deposition was around 36, 45, and 51°C for $dT/dX = 4.2$, 2.8, or 1.7°C/mm, respectively. The substrate was also uniformly heated at $T_s = 60$°C using a digital controlled hot plate (15956-32, Cole-Parmer Inc, India), to act as a control.

3.4.4 Side-visualization and optical microscopy

During the experiments, the side view of the sessile droplet was visualized again using a camera (IDT Inc., MotionPro, Y-3 classic) and long-distance working objective (Qioptiq Inc.), with a white LED lamp acting as a backlight source, as shown in Figure 3.1 and Figure 3.2. The working distance and magnification of the camera corresponded to 9.5 cm, and 14 μm per pixel, respectively, and the videos were recorded at 10 frames per second (fps). Dried patterns were visualized from the top by an optical microscope (Olympus BX53F, with a magnification of 4X to 40X) for the zoomed-in view.

The initial static and the receding contact angles for different cases of dT/dX and particle diameter (d) were measured from the images of the side view, assuming droplet shape as a spherical cap and are listed in Table 3.1. The spherical cap assumption is justified since the wetted radius is smaller than the capillary length of water and the imposed temperature gradient does not deform the liquid-gas interface, as confirmed from the side visualization of the evaporating droplet. While the measured angles do not show significant variation with dT/dX, there is a slight increase in the angles as the particle size (d) increases. This data is consistent with our previous work in Chapter 2 in which a weak dependence of the static contact angle on the particle size was reported for a droplet of aqueous colloidal suspension on a non-heated glass. All experiments were performed three times to ensure repeatability. The ambient temperature and the relative humidity were 25 ± 2°C and 35 ± 5%, respectively.

In order to verify the evaporation characteristics on a non-uniformly heated substarte, the evaporation behaviour of a 1.1 ± 0.3 μL pure water droplet on a glass substrate with $dT/dX = 4.2$°C/mm is investigated. The droplet was placed roughly at X = 3 mm (Figure

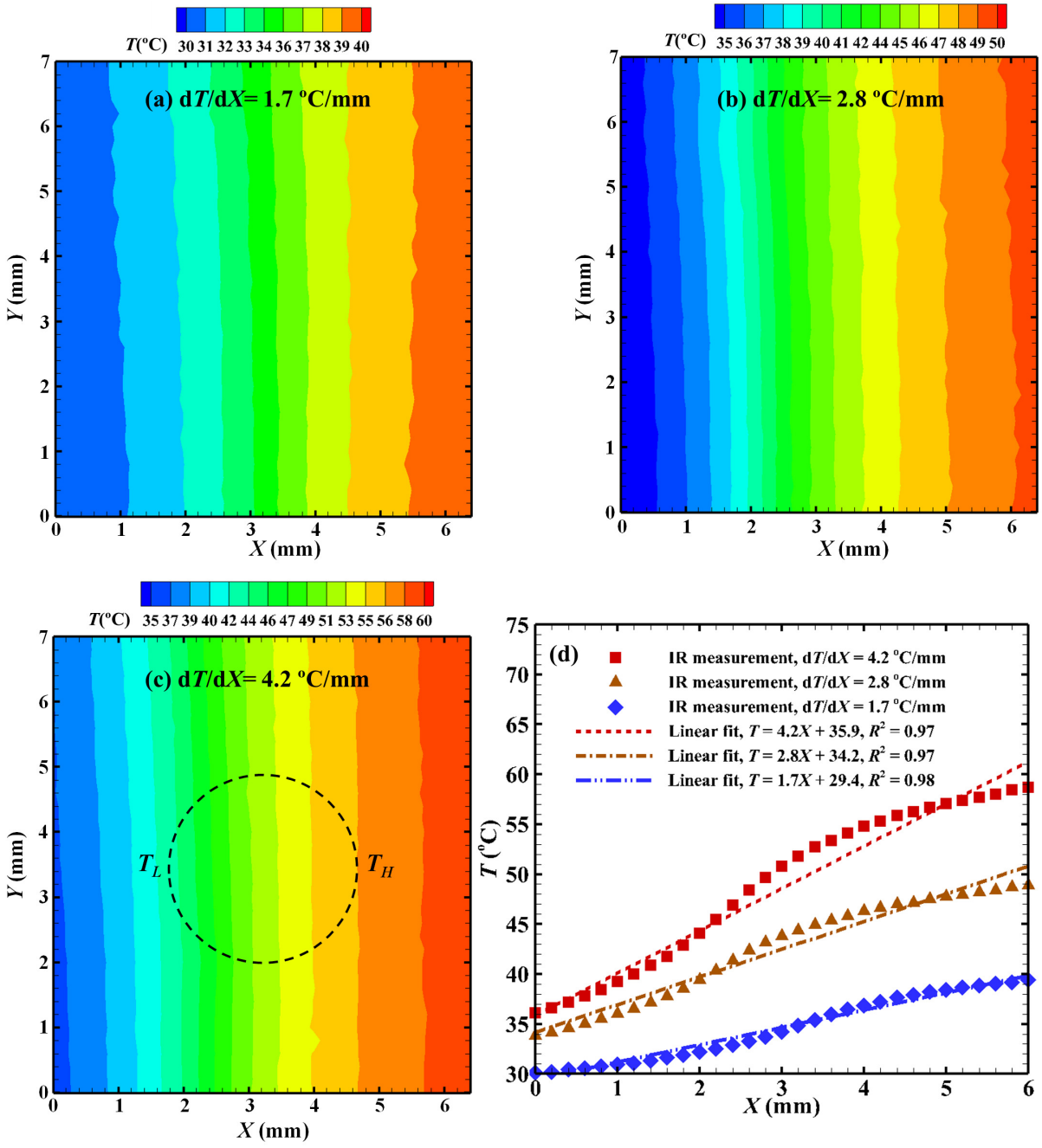

Figure 3.4: Isotherms plotted for different cases of imposed temperature gradient (a) $\mathrm{d}T/\mathrm{d}X$ = 1.7°C/mm (b) $\mathrm{d}T/\mathrm{d}X = 2.8$°C/mm (c) $\mathrm{d}T/\mathrm{d}X = 4.2$°C/mm. The dotted circle shows approximate deposition location of the droplet. (d) The temperature along X at $Y = 3$ mm is plotted for the three cases. Linear fits to the measured data are shown with R^2 values.

3.4 (d)). The initial values of the wetted diameter, droplet height, and contact angle were 2.83 mm, 0.4 mm, and 31.6°, respectively, as measured from the side view image shown in Figure 3.5(a). From the IR camera thermography images, the high temperature and low temperature at the ends of the droplet were measured as 57°C, and 44°C, respectively, hence the actual temperature difference between the two ends of the droplet was 13°C. Also, the evaporation of the pure water droplet was studied on a glass substrate at constant temperature cases of 57 and 44°C, and the average temperature of 57 and 44°C that is 50°C. The time-varying droplet volume is plotted in Figure 3.5 (b) for each of these cases. The largest evaporation time is 140 s ($T_s = 44$°C), and the shortest is 60 s ($T_s = 57$°C). Most interestingly, an evaporation time of 90 s results from both the temperature gradient case ($\mathrm{d}T/\mathrm{d}X = 4.2$°C/mm) and the constant temperature case at the average temperature across this gradient (50°C).

3.5 A Mechanistic model for the depinning of the contact line

A first-order model, developed in previous studies [21, 127, 132, 133], is utilized to predict depinning or pinning of the contact line against the present measurements. The model accounts for the several forces acting on the particles stacked near the contact line, shown in a schematic in Figure 3.6. The surface tension force (F_s) acting on the particle near to contact line and touching the liquid-gas interface pulls the particle away from the contact line while drag force (F_d) push them towards the contact line. The normal forces (F_a) acting on the particles are van der Waals and electrostatic forces. Here, gravity is ignored for neutrally buoyant polystyrene particles. The expressions of these forces are given in the following subsections.

Surface tension force

The surface tension force acting on the outermost particle at the contact line is given by the following relation [21, 134],

$$F_s = \pi d \gamma_{LG} cos\phi \tag{3.3}$$

where d, γ_{LG}, and ϕ are the particles diameter, liquid-gas surface tension, and angle of the liquid layer covering the outermost particle at the contact line, respectively.

van der Waals force

The van der Waals force between the particles and substrate in the fluid medium is given

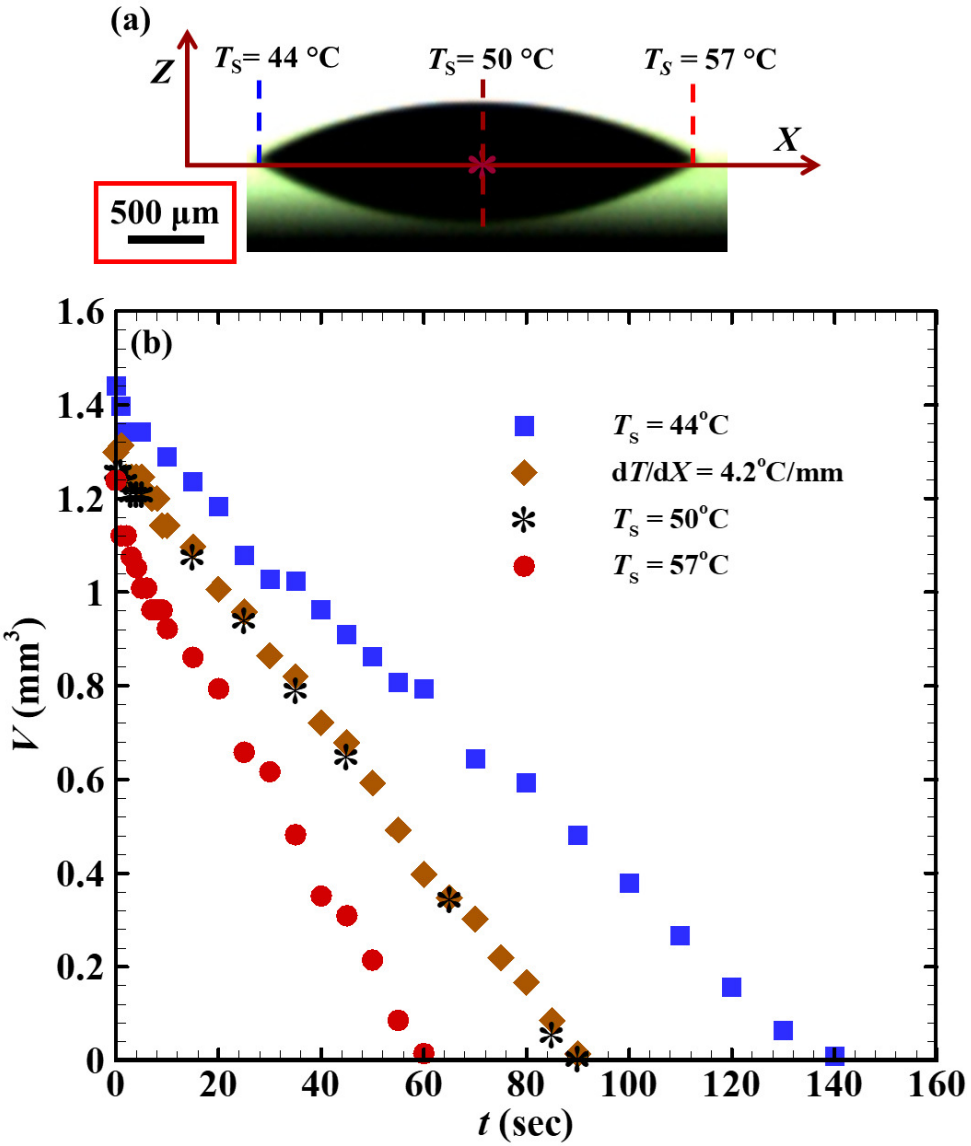

Figure 3.5: Side view image of an evaporating pure water droplet of 1.1 ± 0.2 μL at $t = 0$ sec. (b) Change in the volume of the 1.1 μL pure water droplet with evaporation on the substrate at different temperature conditions.

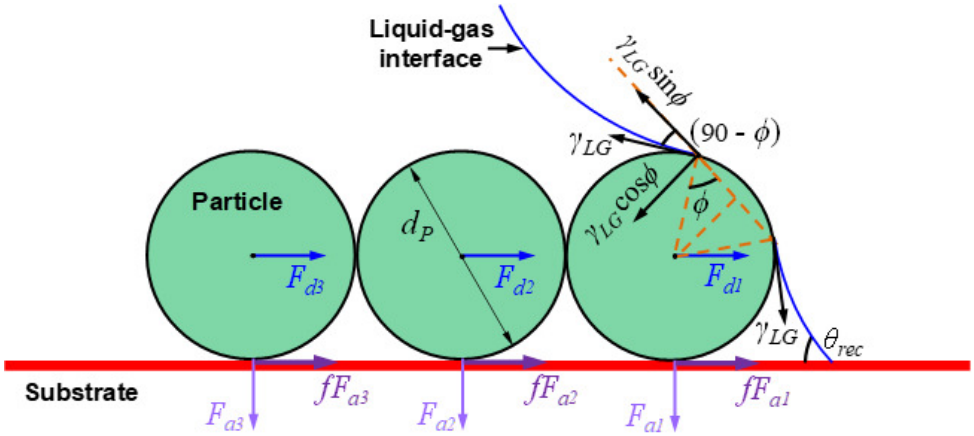

Figure 3.6: Schematic of particles stacked near the contact line and different forces acting on them. Surface tension force pulls the outermost particle inward while drag force pushes all particles outward towards the contact line. Adhesion force (van der Waals force) resist the motion of the particles. Adapted from Ref. [21], Copyright, 2017, Springer Nature and reproduced from Ref. [7], Copyright, 2018, American Chemical Society.

by the following relation [127, 135],

$$F_{wps} = \frac{2A_{123}(d/2)^3}{3z^2(z+d)^2} \tag{3.4}$$

where A_{123} and z are the Hamaker constant for the polystyrene particles and glass in water, and particle-substrate minimum separation distance, respectively.

Electrostatic force

The electrostatic force between the particles and substrate in the fluid medium is given by the following relation [127, 133],

$$F_{eps} = -\pi d\varepsilon k \frac{{\phi_1}^2 + {\phi_2}^2 - 2\phi_1\phi_2 exp(kz)}{exp(2kz) - 1} \tag{3.5}$$

where ε, k, ϕ_1, and ϕ_2 are permittivity of water, reciprocal of the Debye length, the surface potential of polystyrene, and surface potential of glass, respectively.

Drag force

The drag force experienced by the particles in an evaporating droplet is given by the following relation [8, 132],

$$F_d = 3\pi d\mu v_{rad} \tag{3.6}$$

where μ and v_{rad} are dynamic viscosity of water and velocity of water in an evaporating droplet, respectively.

The total adhesion force (F_{a1}) on the outer most particle of the contact line is $F_{a1} = F_{wps1} + F_{eps1} + F_s cos\theta_{rec}$, and the total adhesion force (F_{a2}) on the penultimate particle

Symbols	Physical parameter	Value	Unit
A_{123}	Hamaker constant for the polystyrene particles and glass in water	3x10^{-20} [127, 133]	J
d	Polystyrene particles diameter	0.1, 1.1, 3.0	μm
z	Particle-substrate minimum separation distance	0.4x10^{-9} [127, 133]	m
ε	Permittivity of water	7x10^{-10}	Fm^{-1}
k	Reciprocal of the Debye length	(430x10^{-9})$^{-1}$[127, 133]	m^{-1}
ϕ_1	Surface potential of polystyrene	15 [127, 133]	mV
ϕ_2	Surface potential of glass	-40 [127, 133]	mV
μ	Dynamic viscosity of water	0.001	Pa-s
γ_{LG}	Surface tension of water	0.072	Nm^{-1}
v_{rad}	Velocity of water in a evaporating droplet	7.33x10^{-7} [20]	m/s
$\pi-2\phi$	Angle of liquid layer covering the outermost particle at the contact line	89	degrees
n	Number of particles stacked at the contact line (based on optical microscopy measurements in the present work)	10	
f	Friction coefficient between the particles and the substrate in liquid medium	0.1 [7]	

Table 3.2: Values of the parameters used in calculations of forces acting on the particles.

to the contact line is $F_{a2} = F_{wps2} + F_{eps2}$. Therefore the total adhesion force (F_a) is given $F_s cos\theta_{rec} + nF_a$, where n is the number of particles stacked at the contact line. v_{rad} is the evaporative driven flow velocity, which scales as J_{max}/ρ_L [8], where J_{max} is the maximum evaporative flux near the contact line and ρ_L is droplet density. All the parameters are defined in Table 3.2.

The dimensionless net force (ΔF^*) acting on the outermost particle along the inward horizontal direction is given by [7, 21, 127, 132, 133],

$$\Delta F^* = \frac{1}{\gamma_{LG} d}[F_s sin\theta_{rec} - [f(F_s cos\theta_{rec} + nF_a) + nF_d]] \tag{3.7}$$

The sign on the net force determines if the contact line pins ($\Delta F^* < 0$) or depins ($\Delta F^* > 0$). The values of the parameters required for the calculation of the forces are taken from previous studies [7, 127] and are provided in the Table 3.2. The measured values of the receding angles (θ_{rec}) for different cases of the temperature gradient (dT/dX) and particles size (d) are listed in Table 3.2.

3.6 Results and discussion

Results are presented for the evaporation of 1.0 ± 0.3 μL water droplet containing polystyrene particles on a hydrophilic glass substrate for different cases of particle diameter ($d = 0.1$, 1.1, and 3.0 μm) and concentration ($c = 0.05$, 0.1, 0.5 %v/v). The hydrophilic glass substrate is maintained at a uniform temperature ($T_s = 25$ and 60°C) and a non-uniform temperature with three cases of the temperature gradient, ($\mathrm{d}T/\mathrm{d}X = 1.7$, 2.8, and 4.2°C/mm).

3.6.1 Non-heated or heated substrate at a uniform temperature

3.6.1.1 Effect of particles size and substrate heating

Optical microscopy images of deposition patterns on the substrate at T_s =25, and 60°C, with three cases of particle diameter, $d = 0.1$, 1.1, and 3.0 μm are shown in Figure 3.7. The particle concentration was fixed at, $c = 0.1$ %v/v and the patterns for each case are presented for two runs. All patterns exhibit a ring-like deposit and coupled transport phenomena during the formation of the ring is well-documented in the literature [37, 38]. The corresponding ring profiles measured using optical profilometer for the first run at $T_s = 25$°C is shown in Figure 3.8 (a). The ring profiles plotted on both the left and right sides of the ring are almost similar, and the profiles resemble a partial torus-like shape. The measured cross-section of the ring is consistent with our previous study [136]. Zoomed-in views of the two sides plotted in Figure 3.7 (a) are qualitatively consistent with the measured profiles. The ring dimensions (width and height) are almost on the same order on the two sides. Cracks in the ring at $d = 0.1$ μm (Figure 3.7 (a)) were recorded but not in case of $d = 1.1$, and 3.0 μm. As discussed in Refs. [6, 70, 93, 98] the cracks are formed at the final drying stage of the droplet when the receding liquid tries to shrink the ring whereas the pinned particles obstruct such shrinkage. This results in stress inside the deposit and consequently induces cracks, explained in details in our previous work [136]. A bilayer of particles form in cases of $d = 1.1$, and 3.0 μm since the ring height is almost double the particle diameter.

At $T_s = 60$°C, the deposit patterns and the measured profiles are plotted in Figure 3.7 (b) and Figure 3.8 (b), respectively. The profiles show that the ring gets thinner in this case, and the deposit patterns show the presence of an inner deposit in this case. The ring width decreases by 86, 17, and 25 %, for $d = 0.1$, 1.1, and 3.0 μm, respectively. At $d = 0.1$ μm, an asymmetric inner deposit forms while at $d = 1.1$, and 3.0 μm, the inner deposit is symmetric with respect to the ring.

3.6.1.2 Mechanism of formation of the deposits

At T_s =25°C, the evaporation-induced flow inside the droplet is radially outward, owing to the largest evaporation flux near the contact line, shown schematically in Figure 3.9(a).

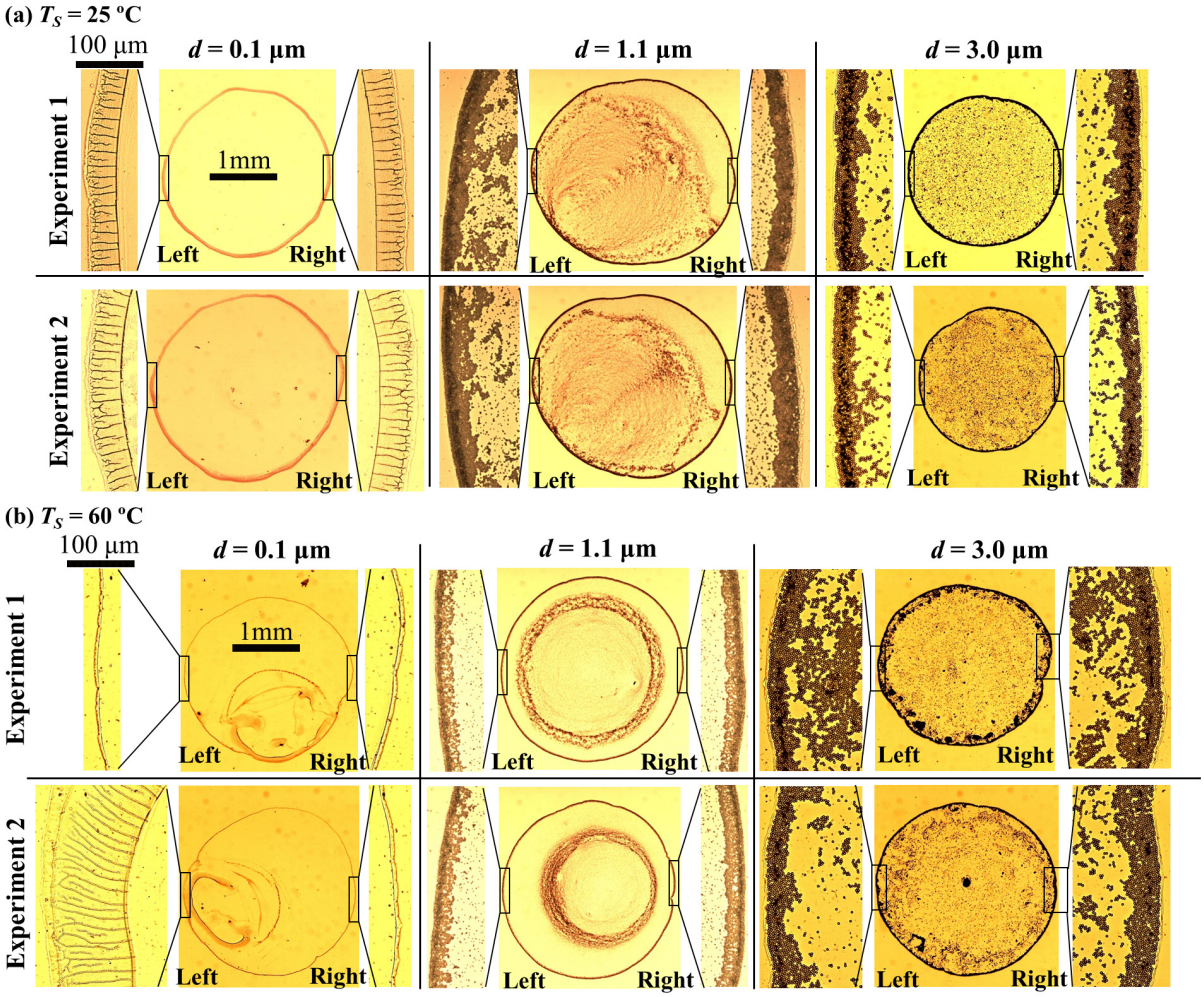

Figure 3.7: Deposit patterns obtained after evaporation of 1 μL droplet containing polystyrene particles of different particles sizes (d), keeping particles concentration constant as, $c = 0.1$ %v/v on a substrate with an imposed constant temperature of (a) $T_s = 25$°C (b) $T_s = 60$°C. Zoom-in view of the rings on the left and right side are also shown for each case.

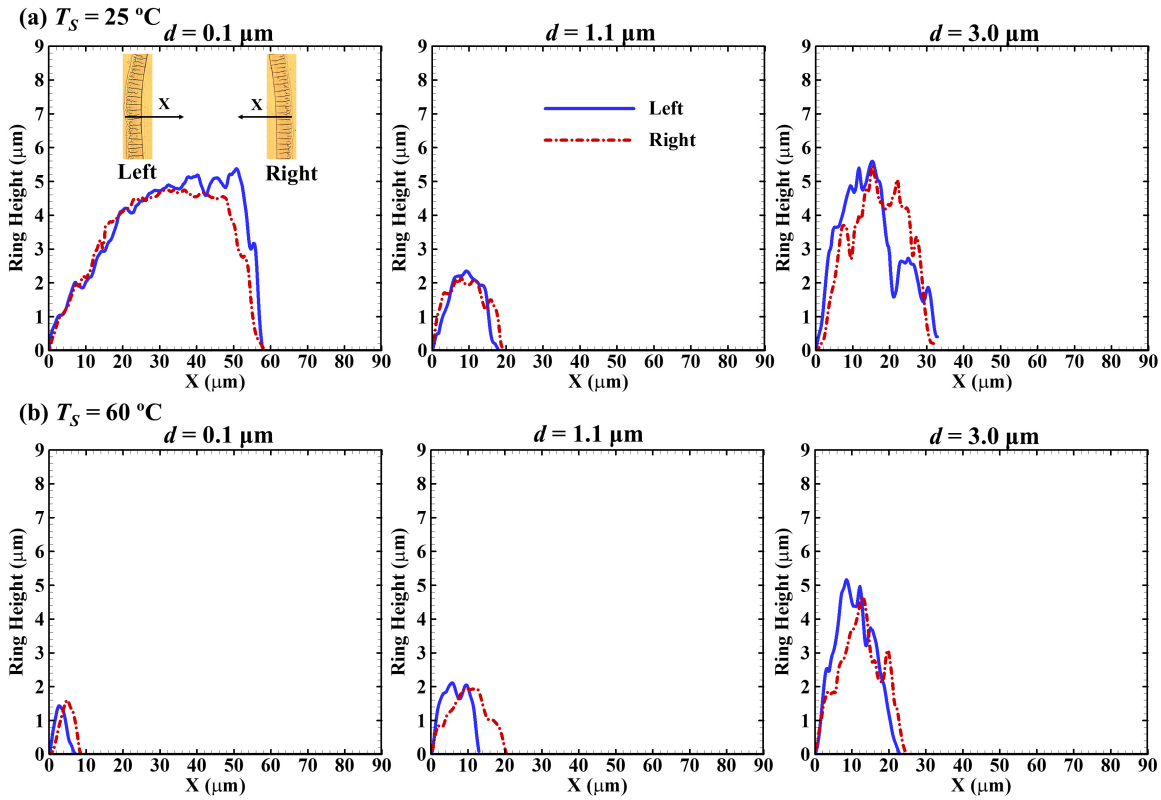

Figure 3.8: Ring profiles measured using an optical profilometer on both the left and right side and plotted for different cases of substrate with an imposed constant temperature of (a) $T_s = 25°C$ (b) $T_s = 60°C$ for different particles sizes ($d = 0.1, 1.1, 3.0\,\mu$m) at concentration, $c = 0.1$ %v/v. X represents the radial position in the deposit (shown as the inset) and $X = 0$ is the ring periphery on both the left and right side.

The arrows normal to the interface represent the flux. Thus, the advection of the particles leads to the formation of the ring, as explained earlier by Deegan et al. [37]. In case of the substrate heating (T_s =60°C), despite a heat loss by the latent heat of evaporation near the contact line, thermal energy is readily available from the substrate in this region, as discussed by Ristenpart et al. [106]. Since a thermal conduction resistance exists across the droplet thickness, the temperature on the liquid-gas interface near droplet apex is lesser than near the contact line. Due to these two factors, a thermal gradient appears across the liquid-gas interface. Consequently, it results in a surface tension gradient and a thermal Marangoni flow exists at the liquid-gas interface whose direction is from the contact line to the droplet apex [9, 20, 49]. Along with radially outward flow (bulk flow), it leads to an axisymmetric Marangoni recirculation inside the droplet that advects particles towards the inner region, as shown in Figure 3.9(b). The arrows on the liquid-gas interface in Figure 3.9(b) represent the variation of evaporation mass flux on a heated substrate, reported in Ref. [97]. The outward radial flow and the inward Marangoni flow, which are opposite in direction to each other, create a stagnation region near the contact line, shown schematically in Figure 3.9(b). The existence of such a stagnation region was reported in Refs. [9, 20, 49]. Due to the curvature of the liquid-gas interface and the outward radial flow, some particles get deposited in the stagnation region, forming the outer ring [9, 20], while most of the particles are advected inward, due to the Marangoni recirculation. Therefore, the deposit, in the heated substrate case, is a thinner ring along with an inner deposit. The thinning of the ring occurs due to advection of particles towards the center of the droplet by the inward Marangoni flow. At $d = 0.1$ μm, the non-axisymmetric inner deposit is formed due to early depinning of the contact line with a stick-slip motion from random direction and the particles are dumped asymmetrically in the wetted area during the final dry out stage of evaporation. While at $d = 1.1$, and 3.0 μm, the contact line is pinned throughout the evaporation, and the inward advection of the particles due to the Marangoni recirculation forms a ring-like axisymmetric inner deposit.

3.6.2 Heated substrate at a non-uniform temperature

Figure 3.10 (a), (b), and (c) show dried patterns of the deposit obtained by optical microscopy for the particle size of $d = 0.1$, 1.1, and 3.0 μm, respectively, with particles concentration of 0.1%. Two runs are shown for each case, and the columns represent different cases of $\mathrm{d}T/\mathrm{d}X = 1.7$, 2.8, and 4.2°C/mm and the left and right side of each case was at lower (T_L) and higher temperature (T_H), respectively. The zoom-in views of the ring on the T_L and T_H sides are shown for each case in Figure 3.10. The corresponding ring profiles measured using optical profilometer for the first run for $d = 0.1$, 1.1, and 3.0 μm for the different $\mathrm{d}T/\mathrm{d}X$ are plotted in Figure 3.11 (a), (b), and (c), respectively.

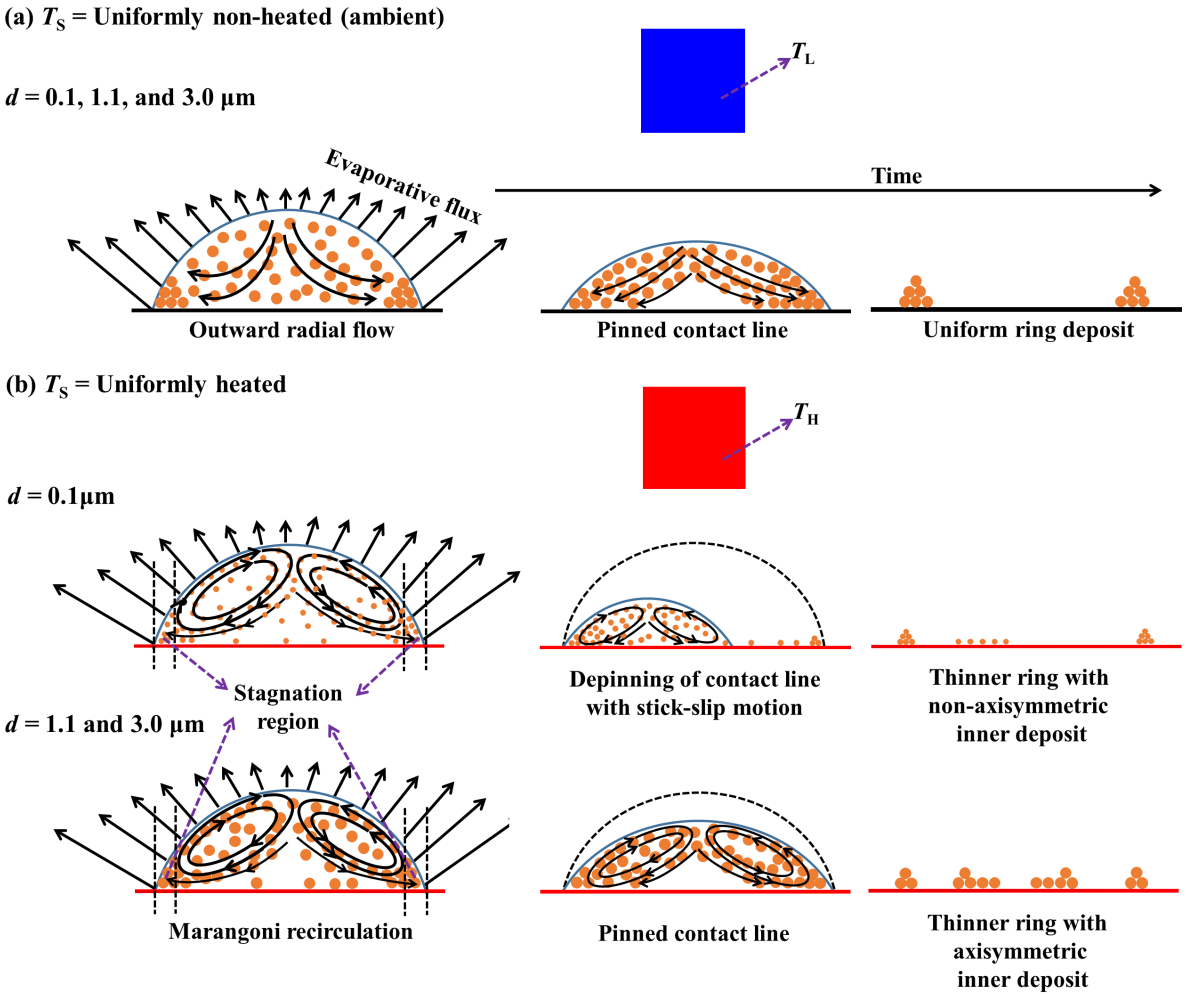

Figure 3.9: Mechanism of the deposit formation for a uniform temperature substrate (a) Non-heated (T_s = 25°C). The arrows on the liquid-gas interface represent non-uniform, axisymmetric evaporation mass flux on the liquid-gas interface. A radial outward bulk flow advects particles to form a ring-like deposit. (b) Uniformly heated substrate (T_s = 60°C). An axisymmetric Marangoni recirculation develops due to themocapillary flow and radial flow in the bulk. In the case of smaller particles, the contact line depins from a random direction and shows the signature of stick-slip motion while for the bigger particles the contact line remains pinned. The depinning occurs if the surface tension force on the particle at the contact line overwhelms the combined friction force between the particles and substrate and hydrodynamic drag force.

For $d = 0.1$ μm, the ring width is wider on the T_L side as compared to the T_H side for all the cases of $\mathrm{d}T/\mathrm{d}X$ as observed qualitatively in Figure 3.10 (a) and quantitatively in Figure 3.11 (a). With an increase in $\mathrm{d}T/\mathrm{d}X$, the ring width on the T_L side increases from 50 μm to 76 μm, whereas the ring width on the T_H side decreases from 44 μm to 8 μm. The ring heights are also larger on the T_L side as compared to the T_H side and increase with the increase in the $\mathrm{d}T/\mathrm{d}X$. Thus, the mass of particles is smaller on T_H side as compared to that on the T_L side. Cracks on the ring were also recorded in this case, as seen earlier in case of the uniformly non-heated or heated substrate.

In contrast, for $d = 1.1$, and 3.0 μm, the ring width is wider on the T_H side as compared to the T_L side for all cases of $\mathrm{d}T/\mathrm{d}X$ as observed qualitatively in Figure 3.10 (b), and (c), and quantitatively in Figure 3.11 (b), and (c), respectively. In general, the ring width shows a slight increase and decrease for T_H and T_L side, respectively, with an increase in $\mathrm{d}T/\mathrm{d}X$. The ring height remains almost same for $d = 1.1$ μm with an increase in $\mathrm{d}T/\mathrm{d}X$ while it increases for 3.0 μm. For $d = 1.1$ μm, the ring widths on the T_L side decreases from 30 μm to 20 μm. For $d = 3.0$ μm, with the increase in the $\mathrm{d}T/\mathrm{d}X$, the ring widths on the T_L side decreases from 50 μm to 40 μm. The ring widths on the T_H side increases from 70 μm at $\mathrm{d}T/\mathrm{d}X = 1.7$°C/mm and goes beyond 90 μm for $\mathrm{d}T/\mathrm{d}X = 2.8$, and 4.2°C/mm. The ring heights on the T_H side for $\mathrm{d}T/\mathrm{d}X = 1.7$, and 2.8°C/mm are around 6 μm and increase to 9 μm with an increase in $\mathrm{d}T/\mathrm{d}X$ to 4.2°C/mm. Overall, with the increase in $\mathrm{d}T/\mathrm{d}X$, the mass of particles in the ring is larger on the T_H side as compared to that on the T_L side. The ring-like axisymmetric inner deposit was also recorded for $d = 1.1$ μm with the intensity of the inner deposit larger towards the T_H side, as observed qualitatively in Figure 3.10 (b).

The effect of particles concentration (c) is also reported at temperature gradient, $\mathrm{d}T/\mathrm{d}X = 4.2$°C/mm and for the cases, $c = 0.05$, and 0.5 %v/v. Figure 3.12 (a) and (b) shows the deposition pattern at $d = 0.1$ and 1.1 μm, respectively. The case for $c = 0.1$ %v/v is already shown in Figure 3.10 (a) at $\mathrm{d}T/\mathrm{d}X = 4.2$°C/mm. For all cases of c, the ring widths are observed to be larger on the T_L side as compared to the T_H side for $d = 0.1$ μm. And for $d = 1.1$ μm, the ring widths are observed to be larger on the T_H side as compared to the T_L side for all cases of c. The ring width on the T_H side increases with increase in the particles concentration. For $d = 0.1$ μm, there are no cracks observed on the T_H side of the ring for $c = 0.05$ %v/v. However, at $c = 0.1$ and 0.5 %v/v, cracks are observed, which are aligned towards the inner side of the ring.

3.6.2.1 Effect of particle size and temperature gradient on contact line motion

Time-varying droplet shapes recorded using side visualization at $\mathrm{d}T/\mathrm{d}X = 4.2$°C/mm for $d = 0.1$, 1.1 and 3.0 μm are plotted in Figure 3.13. In order to quantify the contact line motion in these measurements, the displacements of the contact line from low (T_L) and high (T_H) temperature sides are denoted as X_L and X_H, respectively, and are schematically shown in

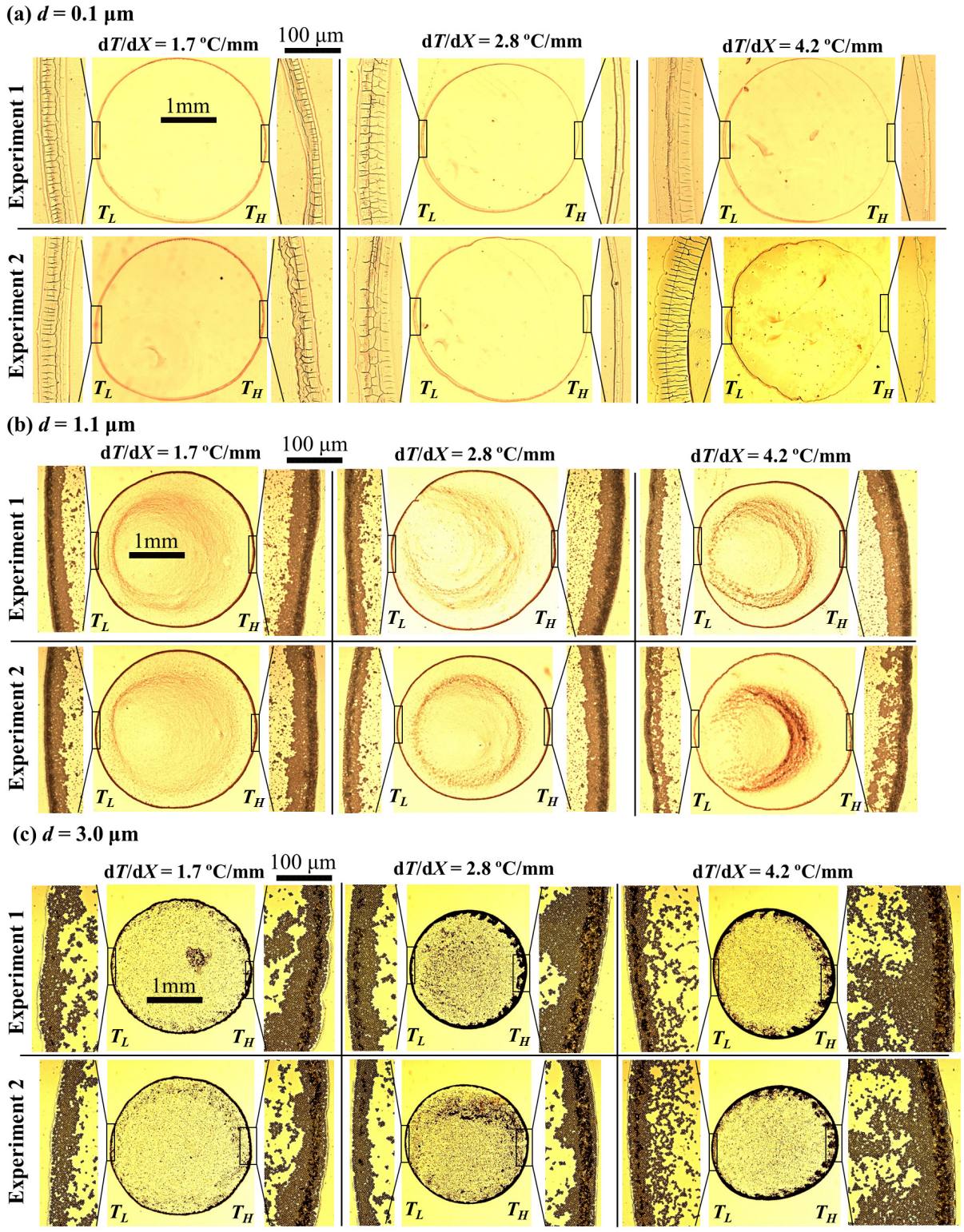

Figure 3.10: Deposit patterns obtained after evaporation of 1 μL droplet containing polystyrene particles of diameter, (a) $d = 0.1$ μm, (b) $d = 1.1$ μm, and (c) $d = 3.0$ μm and concentration, $c = 0.1$ %v/v on a substrate with an imposed temperature gradient, $\mathrm{d}T/\mathrm{d}X = [1.7, 2.8, 4.2]$ °C/mm. Two runs are shown in different rows. T_L and T_H represent the lower and higher temperature side of the substrate, respectively.

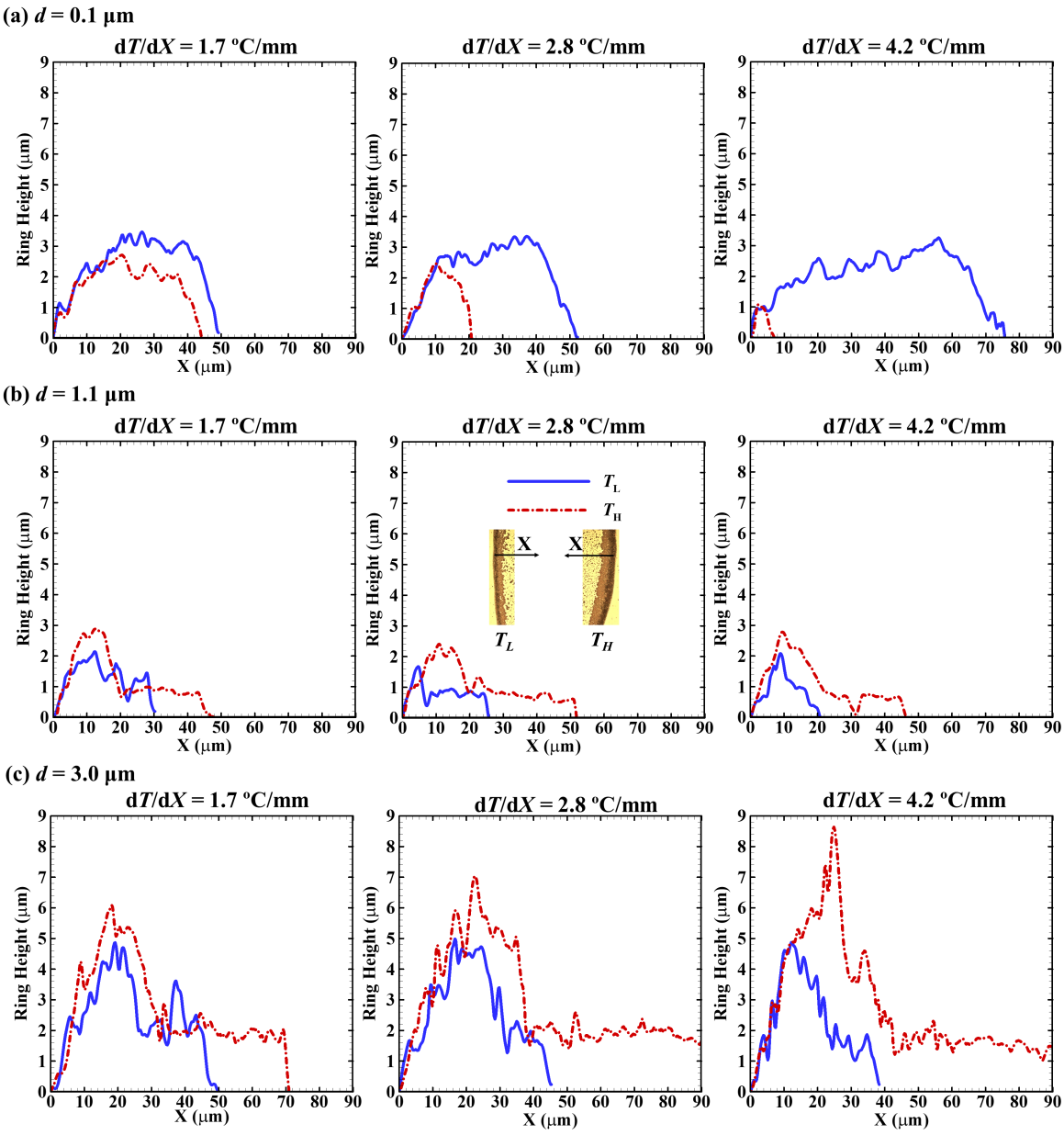

Figure 3.11: Ring profiles measured using an optical profilometer on both the T_L and T_H side and plotted for different cases of particles size (a) $d = 0.1$ μm (b) $d = 1.1$ μm (c) $d = 3.0$ μm) at concentrations, $c = 0.1$ % v/v when substrate is imposed with the temperature gradients ($dT/dX = 1.7$, 2.8, 4.2°C/mm). T_L and T_H represent the lower and higher temperature side of the substrate, respectively. X represents the radial position in the deposit (shown as the inset) and $X = 0$ is the ring periphery on both the T_L and T_H side.

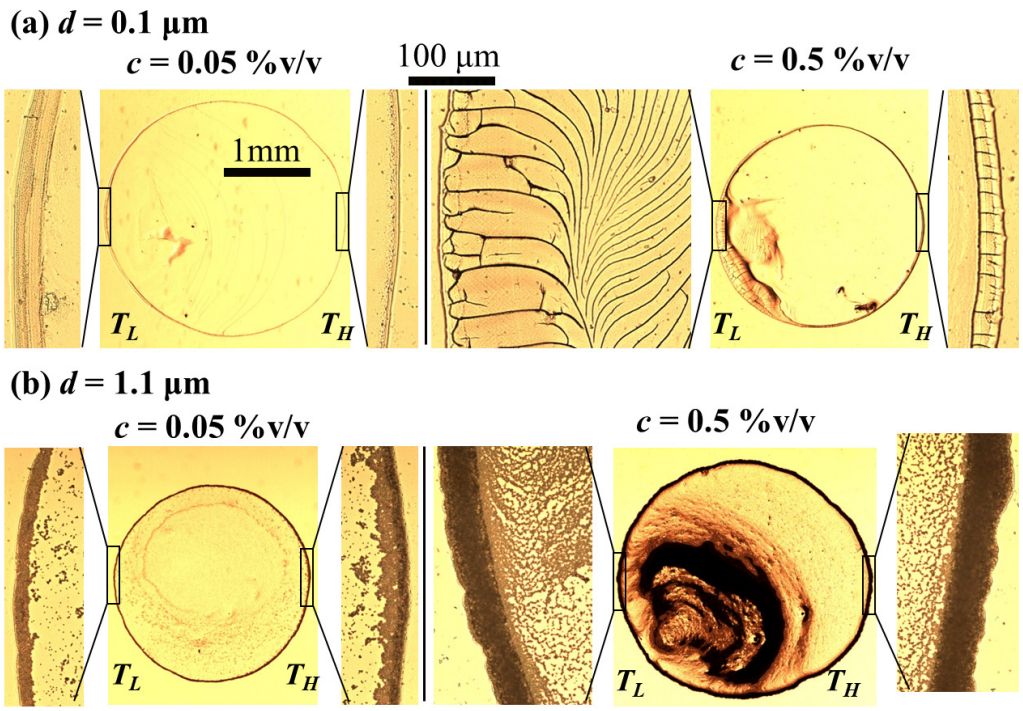

Figure 3.12: Deposit patterns obtained after evaporation of 1 μL droplet containing polystyrene particles of diameter, (a) $d = 0.1$ μm, and (b) $d = 1.1$ μm with concentrations, of $c = 0.05$, and 0.5 %v/v on a substrate with an imposed temperature gradient of $\mathrm{d}T/\mathrm{d}X = 4.2$°C/mm.

Figure 3.14(a).

The contact line displacements for the three cases of particles size are compared in Figure 3.14(b) at $\mathrm{d}T/\mathrm{d}X = 4.2$°C/mm. The contact line on T_H side depins after 25 s for $d = 0.1$ μm, as seen by the graph of X_H (red stars). The contact line at the T_L side is pinned for the maximum time of evaporation, as shown by the graph of X_L (blue stars) in Figure 3.14(b). These trends are qualitatively confirmed in Figure 3.13(a). The jump in the contact line position from the T_H side, corresponding to the depinning, is observed at around 40 s. The contact line exhibits stick-slip motion after this time. By contrast, in the cases of $d = 1.1$ and 3.0 μm, the contact line remains pinned (see graphs of X_L (blue squares and circles) and X_H (red squares and circles)) for the maximum time during the evaporation and depins at around 70 s towards the end of evaporation (observed in Figure 3.13(b), and (c) and Figure 3.14 (b)).

In Figure 3.14(c) for $\mathrm{d}T/\mathrm{d}X = 2.8$°C/mm and Figure 3.14(d) for $\mathrm{d}T/\mathrm{d}X = 1.7$°C/mm, similar trends of the contact line motion are noted for the three particle sizes considered, as discussed above for $\mathrm{d}T/\mathrm{d}X = 4.2$°C/mm. The contact line depins at around 80 s in case of $\mathrm{d}T/\mathrm{d}X = 2.8$°C/mm for $d = 0.1$ μm particles, as plotted in Figure 3.14(c). Whereas, the contact line motion for $\mathrm{d}T/\mathrm{d}X = 1.7$°C/mm for $d = 0.1$ μm is comparatively smoother in Figure 3.14(d). This is attributed to a slower evaporation in 1.7°C/mm case as compared to

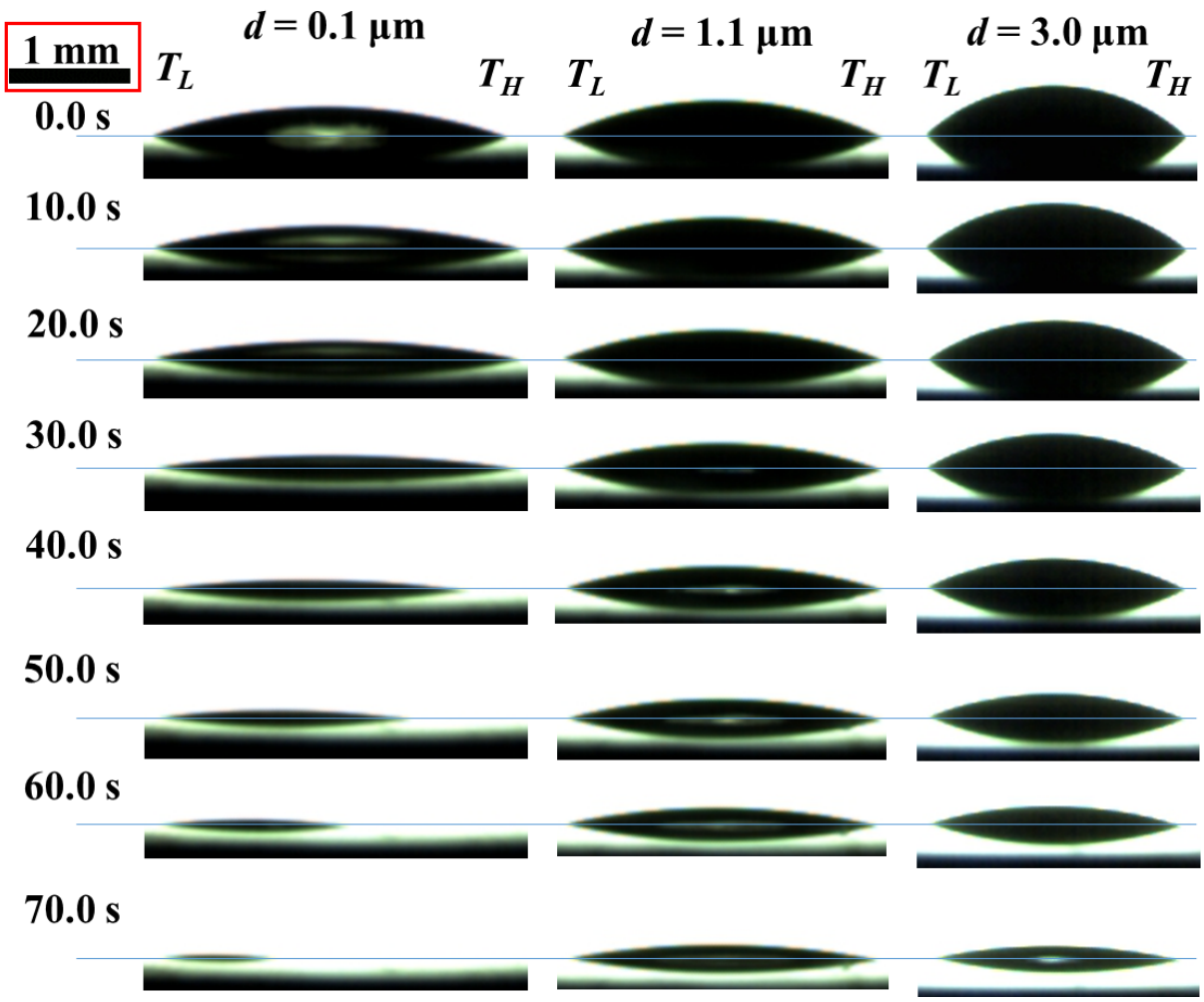

Figure 3.13: Time-sequence of the images obtained by side-visualization during the evaporation of a microliter colloidal suspension on a glass substrate, imposed with a temperature gradient of, $dT/dX = 4.2°C/mm$. A horizontal blue line in all frames represents the solid-gas or liquid-solid interface. T_L and T_H represent the lower and higher temperature side of the substrate, respectively. Three cases of particle sizes are plotted (a) $d = 0.1$ μm, (b) $d = 1.1$ μm, and (c) $d = 3.0$ μm.

2.8°C/mm and 4.2°C/mm cases and the total evaporation time is 28% and 43% shorter, respectively. The contact line remains pinned for most of the evaporation for larger particles in cases of $dT/dX = 2.8°C/mm$ as well as $dT/dX = 1.7°C/mm$, as shown in Figure 3.14(c) and Figure 3.14(d), respectively.

3.6.2.2 Effect of contact line depinning on the deposits

As discussed in the above section, the contact line depins in case of $d = 0.1$ μm particles from the hot side of the substrate (T_H). The deposit patterns obtained for two cases of the temperature gradient, $dT/dX = 4.2°C/mm$ and 2.8°C/mm are shown in Figure 3.15(a) and (b), respectively. The insets in Figure 3.15 show a zoomed-in view of the deposit on T_L side,

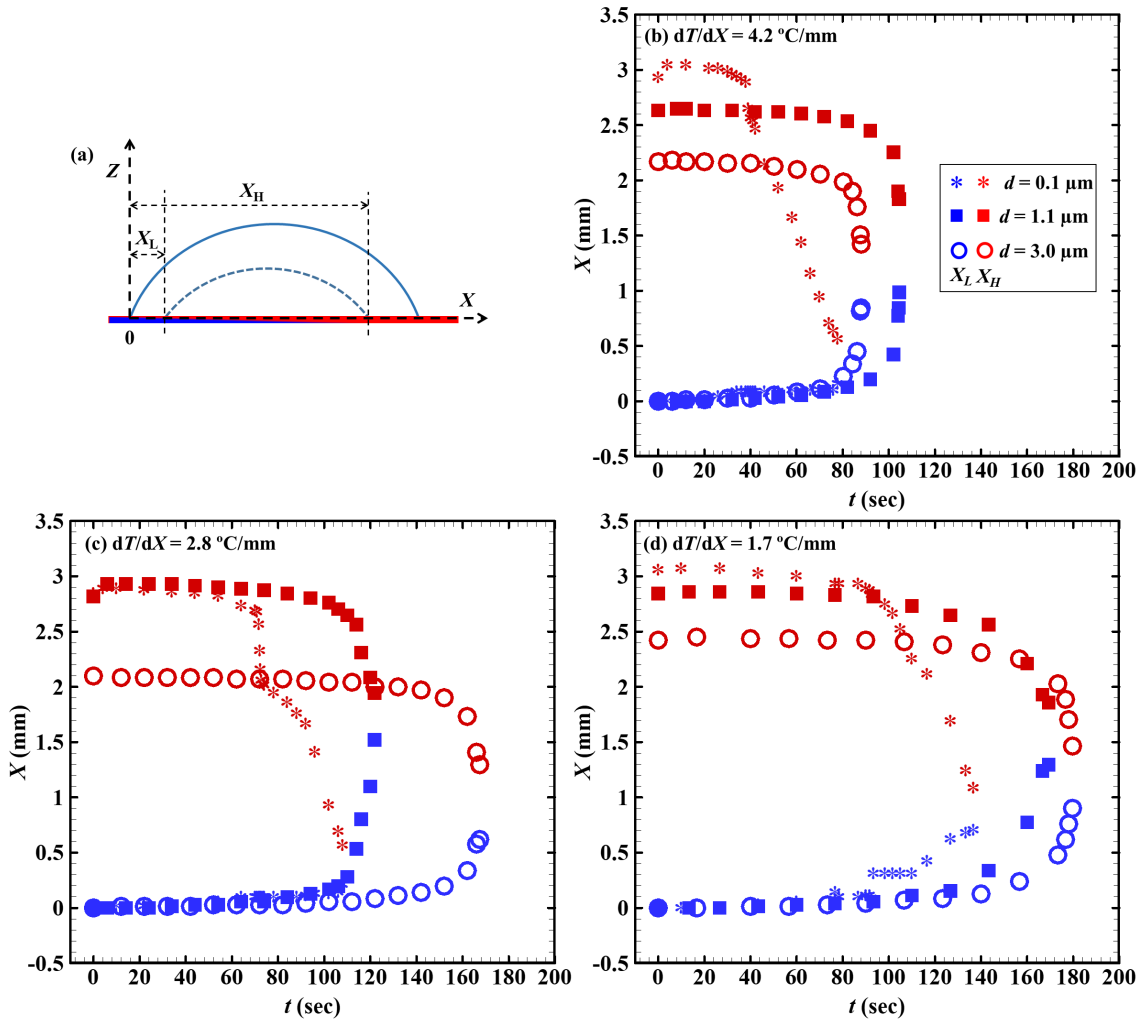

Figure 3.14: Time-variation of the displacements of the contact line from lower (T_L) and higher temperature (T_H) sides of the substrate. X_L (blue symbols) and X_H (red symbols) denote the displacements from T_L and T_H sides, respectively, as schematically shown in (a). Three cases of $\mathrm{d}T/\mathrm{d}X$ are plotted (b) 1.7°C/mm (c) 2.8°C/mm and (d) 4.2°C/mm. In each frame, the displacements, X_L and X_H, are compared for three different particles sizes. For $d = 0.1$ μm, depinning of contact line occurs from T_H (red color) side in all cases of $\mathrm{d}T/\mathrm{d}X$, leading to the stick-slip motion of the contact line. For $d = 1.1$, and 3.0 μm, the contact line is pinned for the maximum duration of the evaporation.

top side and T_H side. As discussed earlier, the deposits in both cases exhibit a smaller ring thickness at T_H side while a larger ring thickness at T_L side. Multiple thin lines of the deposits are observed in the microscopic images of the inner region of the deposit, as shown in the insets of Figure 3.15(a) and (b). These thin lines are the signatures of the stick-slip motion of the contact line, that depins from T_H side for $d = 0.1$ μm particles, as discussed earlier in above section. Some large structures of the deposits in the insets of Figure 3.15 (T_L side) are noted. These are the signatures of the dewetting and drying out of a residual thin liquid film containing particles on the substrate. These particles do not get advected towards the pinned or depinned contact line during the evaporation and remain trapped in the liquid film until at the end of the evaporation.

3.6.2.3 Mechanism of formation of the deposits

The preferential deposition of the particles on either T_H or T_L side with particle size and $\mathrm{d}T/\mathrm{d}X$ is explained as follows. The unidirectional temperature gradient on the substrate creates a temperature gradient on the liquid-gas interface. The temperature near the contact line region of T_H side is larger as compared to the T_L side, as expected. The measured temperature field on the evaporating droplet (as shown in Figure 3.16) verifies the temperature gradient on the liquid-gas interface. The gradient causes thermocapillary Marangoni (interfacial) flow along the interface whose direction is from T_H side to T_L side. The non-uniform evaporation mass flux on the interface induces flow from T_L side to T_H side. This results in twin Marangoni recirculations in two equal halves of the droplet that are separated by a plane aligning along the direction of the imposed temperature gradient. The flow in this plane is schematically shown in Figure 3.17. Such twin recirculations in a pure water droplet on a non-uniformly heated substrate was measured by PIV technique in Ref. [121]. The two characteristics flows (bulk and interfacial) create stagnation regions on both T_H and T_L side contact line where the advected particles get trapped. The existence of a stagnation region on a uniformly heated substrate has been explained earlier. However, the size of the stagnation region on the two sides is not the same on a non-uniform heated substrate. Owing to the larger evaporation flux on T_H side, the flow towards the T_H side would be stronger, creating a larger stagnation region on the T_H side as compared to that on the T_L side. At $d = 0.1$ μm, the depinning of the contact line occurs from the T_H side leading to the stick-slip motion of the contact line towards to T_H side, which advects particles from T_H to T_L side and thereby increases the ring dimensions on the T_L side (Figure 3.17). However, at $d = 1.1$ and 3.0 μm, the contact line is pinned for the maximum time of the evaporation, and a larger number of particles are deposited on the T_H side in the larger stagnation region, as shown in Figure 3.17.

In order to explain the depinning and pinning of the contact line in case of smaller and larger particles, respectively, a mechanistic model (section 3.5) is employed. The dimen-

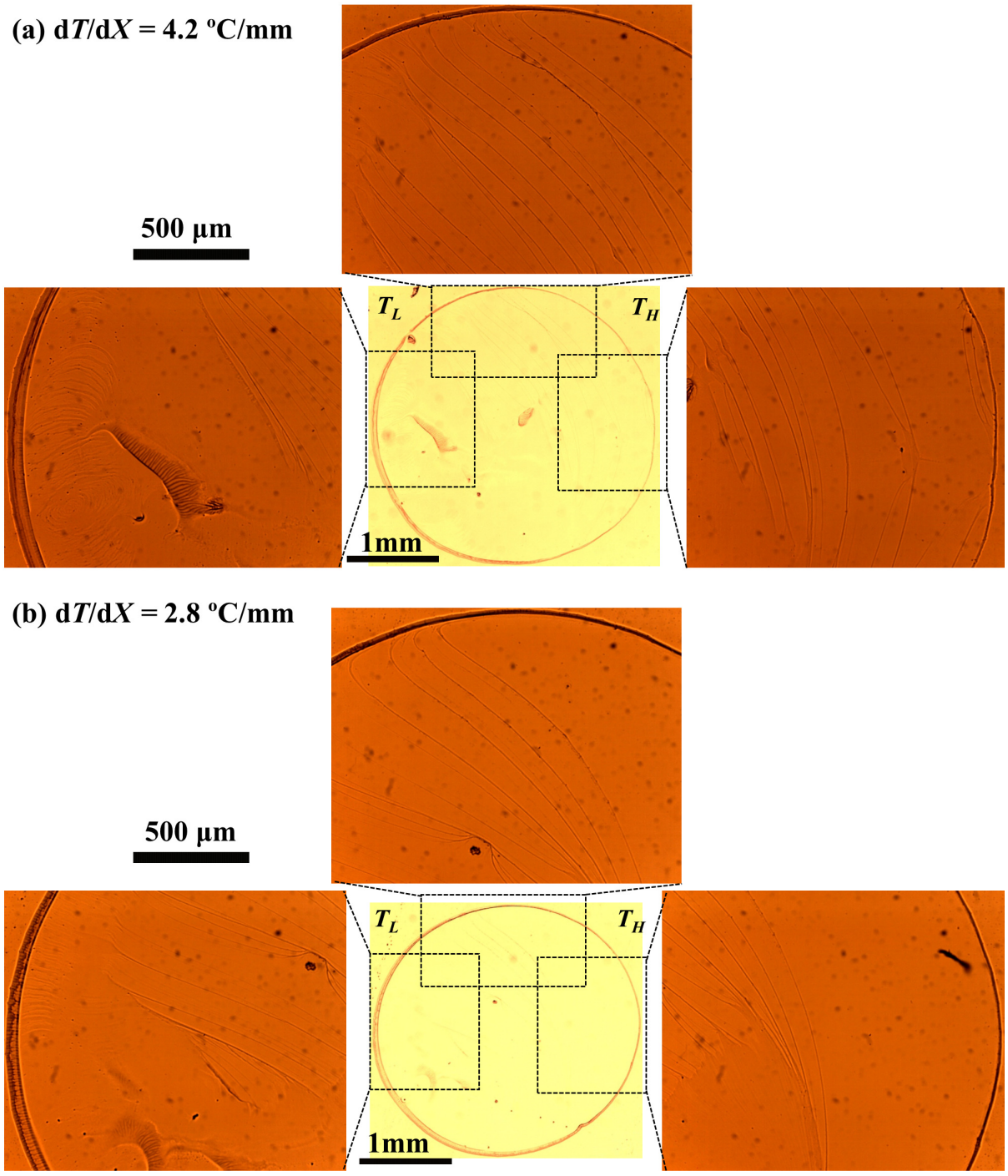

Figure 3.15: Deposit patterns obtained after evaporation of 1 μL droplet containing polystyrene particles of diameter, $d = 0.1$ μm, and concentration, $c = 0.1$ %v/v on a substrate with an imposed temperature gradients of (a) $\mathrm{d}T/\mathrm{d}X = 4.2$°C/mm, and (b) $\mathrm{d}T/\mathrm{d}X = 2.8$°C/mm. The zoom-in figures are shown for three sides (T_L, Top, and T_H side) of the pattern. The patterns in the inset show the signature of the stick-slip motion of the contact line that depins from the hot side (T_H).

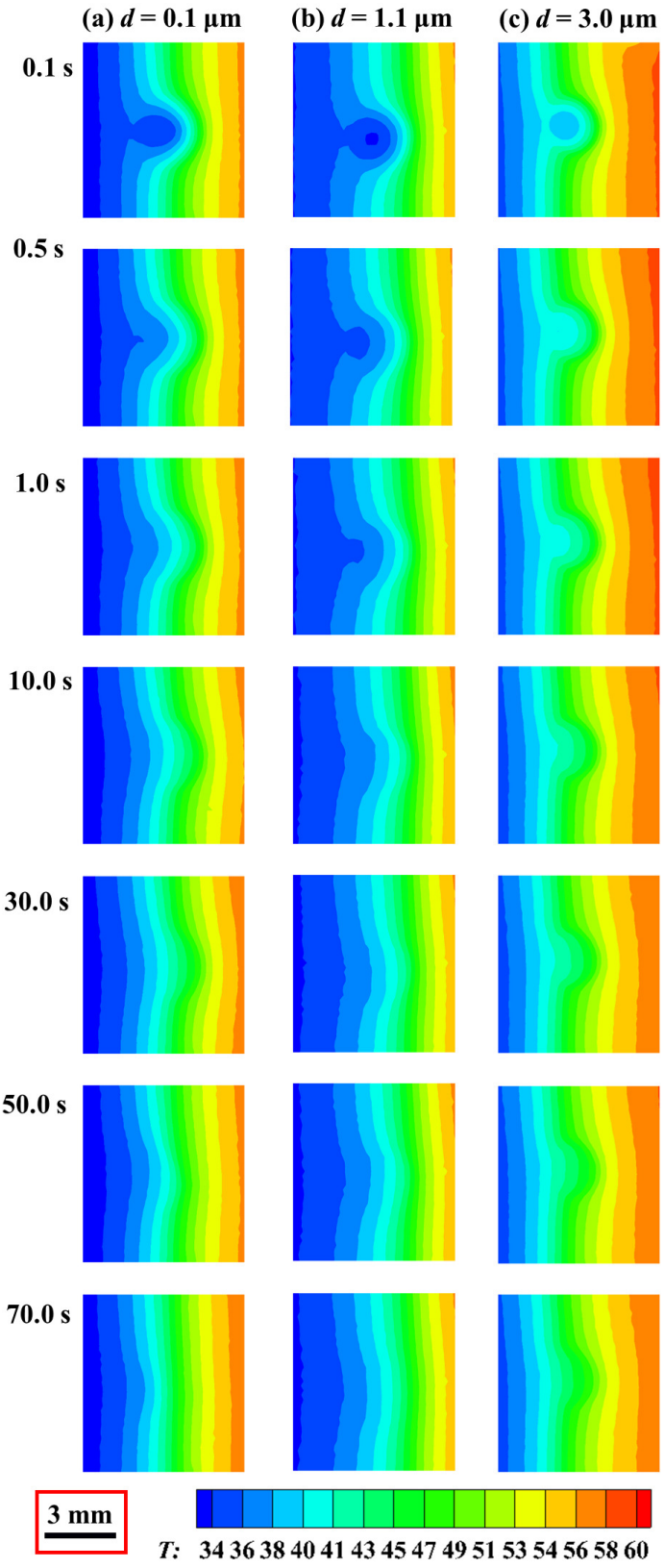

Figure 3.16: Infrared thermography showing instantaneous isotherms on the droplet surface at $\mathrm{d}T/\mathrm{d}X = 4.2$°C/mm on the substrate for different particle sizes at concentration of $c = 0.1$ %v/v

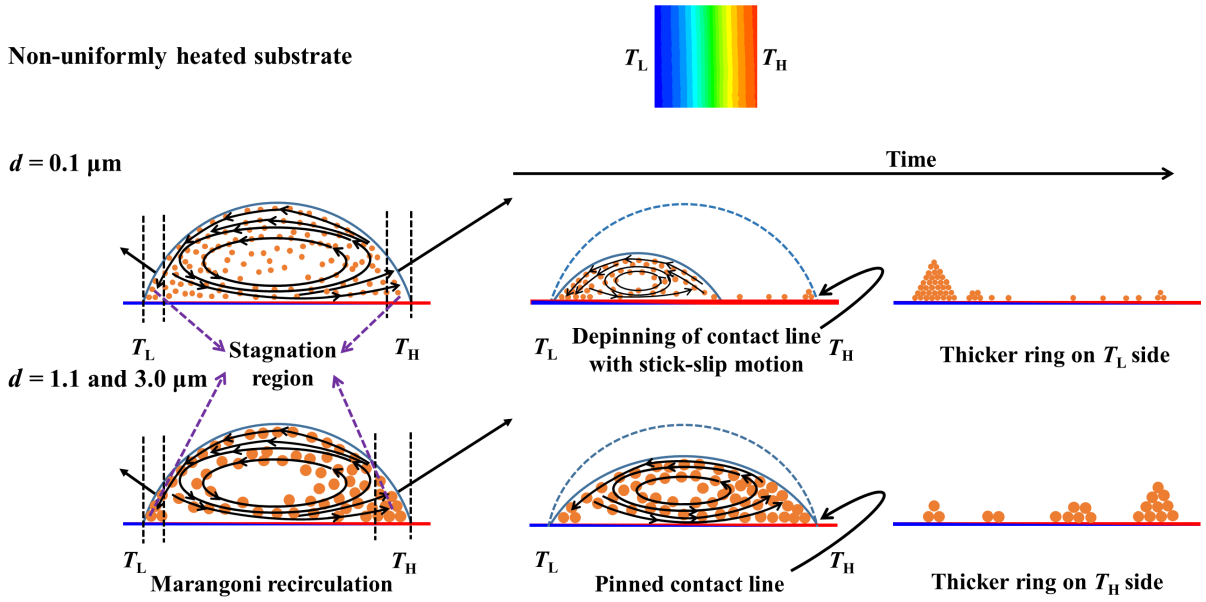

Figure 3.17: Mechanism of the deposit formation for a non-uniformly heated substrate for smaller ($d = 0.1$ μm) and larger particles ($d = 1.1$ and 3.0 μm). T_L and T_H represent the lower and higher temperature side of the substrate, respectively. The arrows on the liquid-gas interface represent non-uniform and asymmetric evaporation mass flux. The flux is larger on the hotter side due to non-uniform heating of the substrate. The unidirectional temperature gradient on the substrate creates a temperature gradient on the liquid-gas interface leading to the thermocapillary Marangoni (interfacial) flow from T_H side to T_L side. The non-uniform flux together with the Marangoni flow on the liquid-gas interface induces bulk liquid flow from T_L side to T_H side that eventually develops as twin asymmetric Marangoni recirculations inside the droplet. In the case of smaller particles, the contact line depins from the hot side and shows the signature of stick-slip motion while for the larger particles the contact line remains pinned. Consequently, the final deposit has a larger ring thickness on the cold side for the smaller particles while a larger ring thickness results on the hot side for the larger particles.

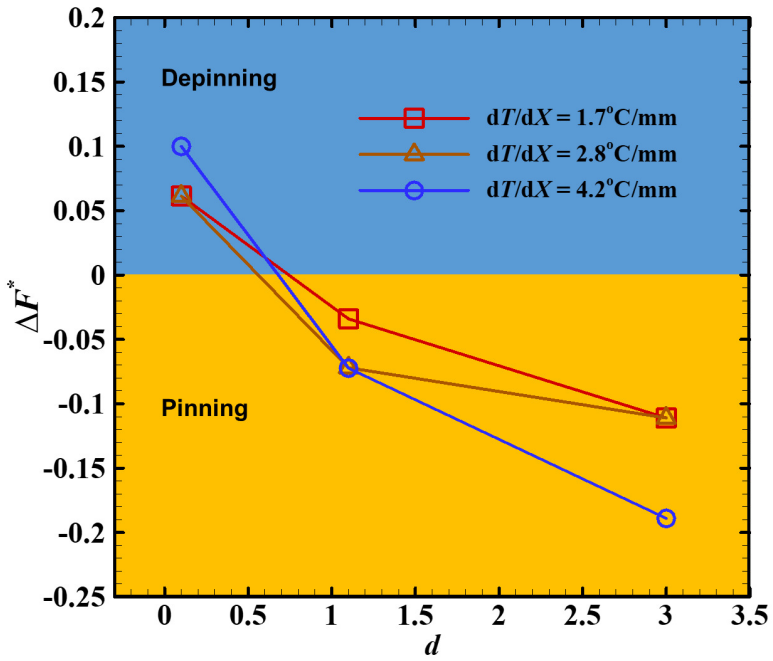

Figure 3.18: Dimensionless net force (ΔF^*) in the inward horizontal direction acting on the particles stacked at the contact line is plotted as a function of particles size (d). Different cases of temperature gradients imposed on the substrate ($\mathrm{d}T/\mathrm{d}X$) are compared. Sign on the net force determines if the contact line pins ($\Delta F^* < 0$) or depins ($\Delta F^* > 0$).

sionless net force (ΔF^*) acting in the inward horizontal direction on the particle nearest to the contact line (eq. 3.7) is plotted as a function of particles size in Figure 3.18 for different cases of $\mathrm{d}T/\mathrm{d}X$ imposed on the substrate. It can be noted that for smaller particles ($d = 0.1$ μm), $\Delta F^* > 0$, i.e., contact line depins for all cases of $\mathrm{d}T/\mathrm{d}X$, which signifies that the surface tension force overcomes the friction and drag forces together. By contrast, for larger particles ($d = 1.1$ and 3.0 μm), $\Delta F^* < 0$, i.e. contact line pins for all cases of $\mathrm{d}T/\mathrm{d}X$, implying that the surface tension forces do not overcome the friction and drag forces. In case of the smaller particles, the depinning occurs on the hot side since a larger intensity of the Marangoni flow advects particles from the hot side to the inner region and the number of particles stacked near the contact line is smaller on the hot side as compared to that on the cold side. Eq. 3.7 shows that for a smaller number of stacked particles (n), $\Delta F^* > 0$ or vice-versa. Overall, the model predictions are consistent with the measurements and this mechanistic model helps to explain the measurements.

3.6.2.4 Regime map

Finally, a regime map is plotted to classify the deposition patterns on a particles size (d) - temperature gradient ($\mathrm{d}T/\mathrm{d}X$) plane in Figure 3.19. At $\mathrm{d}T/\mathrm{d}X = 0$, i.e. if the substrate is

non-heated or heated uniformly, the ring width is uniform. Thus, the first regime is called as $uniform\ ring\ width$. With an increase in the $\mathrm{d}T/\mathrm{d}X$, the ring width gets thicker on the T_L and T_H side for smaller and larger particles, respectively. The dashed lines demarcate the three regimes qualitatively, as shown in Figure 3.19. Our measurements show that for the evaporation on a non-uniformly heated substrate, there exists a critical $\mathrm{d}T/\mathrm{d}X$ at which ring width becomes non-uniform. Beyond this $\mathrm{d}T/\mathrm{d}X$, there also exists a critical particle size below which the contact line depins from the T_H side and stick-slip motion occur, which advects the particles towards the T_L side. Since the ring width is larger on the T_L side, this regime is $thicker\ ring\ on\ lower\ temperature\ side$. For the larger particles, the contact line is pinned and a larger number of particles deposit on the T_H side due to the asymmetric Marangoni recirculation. This results in a larger ring width on T_H side and this regime is $thicker\ ring\ on\ higher\ temperature\ side$.

3.7 Closure

The deposit profile and pattern obtained after the evaporation of a sessile water droplet containing polystyrene colloidal particles on a non-uniformly heated glass substrate is studied. The effect of the temperature gradient and particles size on the deposit pattern and ring dimensions were investigated. The time-varying droplet shapes from the side and the temperature of the liquid-gas interface from the top were recorded using high-speed visualization and infrared thermography, respectively. The dried patterns were visualized under an optical microscope and quantified using an optical profilometer. The following temperature gradients were imposed across the substrate - $\mathrm{d}T/\mathrm{d}X = 1.7$, 2.8, and 4.2°C/mm, and the particles diameter considered were as follows - $d = 0.1$, 1.1, and 3.0 μm.

On the uniformly heated substrate, thinning of the ring with substrate temperature is recorded, which is attributed to an increase in axisymmetric Marangoni recirculation with the substrate temperature. On the non-uniformly heated substrate, the ring dimensions are smaller and larger on higher temperature side (T_H) for a smaller particle ($d = 0.1$ μm), and the larger particles ($d = 1.1$ and 3.0 μm), respectively. The displacement of the contact line on the T_H and T_L side reveals that at $d = 0.1$ μm, the contact line depins early from the T_H side leading to the stick-slip motion of the contact line and twin asymmetric Marangoni recirculations advect more particles towards the T_L side. However, at $d = 1.1$, and 3.0 μm, the contact line remains pinned on both the sides for a maximum duration of evaporation. The pinned contact line and the twin asymmetric Marangoni recirculations aid in trapping the particles in the larger stagnation region on the T_H side contact line. Consequently, the ring width is larger on the T_H side in this case. The variation of the temperature gradient across the substrate shows that the ring width significantly increases or decreases on T_H or T_L side, depending on the particle size. This can be attributed to a stronger Marangoni

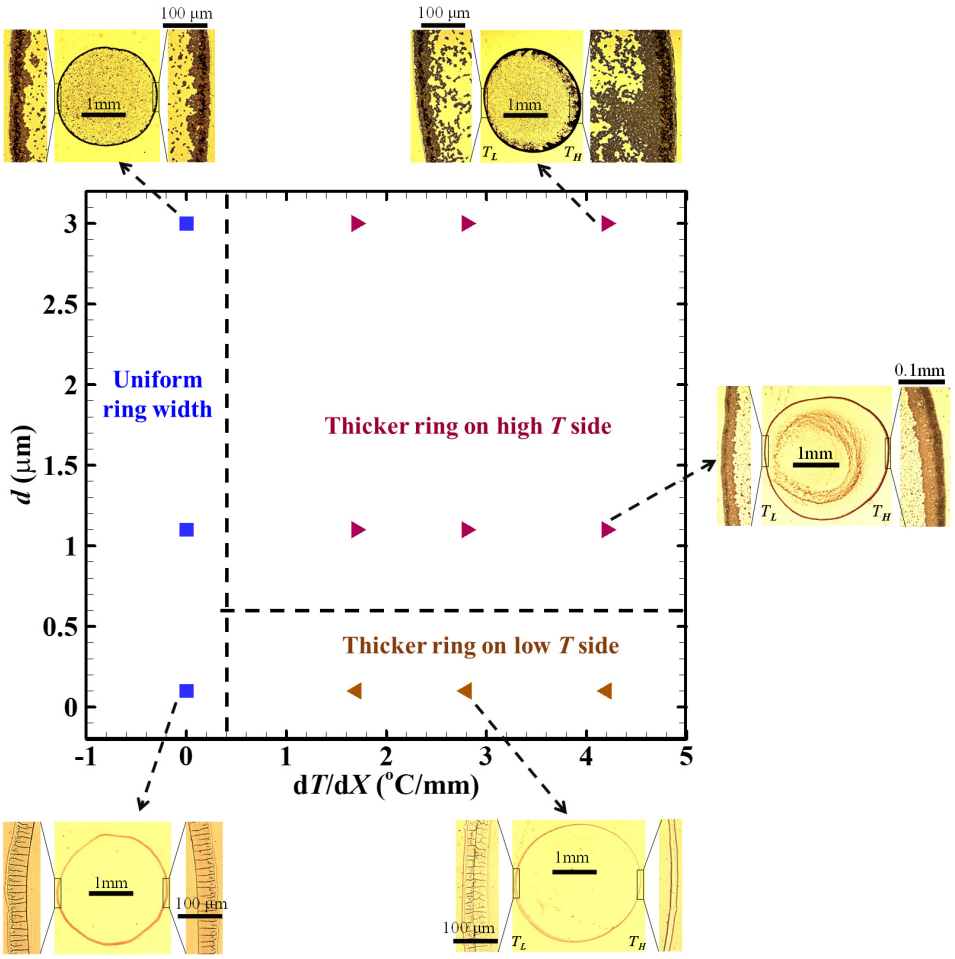

Figure 3.19: Regime map classifying the different deposition patterns obtained as a function of particles size (d) and temperature gradient (dT/dX) imposed on the substrate. The dashed lines are plotted to demarcate the regimes. Insets corresponding to the different regimes are also shown with scale bars. Three regimes are found, namely, uniform ring width, thicker ring on lower temperature side and thicker ring on higher temperature side. The first regime, i.e. coffee-ring effect is well-established in the literature while the regimes with non-uniform ring width are the contribution of the present work. The second regime is explained by asymmetric Marangoni recirculation inside the evaporating droplet and contact line depinning in the presence of the smaller particles. The third regime is the result of the recirculation and the contact line pinning with the larger particles

recirculation as the temperature gradient increases.

A mechanistic model is utilized and it is found that the depinning in case of the smaller particles occurs because the surface tension force on the particles stacked near the contact line overcomes the drag and friction force on them. Finally, a regime map to classify the deposition patterns on a temperature gradient - particles size plane is proposed. Three regimes of deposit pattern are proposed. The first regime is uniform ring width i.e. well-documented coffee-ring effect, corresponds to uniformly non-heated or uniformly heated substrate. The second regime is thicker ring on lower temperature side, explained by asymmetric, twin Marangoni recirculations inside the evaporating droplet and contact line depinning in the presence of the smaller particles. The last and third regime is thicker ring on higher temperature side, attributed to the twin Marangoni recirculation and the contact line pinning with the bigger particles.

Part II

Bouncing Droplets

Chapter 4

Impact Dynamics of a Pure Aqueous Droplet on Microgrooved Surfaces[1]

In this chapter the impact dynamics of a microliter water droplet on a hydrophobic microgrooved surface is investigated experimentally. The surface is fabricated using photolithography and high-speed visualization is employed to record the time-varying droplet shapes in transverse as well as longitudinal direction. The effect of the pitch of the grooved surface and Weber number on droplet dynamics and impact outcome are studied. At low pitch and Weber number, the maximum droplet spreading is found to be greater in the longitudinal direction than the transverse direction to the grooves and the outcome is no bouncing (NB). At higher pitch or Weber number, the following outcomes are obtained - droplet completely bounces off the surface (CB), bouncing occurs with droplet breakup (BDB) or no bouncing due to Cassie to Wenzel wetting transition (NBW). BDB results in droplet breakup alongside bouncing while NBW suppresses the bouncing. These outcomes are demarcated on Weber number-dimensionless pitch plane and the proposed regime map suggests the existence of a critical Weber number or pitch for the transition from one regime to the other.

[1] **LK Malla**, ND Patil, R Bhardwaj, A Neild, "Droplet Bouncing and Breakup during Impact on a Microgrooved Surface" *Langmuir*, 33 (38), 9620-9631. https://pubs.acs.org/doi/abs/10.1021/acs.langmuir.7b02183

Graphical abstract: The impact dynamics of microliter water droplet on hydrophobic microgrooved surfaces, fabricated using standard photolithography techniques and recorded by high-speed visualization to study effect of the pitch of the microgrooved surface and the impact velocity on the impact dynamics as well as on the droplet outcome.

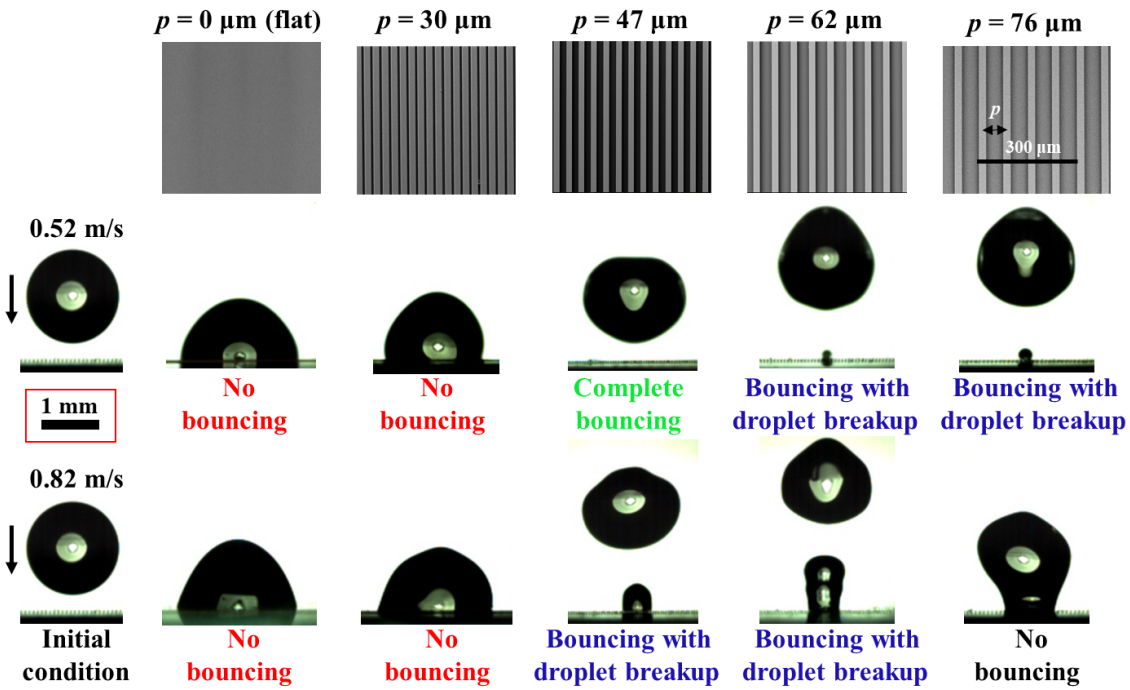

4.1 Introduction

Microtextures on the substrates increase the surface roughness which aids in modifying the contact angle [137] and renders these surfaces as hydrophobic/super-hydrophobic. The impact of the droplet on a microtextured surface is more complex and in general, due to its lower wettability, the droplet may bounce off the surface. The lower wettability is attributed to the Cassie state, in which air is trapped beneath the droplet in the microtextures. If the liquid penetrates the microtextures, leaving no air pockets, it is known as Wenzel state. The penetration of the liquid is attributed to the lesser capillary pressure than the combined hammer and dynamic pressure. In the following section, studies on micropillared and microgrooved surfaces are reviewed.

4.2 Literature review

4.2.1 Studies on isotropic micropillared surfaces

In the context of micropillared isotropic surfaces, Jung and Bhushan [138] reported the wetting behavior of a droplet when it impacts micropatterned (cylindrical pillars) and nanopatterned surfaces. They performed a theoretical analysis to determine the transition criterion from the Cassie state to the Wenzel wetting state by balancing the dynamic pressure and the capillary pressure that acts on the droplet at the point of impact. Deng et al. [139] studied the impact of the droplet over a textured surface with Si posts. They reported that textures at a sub-100 nm scale are essential for a surface to be non-wetting. The effect of the pitch of the pillars and impact velocity play a key role in determining the droplet fate. For instance, bouncing and bouncing with partial penetration of liquid in the pillars as a function of impact velocity was reported by Kwon and Lee [140].

Recently, Patil et al. [24] studied the effect of the pitch of the pillars and the effect of the impact velocity on no bouncing, complete bouncing, and bouncing with droplet breakup behavior of the droplet impact. Very recently, Liu et al. [15] observed "pancake bouncing" of the droplet over a microconical pillared Cu surface at Weber number $(We) > 14.1$. They reported that the diameter of the droplet at the bouncing stage is comparable to the droplet diameter at maximum spreading. They also reported that the stored surface energy due to the penetration of the liquid droplet into the high posts aids in the early upward lift without much recoiling of the droplet. Frankiewicz and Attinger [36] reported the wettability characteristics of etched Cu surfaces with three tiers of roughness and compared the droplet impact dynamics result on these surfaces with those on natural leaves of rice, brassica, and lotus. They put forward the argument that in droplet impact on a hard surface, liquid compressibility comes into effect in the penetration of the droplet liquid into the roughness.

Liu and Kim [18] fabricated SiO_2 surfaces that had microscale cylindrical posts with vertical overhangs. They demonstrated that these double reentrant structures make the surface superrepellent even to low surface tension liquids such as fluorinated solvents. Regarding Cassie to Wenzel wetting transition, previous studies showed that impact velocity [141], equilibrium contact angle [142], the pitch of the pillars [24], wetted diameter [143], the aspect ratio of the pillars [141], droplet volume [144] affect the wetting transition. The transition may result from bouncing to no bouncing off the surface.

4.2.2 Studies on anisotropic microgrooved surfaces

The wetting characteristics of anisotropic, microgrooved surfaces with rectangular grooves and ridges (Figure 4.1) has been reported extensively. These surfaces exhibit anisotropic

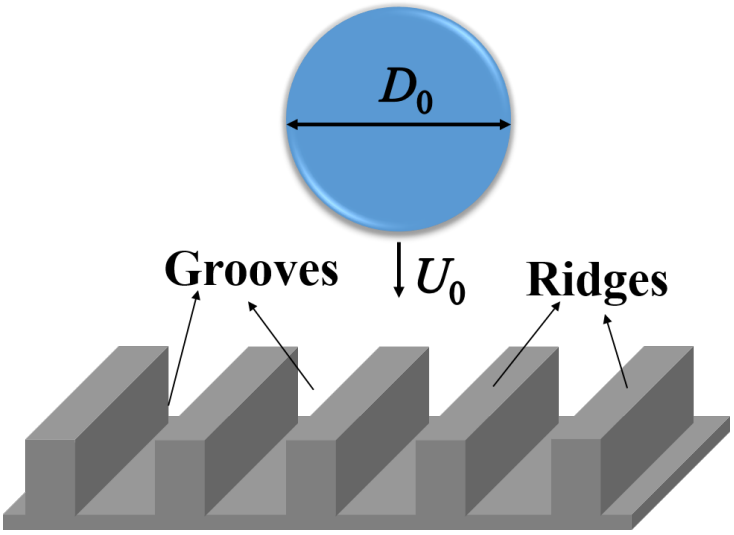

Figure 4.1: Schematic of impact of a droplet of initial diameter D_0 with impact velocity U_0 on a microgrooved surface with rectangular ridges.

wetting, that is, the droplet spreads more in longitudinal direction (along the grooves) as compared to that in transverse direction (normal to the grooves) as shown schematically in Figure 4.2. Chen et al. [145] reported smaller equilibrium contact angle (θ_{eq}) measured in longitudinal direction than that in the transverse direction. Similar findings were reported in Refs. [16] and [146] for wetting behavior of a periodic sub-micrometer-scale grooved surface and two-level hierarchical structure consisting of grating patterns, respectively. Chung et al. [147] reported anisotropic wetting on a microwrinkled surface and observed that the droplet spreading or receding happened in a stick slip manner.

Kusumaatmaja et al. [148] employed sub-micrometer scale corrugated polyimide surfaces and found that the contact angle hysteresis is larger in the transverse direction than that in the longitudinal direction. Yang et al. [149] reported the effect of the droplet volume on the anisotropic wetting behavior on the microgrooved surfaces. For a 1-microliter droplet, the observed droplet water contact angles in both transverse and longitudinal direction of grooves differ greatly from the contact angle that is established by the Cassie model for a rough surface (around 25° greater in transverse direction and 50° lesser in longitudinal direction). Bliznyuk et al. [150] observed the equilibrium state of a water droplet that was gently deposited on shallow grooved surfaces. They found that droplet spreading in the longitudinal direction is more in the Wenzel state. Ma et al. [151] performed an experimental study of the anisotropic silicon carbide surface and found that the difference between the contact angle in the transverse direction with that in the longitudinal direction, increases with increase in the ridge width when the groove width is kept constant.

In the context of droplet impact on microgrooved surfaces (Figure 4.1), Kannan and Sivakumar [152] studied water droplet impact on a stainless steel rectangular grooved surface at $We =$ [50-168]. They found that the grooved structures on the substrate changes

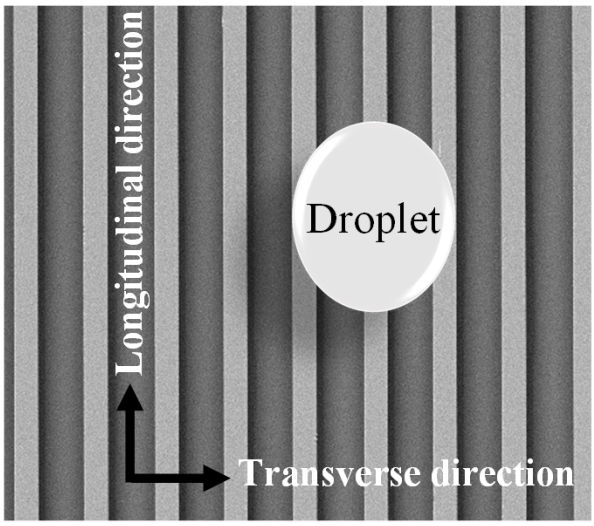

Figure 4.2: Top view of a sessile droplet on an anisotropic microgrooved surface. Light and dark colored patches are ridges and grooves, respectively.

the liquid lamella spreading on the surface. Pearson et al. [153] studied droplet impact dynamics for two types of liquid (water and mixture of water (50%) and glycerol (50%)) on a rectangular microgrooved superhydrophobic surface at We = [1-500]. They observed that the ratio of the maximum wetted diameter in longitudinal to transverse direction starts increasing at $We > 100$. Regarding Cassie to Wenzel wetting transition during droplet impact, Vaikuntanathan and Sivakumar [154] found a critical velocity at which the transition occurs on V-shape microgrooved surface. The critical velocity was found to be function of geometry and wetting of the base material. In a recent paper [155], authors reported that the ratio of the maximum wetted diameter in longitudinal direction to that in transverse direction scales with Weber number in range of [1-100]. Very recently, Yamamoto et al. [156] studied impact of a water droplet on surfaces on which parallel stainless steel razor blades were mounted with pitch of 100 μm and 250 μm. They recorded droplet bouncing at We = [0.04, 5] and the transition at We = [5, 10].

4.3 Objectives

It is well established by previous studies that the droplet preferentially spreads in longitudinal direction as compared to transverse direction on a microgrooved surface. However, most of the previous studies considered large Weber number in which the droplet is most likely in Wenzel state. At low Weber number, the droplet is in Cassie state that may affect the preferential spreading. In particular, the pitch is expected to influence the preferential spreading since previous studies have shown dependence of surface wettability on pitch in Cassie state. The Cassie to Wenzel wetting transition may involve partial penetration

of the liquid into the grooves that could result in breakup of the bouncing droplet. To the best knowledge, these effects have not been described for the droplet impact dynamics on microgrooved surfaces. Therefore, the objective of the present work is to investigate the combined effect of Weber number (We) and pitch (p) on impact dynamics, anisotropic wetting characteristic, Cassie to Wenzel wetting transition, droplet breakup during bouncing and final impact outcome. We consider a microliter water droplet with Weber number, $We = [1.2\text{-}20.4]$ on microgrooved surfaces with wide range of pitch, $p = [30\text{ - }76]\ \mu$m.

4.4 Experimental details

4.4.1 Fabrication and characterization of microgrooved surfaces

Fabrication process of the microgrooved surface was done by the ultraviolet lithography which is a five step process [22]. The steps are shown schematically in Figure 4.3. In the first process, Silicon wafer (2 inch) was RCA cleaned and wet oxidized. Secondly, SU-8 2025 epoxy photoresist polymer was spin coated on the wafer with a speed of 500 rpm for 10 s and 2300 rpm for next 40 s and after that soft baking was carried out at 65°C for 3 min and at 95°C for next 8 min to harden the surface. Previously an iron oxide coated glass mask with rectangular patterns of the requisite ridge widths was printed using Laser Writer, LW405, Microtech Inc. So in the third process, both the prepared surface and glass mask were aligned using double sided aligner (EVG620, EV Group Inc) where the wafer was exposed to UV radiation with intensity of 160 mJ/cm^2 for 2–3 min. Subsequently, they were developed in SU8 photo developer for 5–6 min and cleaned by isopropanol. Fourth process consisted of baking the samples at 65°C for 1 min and 95°C for 6 min and cooling in the ambient. The final stage consisted of hard baking the surface in a heater at 120°C for 10 min and coating with 10 nm platinum layer before the characterization process.

Top view images of the fabricated surfaces were taken using Scanning electron microscope (SEM) as shown in Figure 4.4(a) for four different pitches (30 μm, 47 μm, 62 μm, 76 μm). The characterization of the grooves depth and surface morphology on the microgrooved surfaces is shown as 3D images in Figure 4.4(b) and as 2D line plot for cross-section surface profile in Figure 4.4(c). The images were captured using 3D optical profilometer (Zeta-20, Zeta Instruments Inc. The rectangular ridge width (w) and groove depth (h) are 22 $\pm$ 2 μm and 27 $\pm$ 2 μm, respectively, for all the surfaces. Variation in the groove width provides the requisite pitch.

4.4.2 Droplet generation and high-speed visualization

The experimental setup shown in Figure 4.5, consists of two high-speed cameras connected to a computer, a syringe with an adjustable stand to vary the height (or impact velocity) and

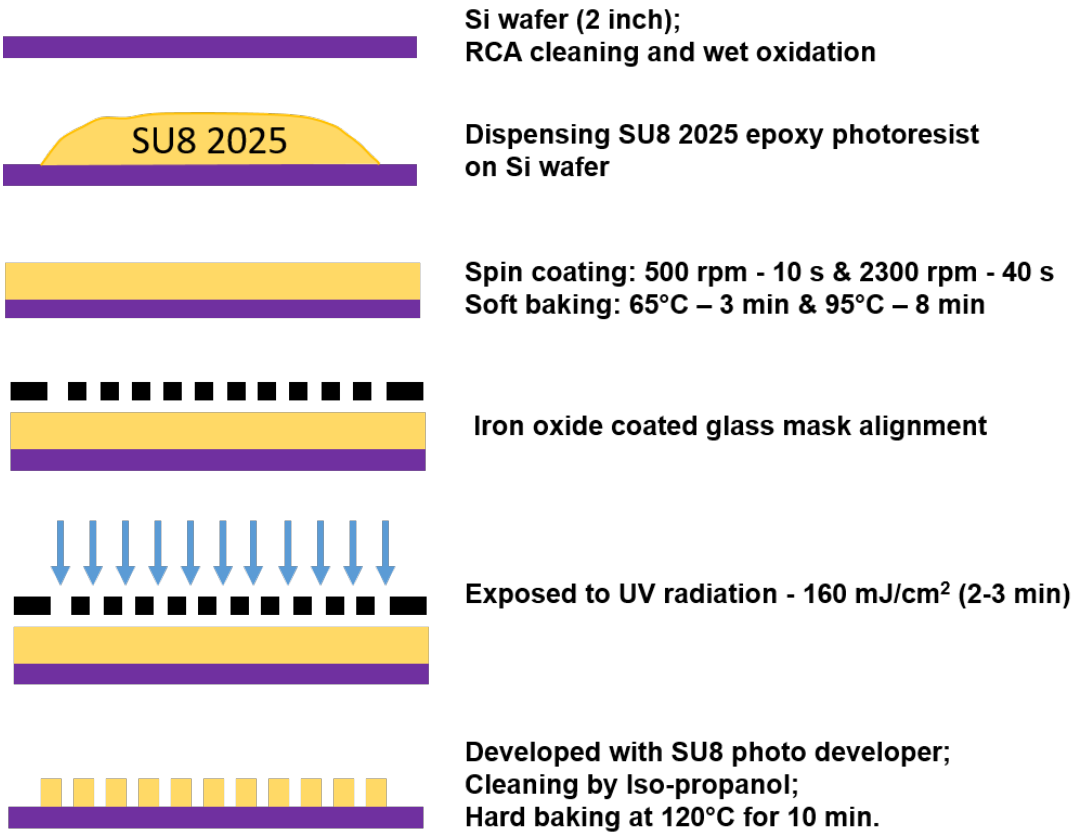

Figure 4.3: Schematic of the steps involved for the fabrication of microgrooved surfaces using ultraviolet lithography. Adapted from Ref. [22]

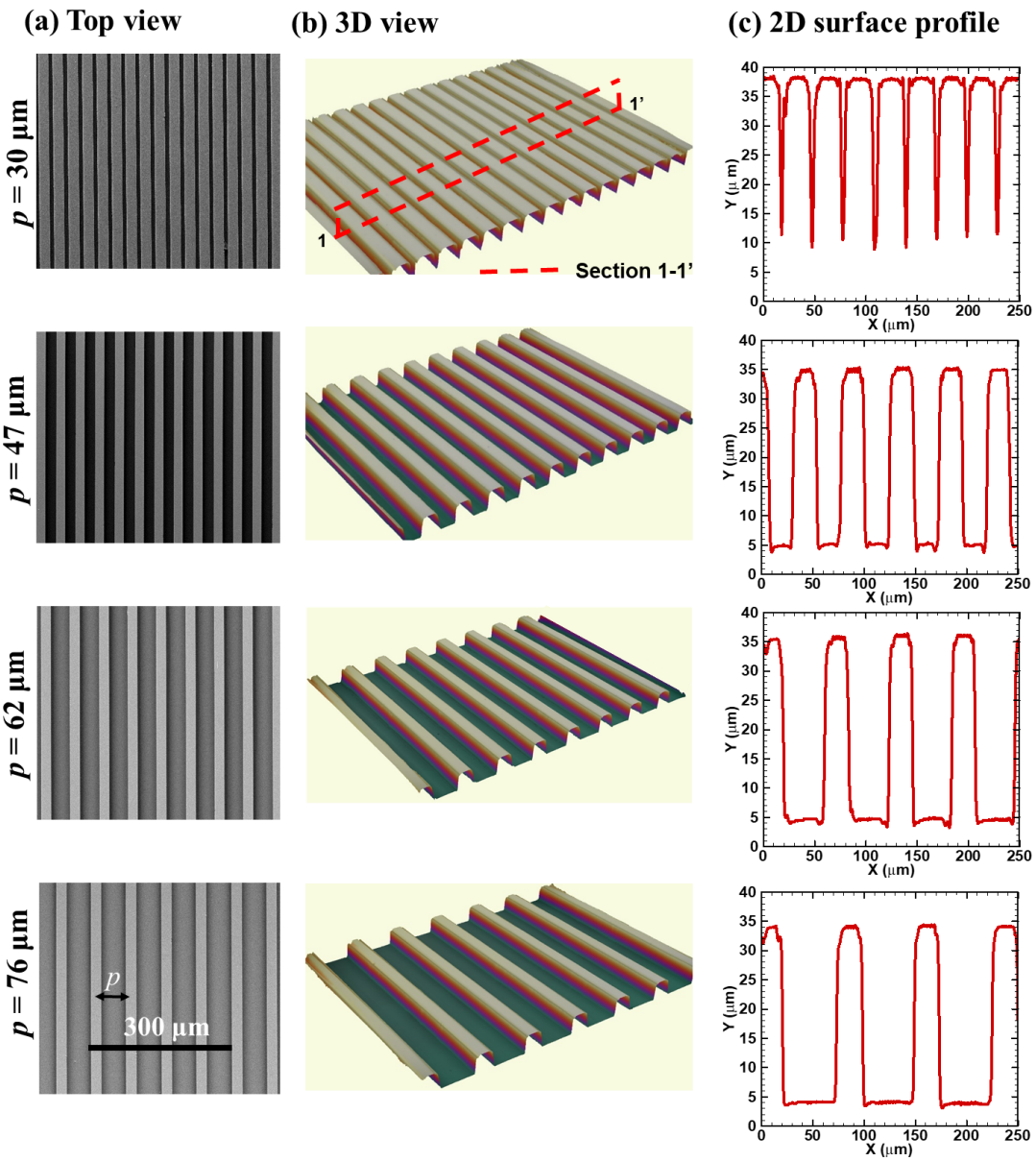

Figure 4.4: Characterization of microgrooved surfaces of different pitches (p). (a) Top view of the surfaces obtained by SEM. Scale is shown in image plotted in last row and first column. (b) 3D view of the surface obtained by optical profilometer. (c) 2D cross-sectional profiles obtained using 3D profilometer data. The cross-section plane 1-1' is shown in first row and second column.

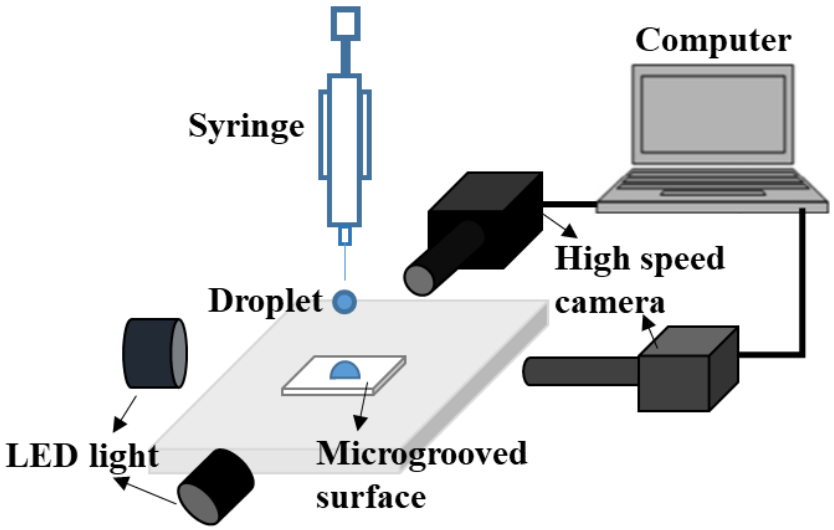

Figure 4.5: Schematic of the experimental setup.

two LED lamps. Microliter deionized water droplets are generated using the syringe with 31-gauge needle. The droplet diameter and range of impact velocity are 1.7±0.05 mm and [0.22 - 0.92] m/s, respectively. The high-speed cameras are used to visualize the droplets in planes transverse and longitudinal to the direction of the grooves, as shown in Figure 4.2 (Motion- Pro Y-3 classic camera in transverse direction and PixeLINK PL-C722MU-BL in longitudinal direction). A long distance working objective (Qioptiq Inc.) is used with the two cameras. Two white LED lamps serve as a back light source. The magnification corresponds to 14 μm per pixel and 29 μm per pixel for the transverse and longitudinal view, respectively. The videos are recorded at 1500 and 750 frames per second (fps) in the transverse and longitudinal view, respectively.

4.4.3 Measurement of contact angle

Advancing contact angle (θ_{adv}), receding contact angle (θ_{rec}) and the contact angle hysteresis (CAH) are measured in the transverse and longitudinal direction as shown in Figure 4.6(a) and (b) respectively. Captive droplet method is used to measure the θ_{adv} and sessile droplet evaporation technique is used for measuring θ_{rec}. Equilibrium contact angle (θ_{eq}) is measured for a gently deposited droplet on the surface, using the following equation considering a sessile spherical cap on the surface, $\theta_{eq} = 2tan^{-1}(2H/D_{wetted})$ where H and D_{wetted} are sessile cap height and wetted diameter, respectively. The increasing contact angle value with increase in pitch shows that the decrease in surface wettability with increase in the pitch of the grooves. The angles and CAH are larger in the transverse direction than in the longitudinal direction, consistent with data of Kusumaatmaja et al. [148]. The uncertainty in the contact angle measurements is ±5°. All the experiments are performed at 25±2 °C and 50 ± 5% relative humidity and are repeated three times to ensure

repeatability.

4.5 Theory of Cassie to Wenzel wetting transition

In this section, the possible pressures acting on the droplet which leads to the penetration of the liquid into the microgrooves of the surface and also the two transition mechanisms by which the droplet penetrates into the microgrooves are discussed. Liquid penetration into the microgrooves of the surface can occur in three stages: the impact stage, the spreading stage, and the receding stage [157]. In the impact stage, the interaction between the droplet and the microgrooved surface generates three pressure forces: hammer pressure ($\triangle P_{\mathrm{H}}$), dynamic pressure ($\triangle P_{\mathrm{D}}$), and capillary pressure ($\triangle P_{\mathrm{C}}$) [139, 140, 157, 158]. Just after the impact, there is a sudden change in the velocity inside the droplet, which creates shock waves. This shock front compresses the droplet liquid behind it, and as the shock front reaches the edges of the rectangular ridges, the compressed liquid suddenly expands, acquiring free space. Thus, the liquid-gas interface experiences a thrust from the compressed liquid above it, which is known as the hammer pressure [139] and is expressed as [159]:

$$\triangle P_{\mathrm{H}} = \alpha \rho C U_0 \tag{4.1}$$

where α is the coefficient that is found empirically from the experimental results, ρ and C are the density of the droplet liquid and the speed of the sound in the droplet liquid, respectively, and U_0 is the impact velocity. The coefficient, α, gives us the fraction of impact velocity, U_0, at which the compression wave travels through the spherical droplet [159]. Different values of the coefficient, α, which are used in the literature, are reported in Table 4.1. The speed of sound in the droplet liquid (C) is considered to be 1482 m/s. The dynamic pressure is given as [157]:

$$\triangle P_{\mathrm{D}} = 0.5 \rho {U_0}^2 \tag{4.2}$$

Study by	Substrate	Impact velocity	α
Engel, 1955 [159]	Glass	4.84 m/s	0.2
Deng et al., 2009 [139]	Silicon	3 m/s	0.2
Kwon and Lee, 2012 [140]	SU-8	1.2 m/s - 3.1 m/s	0.003
Quan and Zhang, 2014 [160]	SU-8	1.89 m/s	0.003

Table 4.1: Reported values of coefficient for estimating water hammer pressure, α, using eq. 4.1 for impact of water droplet on different substrates.

The capillary pressure is defined as the Laplace pressure acting along the air-liquid interface beneath the droplet and is given as [34]:

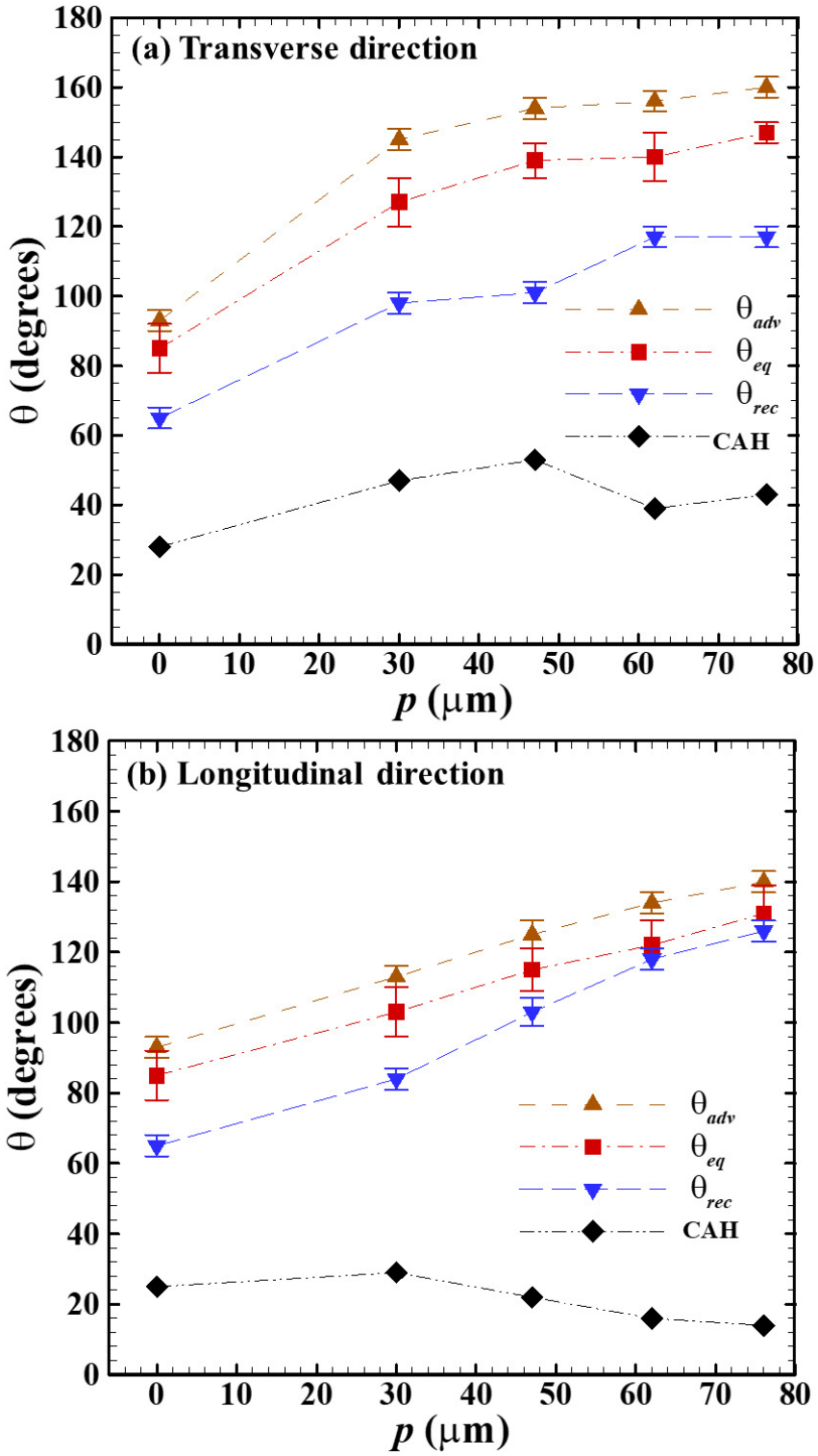

Figure 4.6: (a) Measured advancing contact angle (θ_{adv}), equilibrium contact angle (θ_{eq}), receding contact angle (θ_{rec}) and contact angle hysteresis (CAH) for flat and microgrooved surfaces of various pitches (p) in the transverse direction. (b) Corresponding angles and hysteresis in the longitudinal direction.

$$\triangle P_C = \gamma H \tag{4.3}$$

where γ and H are surface tension and curvature of the interface, respectively. Since $\triangle P_H$ and $\triangle P_D$ act as wetting pressure, and $\triangle P_C$ acts as anti-wetting pressure [138, 139, 141, 161], a criterion for the Cassie to Wenzel wetting transition is given as follows:

$$\triangle P_H + \triangle P_D - \triangle P_C \geq 0 \tag{4.4}$$

The transition of the droplet from the Cassie state to the Wenzel state occurs in two mechanisms, namely, the de-pinning and the sagging mechanism [141, 162], which are described in the following subsections.

4.5.1 Depinning mechanism

As observed in the Cassie state, the liquid-air interface hangs in between the ridges, that is, inside a groove, and the balance of capillary pressure is on the surface against the combined dynamic pressure and hammer pressure. The transition from the Cassie state to the Wenzel state occurs when wetting pressures (dynamic pressure and hammer pressure) exceed the capillary pressure, and the droplet cannot remain pinned at the ridge edge. The droplet slides downward on the sides of the ridge, as shown in Figure 4.7(left). The capillary pressure in the de-pinning mechanism can be calculated as [157]:

$$\triangle P_C = \frac{-2\gamma \cos\theta_{adv}}{p - w} \tag{4.5}$$

where γ is the surface tension of the liquid droplet, θ_{adv} is the advancing contact angle on the flat surface [141], p is the pitch of the microgrooves and w is the ridge width.

4.5.2 Sagging mechanism

Due to excess wetting pressures, liquid-air interface curvature can increase and touch the base of a microgroove, which leads to the transition from the Cassie state to the Wenzel state [141]. This type of transition mechanism is called the sagging mechanism as shown in Figure 4.7(right). The critical height of the microgroove required for sagging is [163],

$$h_c = \frac{p - w}{2} \tan\frac{\theta_{adv} - 90^\circ}{2} \tag{4.6}$$

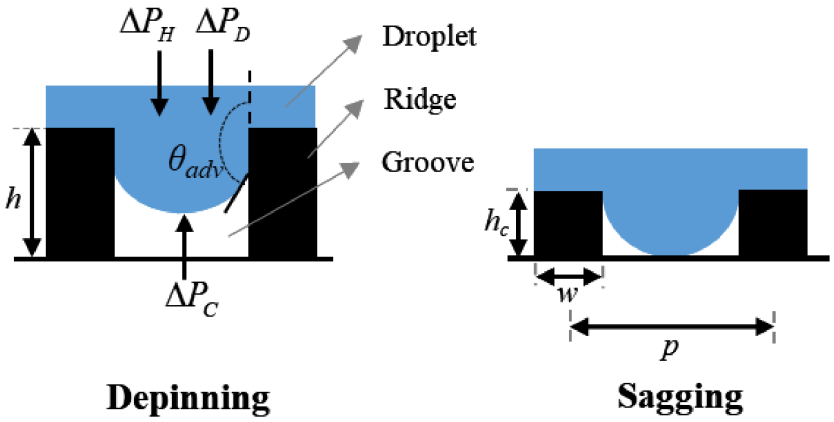

Figure 4.7: Droplet penetration into the microgrooves could occur by depinning of the contact line (left) or by sagging of the liquid-air interface (right).

4.6 Results and discussions

Results are presented for the impact of 1.7 mm water droplet on microgrooved surfaces with impact velocity and pitch in range of U_0 = [0.22 - 0.92] m/s and p = [30 - 76] μm, respectively, in the following subsections. The corresponding range of Reynolds number ($Re = \rho U_0 D_0/\mu$), Weber number ($We = \rho U_0{}^2 D_0/\gamma$), and dimensionless pitch (p/D_0) are Re = [429, 1794], We = [1.2, 20.4] and p/D_0 = [0, 0.045], respectively, where ρ, U_0, D_0, μ and γ are density, impact velocity, initial droplet diameter, dynamic viscosity and surface tension, respectively. The impact conditions of We = [1.2 - 20.4] and Z = 0.00253, which are used in this study, fall into the inviscid and impact-driven region [23], as shown in Figure 4.8. In the following subsections, the effect of dimensionless pitch and We on the impact dynamics are discussed.

4.6.1 Effect of pitch

The wetting characteristics of the surfaces with different pitches (quantified in Figure 4.6) shows that the angles and CAH are larger in the transverse direction than in the longitudinal direction. As explained by Chen et al. [145], the larger spreading in the longitudinal direction (or larger angles in the transverse direction) is due to the pinning of the contact line at the edge of the ridge while spreading in the transverse direction. This results in squeezing of the droplet in the transverse direction and stretching of the droplet in the longitudinal direction. These results show the anisotropy wetting characteristic of the microgrooved surfaces.

Figure 4.9 compares the droplet impact dynamics on flat and microgrooved surfaces with four different pitches, p = 30 μm, 47 μm, 62 μm, 76 μm. The Weber number in all cases is We = 6.5 that corresponds to impact velocity of U_0 = 0.52 m/s. The impact sequences

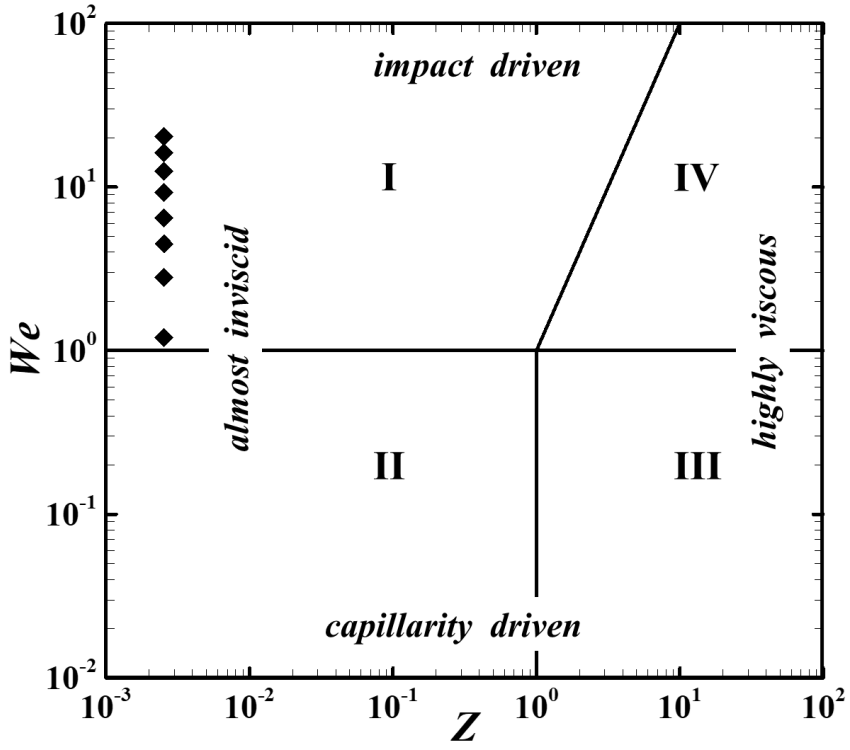

Figure 4.8: Impact regimes given by Schiaffino and Sonin [23]. Present experimental conditions shown as diamond points, corresponds to regime I

obtained by high-speed visualization in the transverse direction are compared columnwise in Figure 4.9 and top insets shows the topology of the surface, recorded by SEM. The droplet initially spreads due to inertial and wetting forces ($t < 3.33$ ms) and large deformation of the liquid-gas interface is observed. The surface forces cause the recoiling and the contact line recedes radially inwards. At $t = 11.33$ ms, the droplet does not bounce on the flat as well as $p = 30$ μm surface and bounces on the $p = 47$ μm surface. The droplet bounces on the surfaces with pitch $p = 62$ μm and $p = 76$ μm, however, a small volume of the droplet is left on the surface due to droplet breakup (Figure 4.9).

These three outcomes are referred to as – no bouncing (NB), complete bouncing (CB) and bouncing with droplet breakup (BDB), respectively, hereafter. The CB is explained due to lower wettability (or larger equilibrium contact angle, θ_{eq}) at larger pitch (Figure 4.6 (a) and (b)). In terms of the energies involved, the kinetic energy of the droplet converts into the surface energy until the maximum spreading and during recoiling the surface energy converts into the kinetic energy. If the sum of kinetic and surface energy exceeds the initial surface energy during recoiling, the droplet bounces off the surface [51, 52]. The measured bouncing times are in good agreement with the analytical model of Richard et al. [164] ($t \sim \sqrt{\rho {D_0}^3/\gamma} = 8.2$ ms) and the measured wetted diameter (D_{wetted}) on the flat surface (~ 2.7 mm) and microgrooved surfaces (~ 2.5 mm) are consistent with prediction of an analytical model reported by Clanet et al. [10]($D_{max} \sim D_0 We^{1/4} \sim 2.7$ mm).

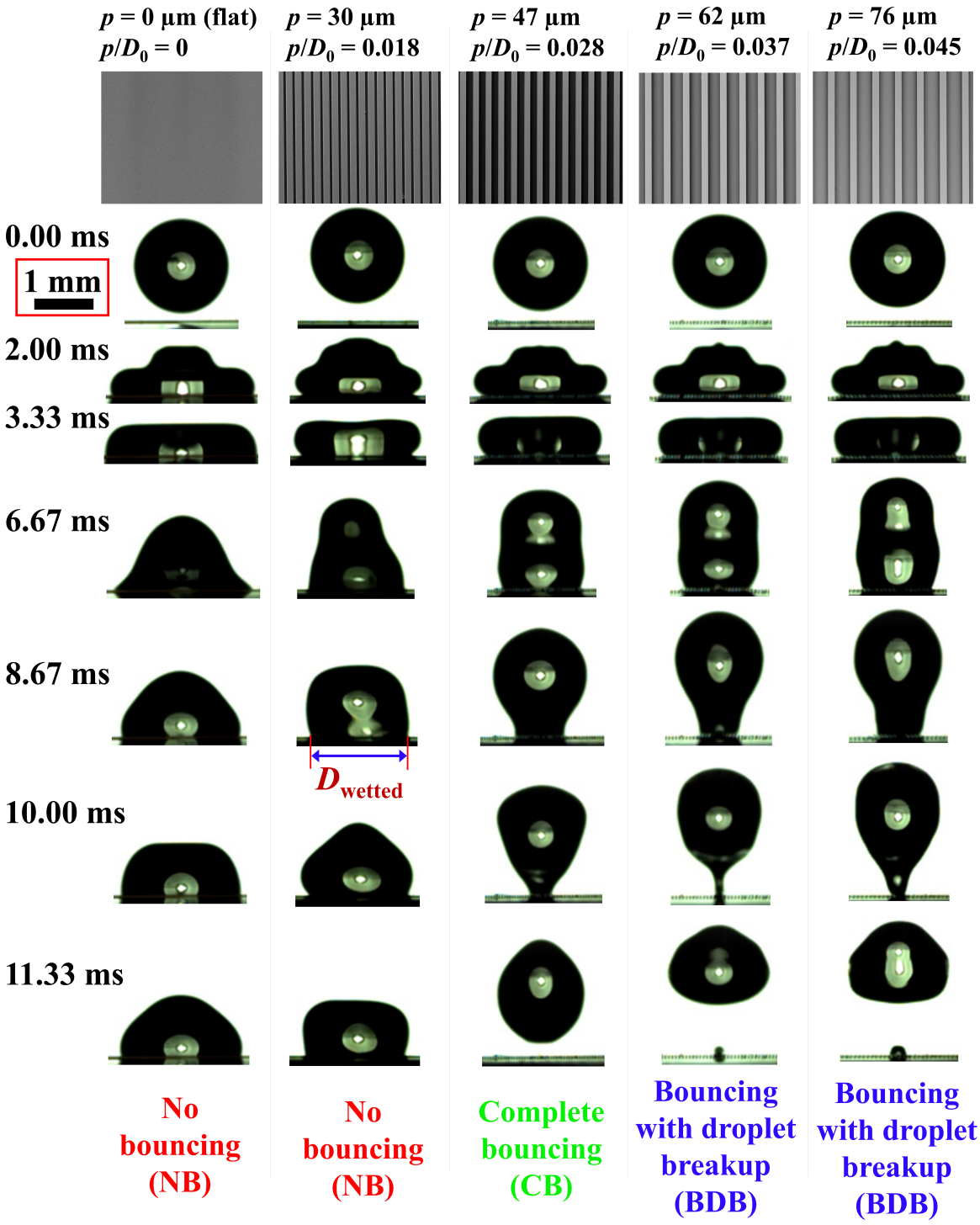

Figure 4.9: Image sequence obtained by high-speed visualization in transverse direction for impact of a microliter water droplet of 1.7 mm diameter on a flat and microgrooved surfaces of various pitches (p) at Weber number, $We = 6.5$ ($U_0 = 0.52$ m/s). Columns show different cases of pitch and scale is shown at top-left.

The impact dynamics is further quantified by plotting the time-varying dimensionless wetted diameter (D^*_{wetted}, normalized with respect to the initial droplet diameter) in the transverse and longitudinal direction in Figure 4.10 (a) and (b), respectively. The time scale (t) is nondimensionalized as $t^* = tU_0/D_0$. D^*_{wetted} is compared for surfaces with different pitches and it increases to a maxima during initial spreading and further decreases due to the receding in all cases at $t^* < 3$. The maximum corresponds to the flat surface due to its largest wettability (Figure 4.6 (a) and (b)). D^*_{wetted} attains a plateau value after the droplet becomes sessile on the surface for NB at $t^* > 3$. In Figure 4.10, $D^*_{wetted} = 0$ and $D^*_{wetted} < 0.3$ denote CB and BDB, respectively. In cases of BDB, D^*_{wetted} stays almost constant for $3 < t^* < 12$ and is slightly larger for $p = 76$ μm surface as compared to $p = 62$ μm surface. The latter is due to the fact that a larger pitch surface captures a larger volume of water into the grooves during Cassie to Wenzel wetting transition. starts increasing after the droplet reimpacts for CB and BDB at around $t^* = 6$ and 11, respectively (Figure 4.10).

The maximum spreading is larger in the longitudinal direction than in the transverse direction in Figure 4.10(a) and (b), which is attributed to anisotropic wetting charateristic of the surface. In order to quantify this, the percentage change in the maximum wetted diameter in the longitudinal direction with respect to that in the transverse direction (η) at a given dimensionless pitch (p/D_0) is defined as follows,

$$\eta(\%) = \frac{D_{wetted,max,longitudinal} - D_{wetted,max,transverse}}{D_{wetted,max,longitudinal}} \times 100 \tag{4.7}$$

Figure 4.11 plots the variation of η with dimensionless pitch (p/D_0) at $We = 6.5$. Note that the spreading is considerably larger in the longitudinal direction in all cases and $\eta = 27\%$, 22%, 19%, and 17% for $p/D_0 = 0.018$, 0.028, 0.037, and 0.045, respectively.

4.6.2 Effect of Weber number

The effect of the Weber number (We) is investigated by varying it in range of $We = [1.2, 20.4]$ on a $p = 47$ μm surface ($p/D_0 = 0.028$). The corresponding range of the impact velocity is $U_0 = [0.22, 0.92]$ m/s. The images acquired by the high-speed visualization in Figure 4.12 show NB for $We = 2.8$ ($U_0 = 0.34$ m/s) and $We = 4.5$ ($U_0 = 0.43$ m/s), CB for $We = 6.5$ ($U_0 = 0.52$m/s) and $We = 9.3$ ($U_0 = 0.62$ m/s), and BDB for $We = 16.2$ ($U_0 = 0.82$ m/s). In all cases, most of the initial kinetic energy converts into surface energy upon impact whilst some is also dissipated during the spreading processes due to viscosity [10]. As such, an increase in the initial kinetic energy gives rise to an increase in the surface energy stored, which in turn aids the receding of the droplet after spreading. As explained earlier, CB and BDB occurs if the sum of kinetic and surface energy exceeds the initial surface energy during recoiling.

The corresponding time-variation of D^*_{wetted} in transverse and longitudinal direction

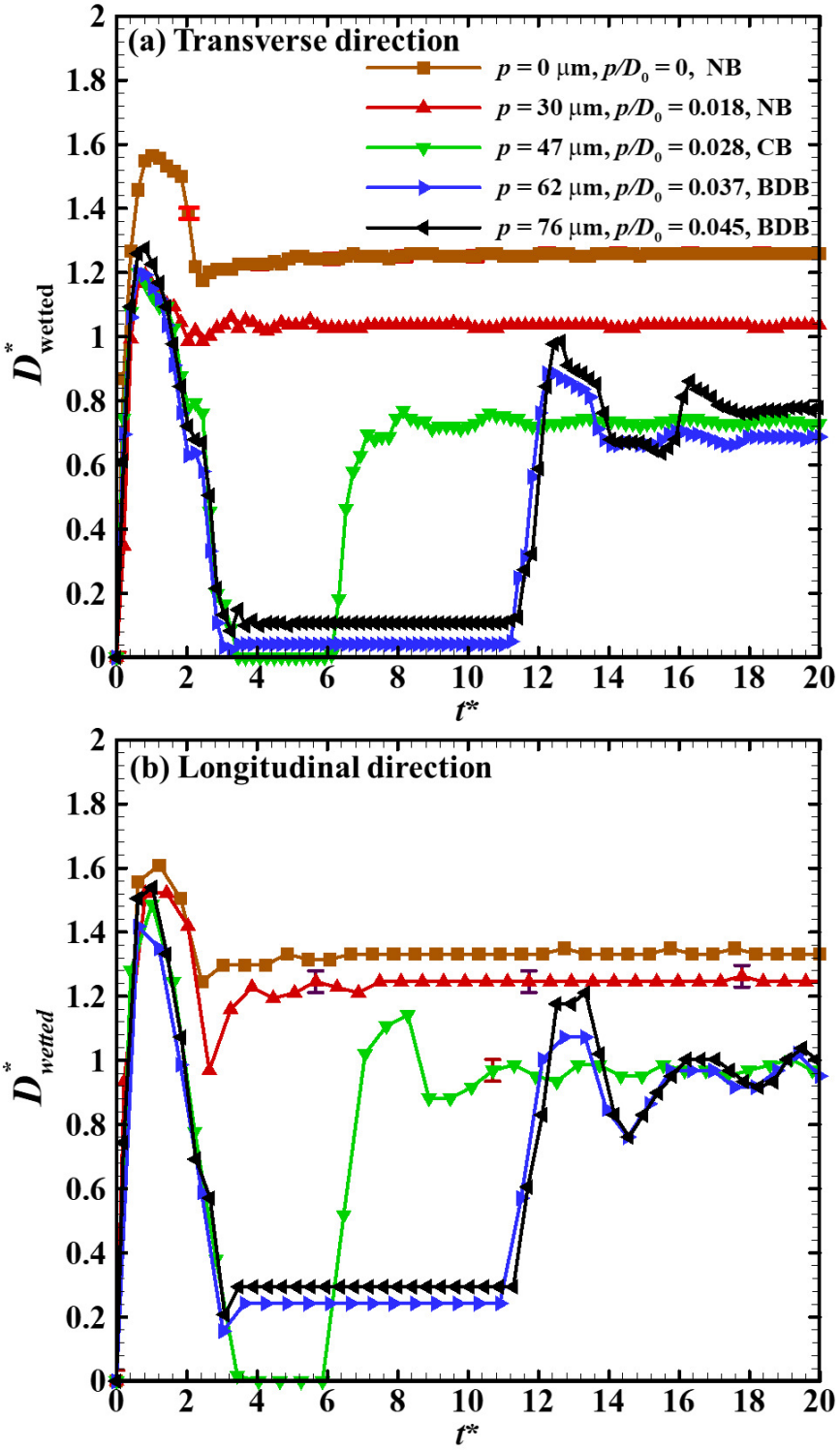

Figure 4.10: Time-varying dimensionless wetted diameter (D^*_{wetted}) for water droplet impact on flat surface and microgrooved surfaces of various pitches (p) at $We = 6.5$ ($U_0 = 0.52$ m/s) in transverse (a) and longitudinal (b) direction. Different outcomes are obtained, namely, no bouncing (NB), complete bouncing (CB) and bouncing with droplet breakup (BDB). Temporal resolution in longitudinal direction is approximately half to that in transverse direction.

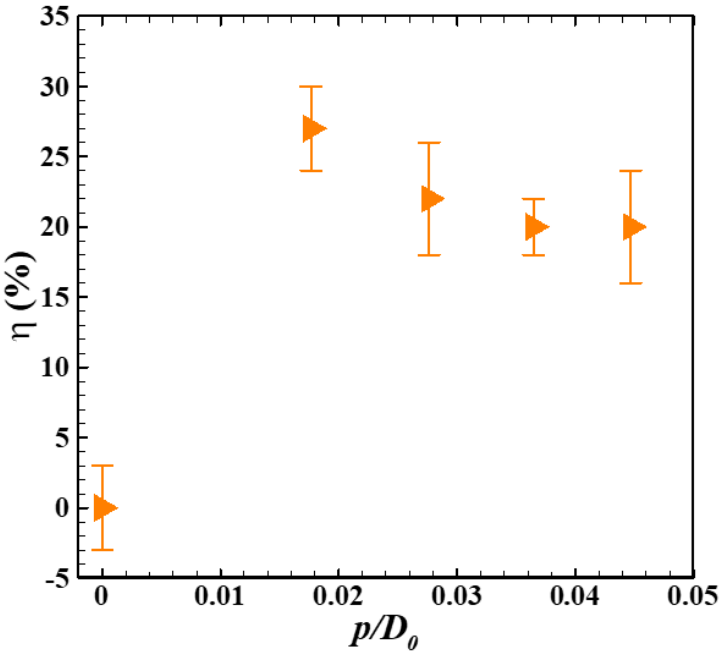

Figure 4.11: Percentage increase in the maximum spreading in longitudinal direction with respect to that in the transverse direction (η, eq. 4.7) as function of dimensionless pitch (p/D_0) for Weber number, $We = 6.5$ ($U_0 = 0.52$ m/s).

for the $p = 47$ μm surface is shown in Figure 4.13(a) and (b), respectively. As expected, the instance of maximum spreading scales with impact velocity ($t_{spreading} \sim D_0/U_0$ [57]). A larger impact velocity results in larger spreading as well as receding of the contact line, as shown in Figure 4.13. In cases of CB ($D^*_{wetted} = 0$), the droplet remains in air for longer time for larger Weber number (or impact velocity). In Figure 4.13(b), the oscillations of D^*_{wetted} in the longitudinal direction after completion of the recoiling for NB and after reimpact of the droplet for CB and BDB are noted. These oscillations are attributed to the conversion of kinetic and surface energy into each other [52] and were also observed for the impact of a water droplet on glass [11, 13]. The amplitude of the oscillation decays with time due to viscous dissipation of the energies and eventually the droplet reaches to a sessile state. The oscillations are absent in the transverse direction since contact line pins at the microgroove edge that is anisotropic wetting of the surface.

Further, the anisotropic wetting as function of the Weber number (We) and dimensionless pitch (p/D_0) is quantified. Figure 4.14 plots the percentage change in the maximum wetted diameter in the longitudinal direction with respect to that in the transverse direction (η, eq. 4.7) as function of the dimensionless pitch (p/D_0) for different cases of We. At low We, η is larger and decreases with p/D_0. This is due to the pinning of the contact line at the edge of the ridge, which causes obstruction for the droplet to spread in the transverse direction. The chances of the obstruction are larger at lower p/D_0 because of presence of higher number of the ridges beneath the droplet. However, η stays constant ($\sim$ 20 - 30%) at

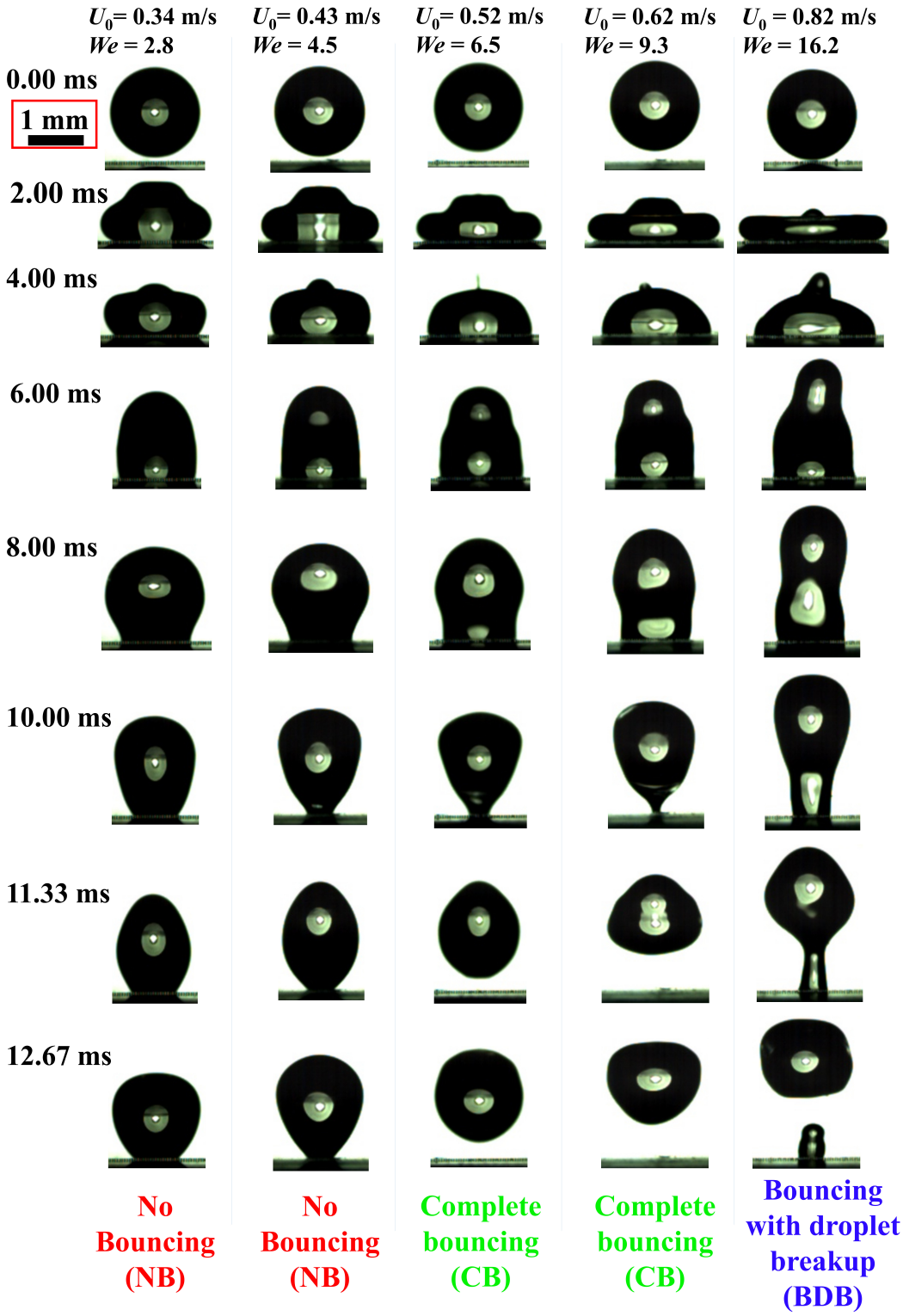

Figure 4.12: Image sequence obtained by high-speed visualization in transverse direction during impact of a microliter water droplet of 1.7 mm diameter on a microgrooved surface of pitch, $p = 47$ μm. Columns show different cases of Weber number (or impact velocity) and scale is shown on top-left.

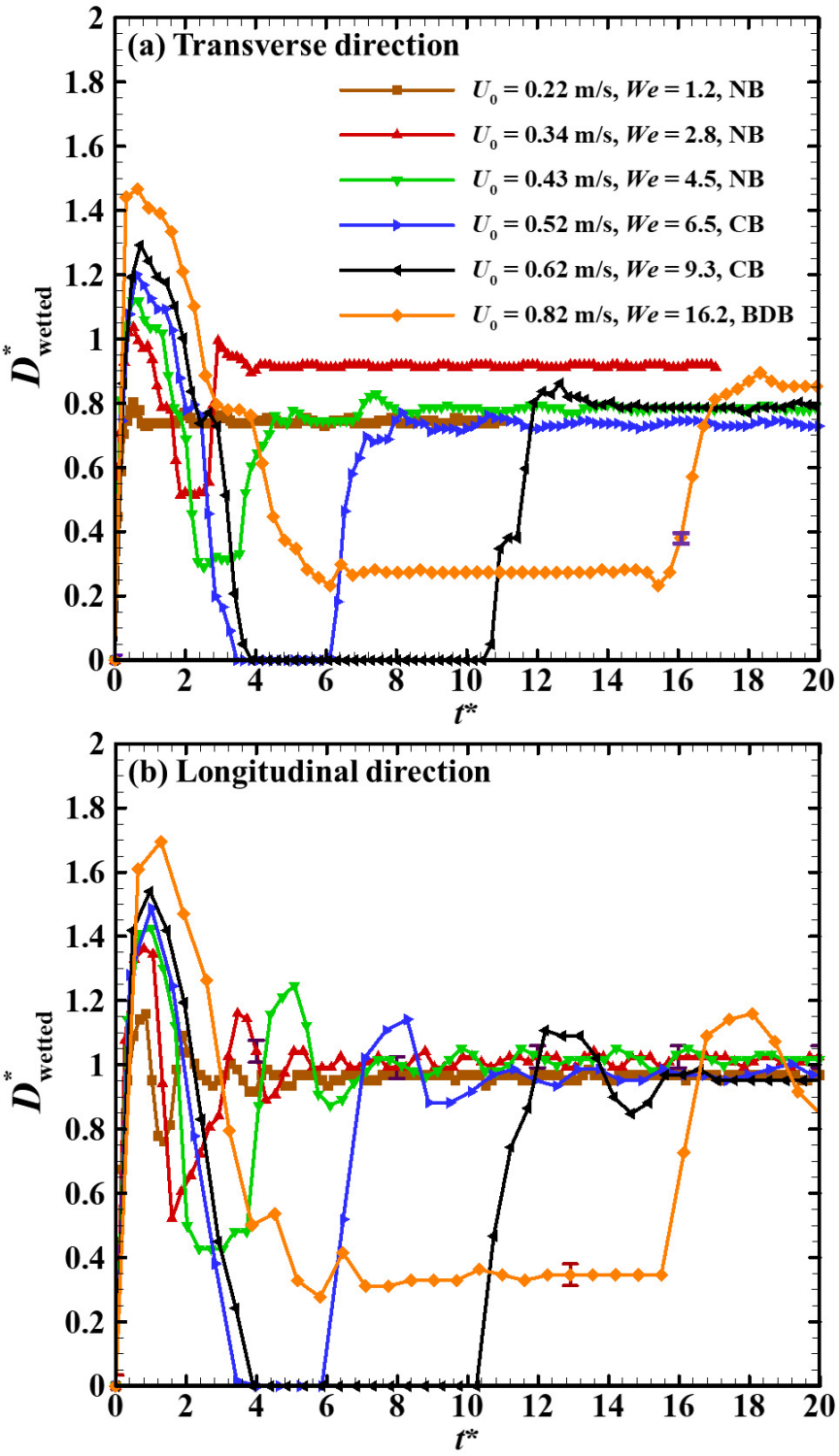

Figure 4.13: Time-varying dimensionless wetted diameter (D^*_{wetted}) of water droplet impact on a pitch surface of 47 μm with various Weber numbers (or impact velocities) in transverse (a) and longitudinal (b) direction. Different outcomes are obtained, namely, no bouncing (NB), complete bouncing (CB) and bouncing with droplet breakup (BDB). Temporal resolution in longitudinal direction is approximately half to that in transverse direction. Only few error bars are shown for clarity.

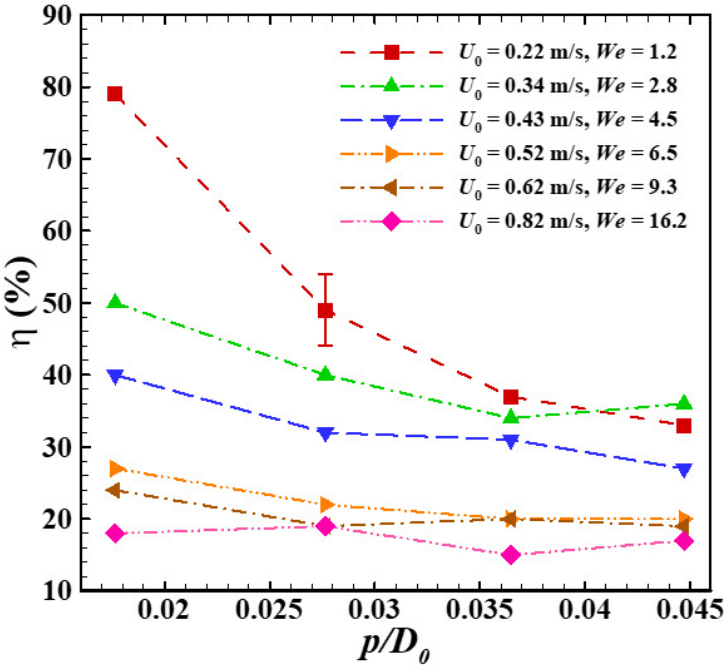

Figure 4.14: Percentage increase in the maximum spreading in longitudinal direction with respect to that in transverse direction (η, eq. 4.7) as function of dimensionless pitch (p/D_0) for different cases of Weber number (or impact velocity). Only one error bar is shown for clarity.

larger We because the kinetic energy dominates over the surface energy at larger We and consequently, the preferential spreading in the longitudinal direction suppresses, as seen in Figure 4.14. The largest η, $\eta = 80\%$, is obtained for $p/D_0 = 0.018$ ($p = 30$ μm), $We = 1.2$ ($U_0 = 0.22$ m/s).

4.6.2.1 Variation of surface energy

The variation of the total surface energy of the droplet with respect to time is computed by analyzing the time-varying high speed camera images for $p = 47$ μm case, and is shown in Figure 4.15. First, the surface area of the liquid-gas interface above the substrate is calculated for a particular image by the following steps:

1. Digitization of the images with in-built Matlab based code for getting the pixel numbers.

2. Division of the height of the droplet into small Δh, here it is the pixel size.

3. For a particular Δh, there is a particular radius of the droplet and for small Δh, the surface of the droplet is assumed to be a vertical and the base of the droplet is assumed to be a circle.

4. The surface area of the droplet for small Δh, can be calculated as $dA = 2\pi r \Delta h$.

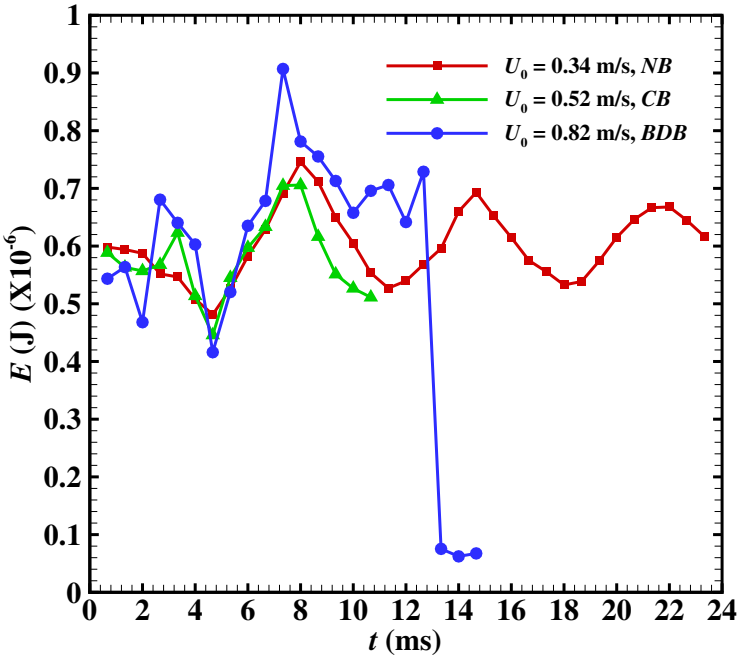

Figure 4.15: Time-varying total surface energy stored in the liquid-gas interfaces at different impact velocities for $p = 47$ μm.

5. Then, the total surface area of the liquid-gas interface (A_{LG}) is obtained by integrating dA over the entire height of the droplet.

The total liquid-gas surface area on a microtextured surface is then calculated as $A_{LG} + ((\pi/4)D^2(1-\phi))$ and the solid-liquid surface area is $(\pi/4)D^2\phi$, where ϕ is the solid-liquid surface fraction and D is the spreading diameter of the droplet at that time instant. The total surface energy for a particular time instant is then calculated as, $(A_{LG} + ((\pi/4)D^2(1-\phi)))\gamma_{LG} + ((\pi/4)D^2\phi)(\gamma_{SL} - \gamma_{SG})$.

4.6.2.2 Cassie to Wenzel wetting transition

The Cassie to Wenzel wetting transition on the microgrooved surfaces is examined in this section. As shown in Figure 4.16, the droplet impact on $p = 76$ μm surface results in NB at $We = 1.2$ ($U_0 = 0.22$ m/s), CB at $We = 2.8$ ($U_0 = 0.34$ m/s), $We = 4.5$ ($U_0 = 0.43$ m/s), BDB at $We = 6.5$ ($U_0 = 0.52$ m/s), $We = 9.3$ ($U_0 = 0.62$ m/s) and again no bouncing at $We = 16.2$ ($U_0 = 0.82$ m/s). Therefore, a critical Weber number (or impact velocity) exists at which the droplet outcome changes from CB to BDB and the liquid penetrates into the grooves. The no bouncing at $We = 16.2$ ($U_0 = 0.82$ m/s) is due to the Cassie to Wenzel wetting transition and is referred to as – no bouncing due to the wetting transition (NBW). The time-varying droplet shapes for NBW are plotted in Figure 4.17. The microgrooves are visible in Figure

4.17 before the impact at $t = 0$ ms and air-filled and liquid-filled microgrooves are visible beneath the droplet at 1.33 ms. In addition, capillary wave propagation is visible on the liquid-gas interface at 1.33 ms. From 4.67 ms to 6.67 ms, the contact line recedes and the droplet recoils, however, it sticks in the microgrooves due to the penetration of water into the grooves and does not bounce. Whereas, for the CB case on $p = 76$ μm surface at We = 4.5 ($U_0 = 0.43$ m/s) in Figure 4.18, the microgrooves beneath the droplet are completely filled with air during spreading at $t = 2.67$ ms, receding at $t = 6.00$ ms and bouncing at t = 9.33 ms in Figure 4.18. The droplet remains in Cassie state even after it impacts again at 44.67 ms.

Further, the critical We required for the wetting transition is calculated using the existing theory presented earlier and is compared with measurements for three cases of the pitch, $p = 47$ μm, 62 μm and 76 μm, corresponding to dimensionless pitch, $p/D_0 = 0.028$, 0.037, and 0.045. As discussed earlier, the droplet penetrates inside the microgrooves if the combined wetting pressure ($\triangle P_H + \triangle P_D$) exceeds the capillary pressure ($\triangle P_C$). The critical height estimated using eq. 4.6 for the wetting transition due to the sagging of the interface (Figure 4.7(right)) for $p = 47$ μm, 62 μm and 76 μm is on the order of 1 μm. Since the height of the ridge is 27 μm, the wetting transition occurs by depinning of the contact line (Figure 4.7 (left)) in the present measurements. The critical We is estimated using dimensionless form of eq. 4.5, expressed as follows,

$$\triangle {P^*}_H + \triangle {P^*}_D = \triangle {P^*}_C \tag{4.8}$$

where superscript $*$ denotes dimensionless variable normalized with $\rho {U^2}_0$. The coefficient α in the expression of the dimensionless hammer pressure ($\triangle {P^*}_H = \alpha C/U_0$, dimensionless form of eq. 4.1) is a function of impact velocity and reported values of α in the literature are listed in Table 4.1. Extrapolating the dependence of α on U_0 using data in Table 4.1, the estimated range of α is [10^{-5}, 10^{-4}] for $U_0 = [0.22, 0.92]$ m/s in the present work. ($\triangle {P^*}_H + \triangle {P^*}_D$) and $\triangle {P^*}_C$ is plotted using the respective equations given earlier as function of We for the surfaces with the following pitches, $p = 47$ μm ($p/D_0 = 0.028$), $p = 62$ μm (p/D_0 = 0.037) and $p = 76$ μm ($p/D_0 = 0.045$) in Figure 4.19(a), (b), and (c), respectively. The intersection of plots of ($\triangle {P^*}_H + \triangle {P^*}_D$) and $\triangle {P^*}_C$ is shown by a filled circle in Figure 4.19 (a-c) and it represents the theoretical estimate of We needed for the wetting transition. α = 7 $\times 10^{-5}$ is used as a fitting parameter in present calculations for $\triangle {P^*}_H$ in Figure 4.19 (a-c) and this value lies in the estimated range of α mentioned earlier. The measured minimum We for the CB and BDB are shown by green and blue vertical lines, respectively, in Figure 4.19 (a-c). Since the filled circle lies between the vertical lines for three cases of the pitch in Figure 4.19, the calculated values of the critical We are consistent with the measurements. These results show that the critical We required for the wetting transition inversely scales with the pitch.

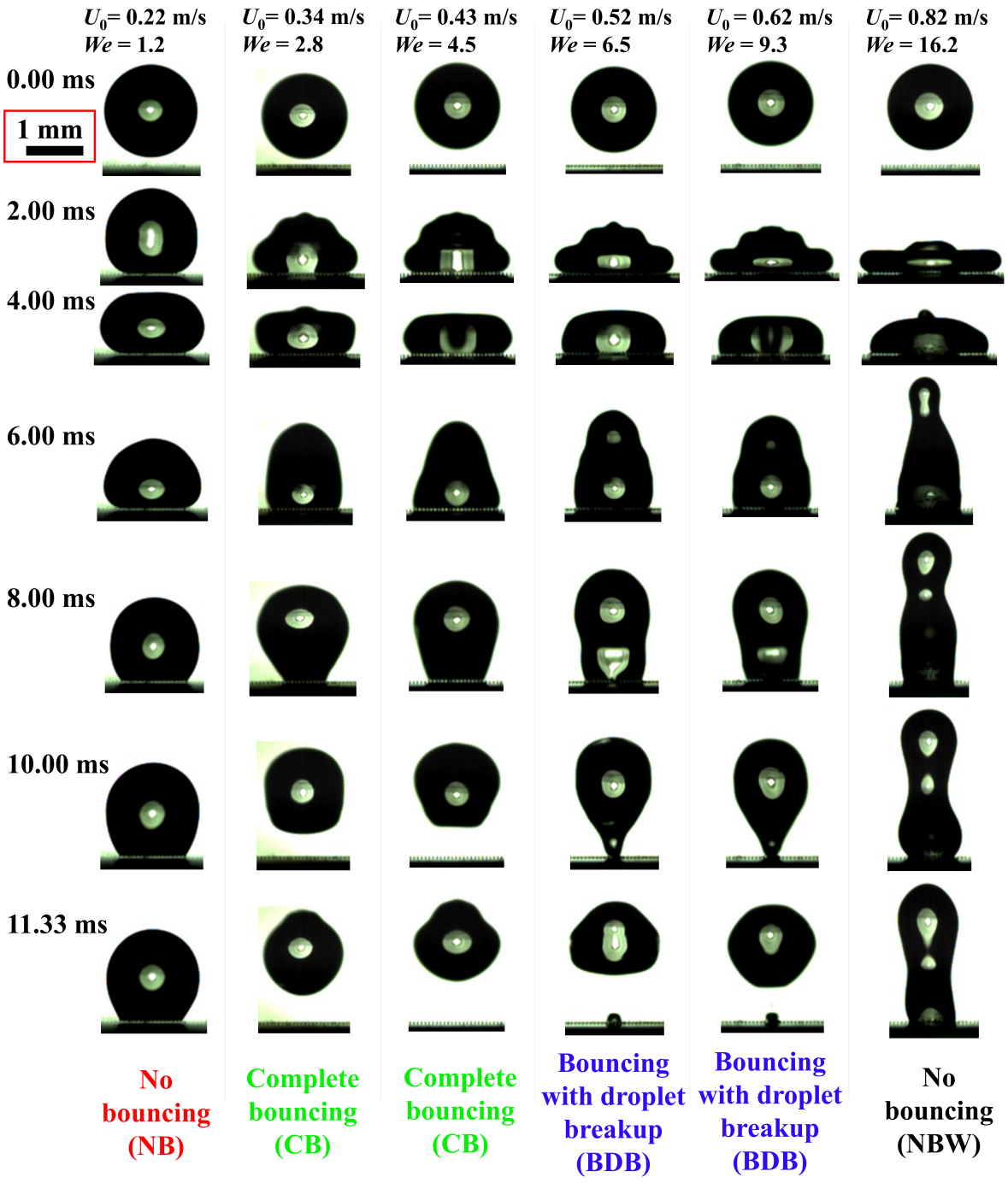

Figure 4.16: Image sequence obtained by high-speed visualization in transverse direction during impact of a microliter water droplet of 1.7 mm diameter on a microgrooved surface with $p = 76$ μm. Columns show different cases of Weber number (or impact velocity) and scale is shown on top-left.

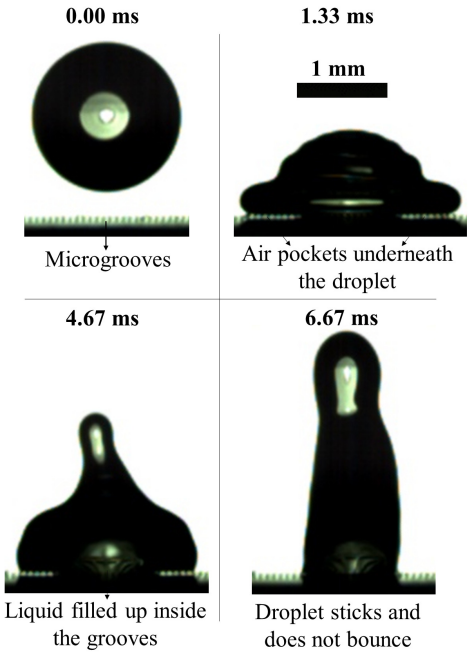

Figure 4.17: Image sequence obtained by high-speed visualization in transverse direction during impact on a microgrooved surface with pitch of 76 μm and at $We = 16.2$ ($U_0 = 0.82$ m/s). Images show the penetration of water into the microgrooves i.e. Cassie to Wenzel wetting transition (NBW).

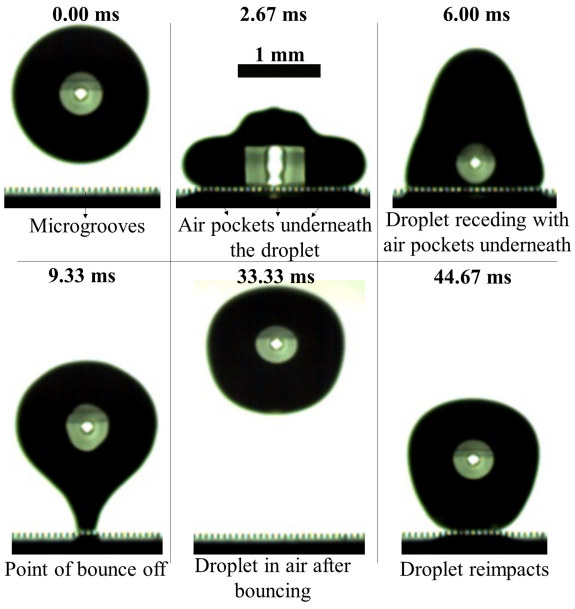

Figure 4.18: Image sequence obtained by high-speed visualization in transverse direction during impact on a microgrooved surface with pitch of 76 μm and at $We = 4.5$ ($U_0 = 0.43$ m/s). Images show the droplet bouncing off the surface (CB).

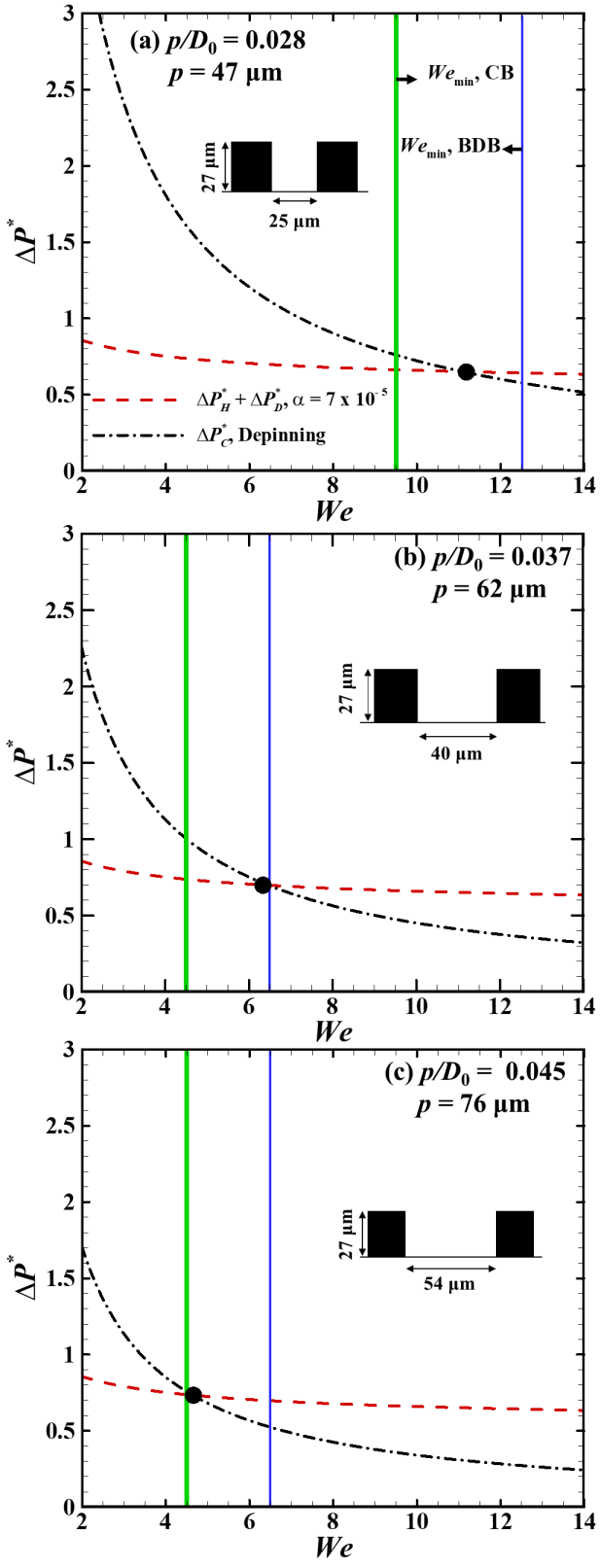

Figure 4.19: Estimation of theoretical critical Weber number (We) by eq. 4.8. The critical Weber number is represented by a filled circle. The minimum Weber numbers obtained in measurements for CB and BDB are shown by vertical lines. Three cases of the pitch are considered: (a) $p = 47$ μm, (b) $p = 62$ μm and (c) $p = 76$ μm.

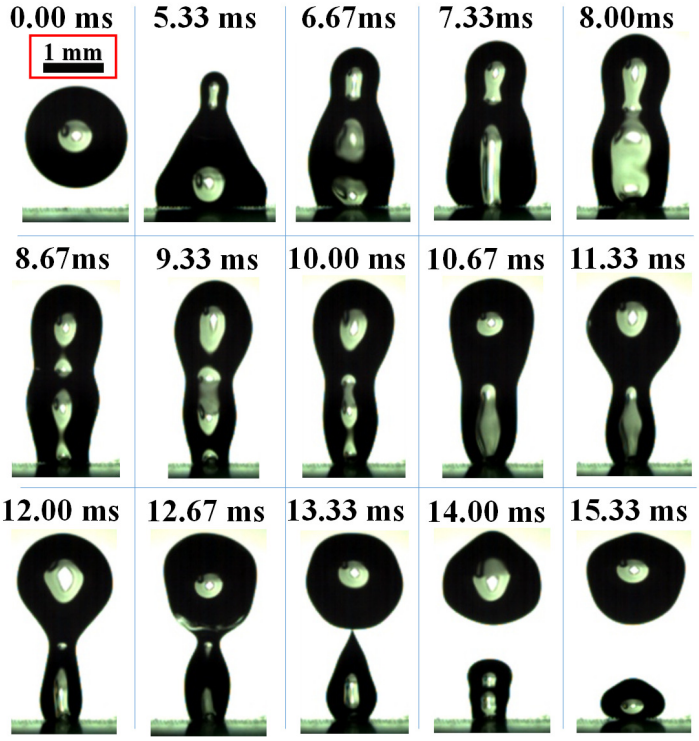

Figure 4.20: Image sequence obtained by high-speed visualization in transverse direction of impact of 1.7 mm diameter water droplet on a microgrooved surface with of pitch, $p = 62$ μm and at Weber number, $We = 16.2$ ($U_0 = 0.82$ m/s). Scale is shown on top-left.

4.6.2.3 Bouncing with droplet breakup

As discussed earlier in section, BDB occurs due to partial penetration of water in the microgrooves (Cassie to Wenzel wetting transition) at large pitch and large Weber number. Figure 4.20 shows time-varying droplet shapes on $p = 62$ μm surface ($p/D_0 = 0.037$) with $We = 16.2$ ($U_0 = 0.82$ m/s). The droplet spreads (0 ms to 5.33 ms), recedes (10 ms to 11.33 ms) and capillary wave propagation on the liquid-gas interface is noted after 8.67 ms. Due to the penetration of water in the microgrooves, the droplet sticks to the base surface and capillary wave propagation on the liquid-gas interface causes necking of the interface (8 ms to 12.67 ms). This results in the breakup of the droplet at 13.33 ms. We further quantify volume of daughter droplet left on the surface (V) from the recorded images. An axisymmetric droplet is assumed in the image in order to calculate volume. The percentage of V with respect to initial droplet volume is plotted in Figure 4.21 on Weber number (We) - dimensionless pitch (p/D_0) plane for the BDB ($V = 0$ for NB, CB and NBW). The contour plot shows that the maximum V % corresponds to $p/D_0 = 0.037$ surface at $We = 16.2$. Therefore, there exists an optimal pitch as well as Weber number for achieving the maximum V.

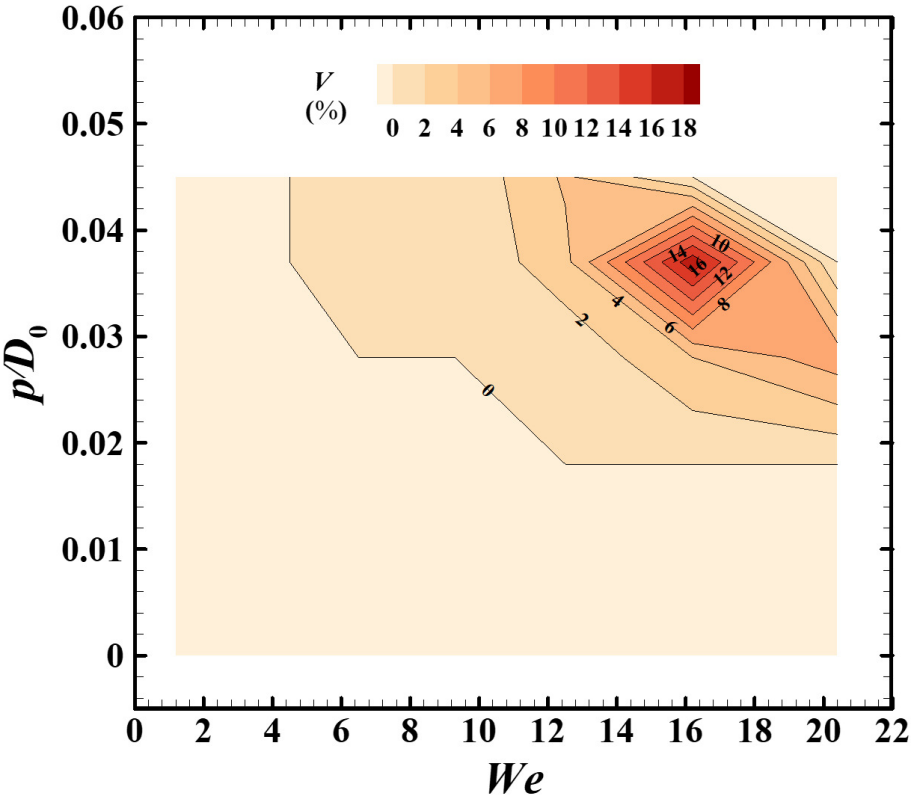

Figure 4.21: Contour of volume of daughter droplet left on the surface after droplet bouncing and breakup (BDB) on $We - p/D_0$ plane.

4.6.3 Regime map

A regime map is proposed using present measurements for different impact outcomes. Figure 4.22 shows the outcomes, namely, NB, CB, BDB, and NBW, on Weber number (We) - dimensionless pitch (p/D_0) plane. Figure 4.22 shows NB is observed in all cases of We at $p/D_0 = 0.018$ ($p = 30$ μm). As We increases at $p/D_0 = 0.028$ ($p = 47$ μm), the outcome changes from NB to CB and CB to BDB. Similarly, at $p/D_0 = 0.037$ ($p = 62$ μm) and $p/D_0 = 0.045$ ($p = 76$ μm), the outcome changes from NB to CB, CB to BDB and BDB to NBW. Therefore, there exists a critical We at a constant pitch or a critical pitch at a constant We for change from one regime to other. The critical We is the lowest for NB to CB at a given pitch. At larger We, CB to BDB and BDB to NBW occurs due to Cassie to Wenzel wetting transition, as explained in section 2.6.2.2.

In order to characterize the intensity of the bouncing, coefficient of restitution (ε) for CB or BDB cases is estimated. In this context, Richard and Quéré [53] plotted coefficient of restitution for the bouncing droplets on non-textured superhydrophobic surfaces. It is defined as $\varepsilon = U/U_0$, where U and U_0 are velocity of the droplet just after bouncing and impact velocity, respectively. U is estimated as $\sqrt{(2gh)}$, where h is the maximum height of the center of gravity of the droplet achieved after the bouncing. In BDB cases, h is measured after neglecting the daughter droplet that remains on the surface. The contours of ε

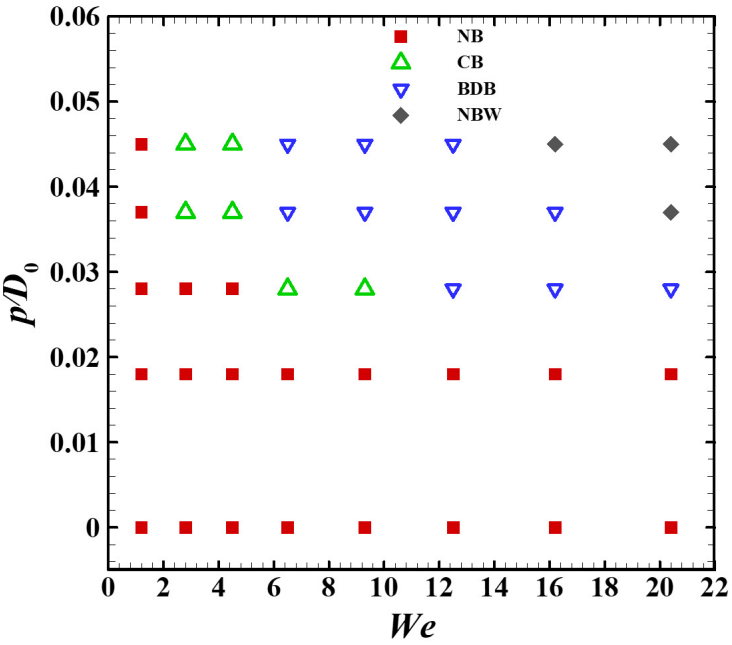

Figure 4.22: Regime map on Weber number (We) – dimensionless pitch (p/D_0) plane for different impact outcomes obtained in the present study for 1.7 mm water droplet. The outcomes are no bouncing (NB), complete bouncing (CB), bouncing with droplet breakup (BDB) and no bouncing due to Cassie to Wenzel wetting transition (NBW).

on We - (p/D_0) plane are plotted in Figure 4.23, that shows ε is the maximum for the CB cases at the largest pitch ($p/D_0 = 0.045$) and at $We = [2.8 - 4.5]$. Further increase in We at this pitch results in the penetration of liquid into the microgrooves and the outcome is BDB that lowers ε, as plotted in Figure 4.23. At $We = [2.8 - 4.5]$, ε slightly decreases on $p/D_0 = 0.037$ surface in comparison to $p/D_0 = 0.045$ surface due to slightly larger surface wettability of the former than the latter (Figure 4.6(a, b)). At $p/D_0 = 0.028$, the droplet bouncing is first observed at $We = 6.5$ with lower ε (~ 0.3) because it has larger wettability in comparison to surfaces with $p/D_0 = 0.037$ and $p/D_0 = 0.045$. In addition, the droplet experiences more number of ridges beneath it for $p/D_0 = 0.028$, which leads to more dissipation of the kinetic energy (which lowers ε) due to pinning and depinning of advancing or receding contact line [155]. Therefore, the coefficient of restitution is the largest for CB at the largest pitch considered and at an optimal Weber number.

4.6.4 Comparison with results on micropillared surfaces

The present results on the microgrooved surfaces are compared with previous results on micropillared surfaces [24]. The height and width of the pillar in Ref. [24] is almost equal to that of the ridge in the present study (within ± 2 μm). As explained in section 2.6.1, the spreading on the microgrooved surface is more in longitudinal direction than in transverse direction to the grooves. However, the spreading is isotropic on micropillared surfaces [24].

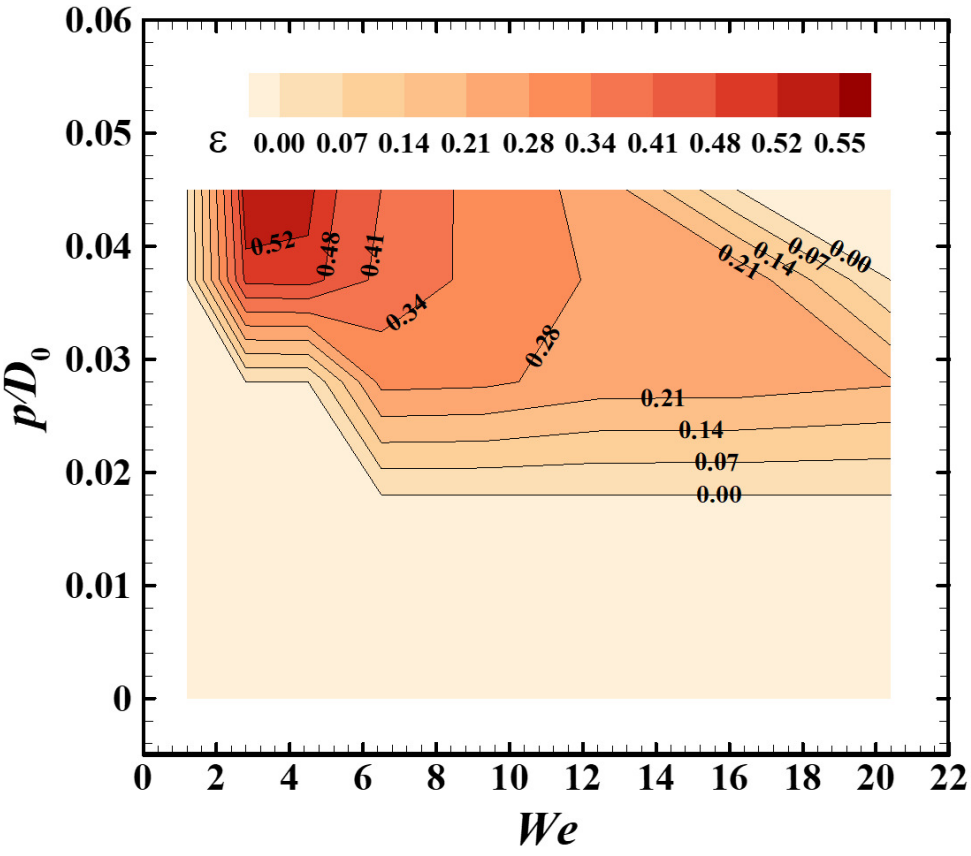

Figure 4.23: Contour of coefficient of restitution for CB and BDB on We - p/D_0 plane.

Further, the minimum Weber number (We_{min}) required for regimes; CB, BDB and NBW, as function of dimensionless pitch (p/D_0), are compared in Figure 4.25 (a), (b) and (c), respectively. Comparisons show that We_{min} for CB, BDB and NBW is larger for the microgrooved surface as compared to the micropillared surface at a given pitch. This is explained by the pinning and depinning of the contact line at edge of the ridge during spreading that dissipates larger kinetic energy in the former. Therefore, a larger Weber number is required to achieve CB, BDB and NBW on the microgrooved surface. Regarding comparison between water repelling properties of the two surfaces, the microgrooved surface is a better choice at larger pitch since Weber number (or impact velocity) required to achieve NBW is larger. Similarly, the micropillared surfaces perform well at lower pitch because the Weber number required to achieve CB is lower.

4.7 Closure

We investigate impact dynamics of a microliter water droplet (1.7 mm diameter) on a hydrophobic microgrooved surface, manufactured using photolithography. Time-varying droplet shapes are obtained in longitudinal and transverse direction to the grooves using high-speed visualization. The range of impact velocity and pitch of the microgrooves are $U_0 =$

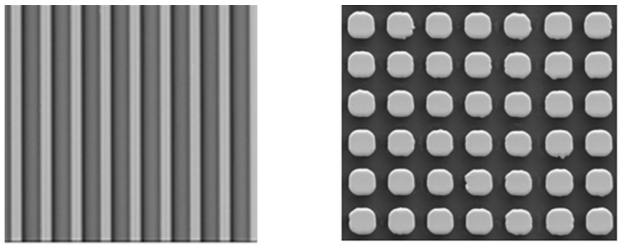

Microgrooved surface (Present work) **Micropillared surface (Patil et al., 2016)**

Figure 4.24: The results on the microgrooved surface of the present work and the micropillared surface of Patil et al. [24] work are compared.

[0.22, 0.92] m/s and $p = [30, 76]$ μm, respectively. The corresponding range of Reynolds number, Weber number and dimensionless pitch are $Re = [429, 1794]$, $We = [1.2, 20.4]$ and $p/D_0 = [0, 0.045]$, respectively. The surfaces exhibit anisotropic wetting characteristic and measured advancing, receding, and equilibrium contact angles are around 20 percent larger in the transverse direction. The droplet spreads more in longitudinal direction and this preferential spreading at low We inversely scales with the pitch. The largest percentage increase in the maximum wetted diameter in the longitudinal direction with respect to that in the transverse direction is around 80% at $We = 1.2$ at $p/D_0 = 0.018$.

The following regimes are obtained with increasing pitch at constant Weber number or with increasing Weber number at constant pitch: no bouncing (NB) $\rightarrow$ complete bouncing (CB) $\rightarrow$ bouncing with droplet breakup (BDB) $\rightarrow$ no bouncing due to Cassie to Wenzel wetting transition (NBW). BDB and NBW occur due to partial and full penetration of water into the microgrooves during Cassie to Wenzel wetting transition, respectively. The maximum volume of daughter droplet left on the surface after the droplet breakup for BDB corresponds to an optimal pitch and We. The critical We needed for the wetting transition inversely scales with the pitch and the depinning mechanism of the contact line at the edge of the pillars is found to be the possible mechanism for the wetting transition. Microgrooved surfaces exhibit better water repelling properties when the results are compared with the micropillared surface at larger pitch since the minimum We required to achieve CB, BDB, and NBW at a given pitch is larger for the microgrooved surfaces.

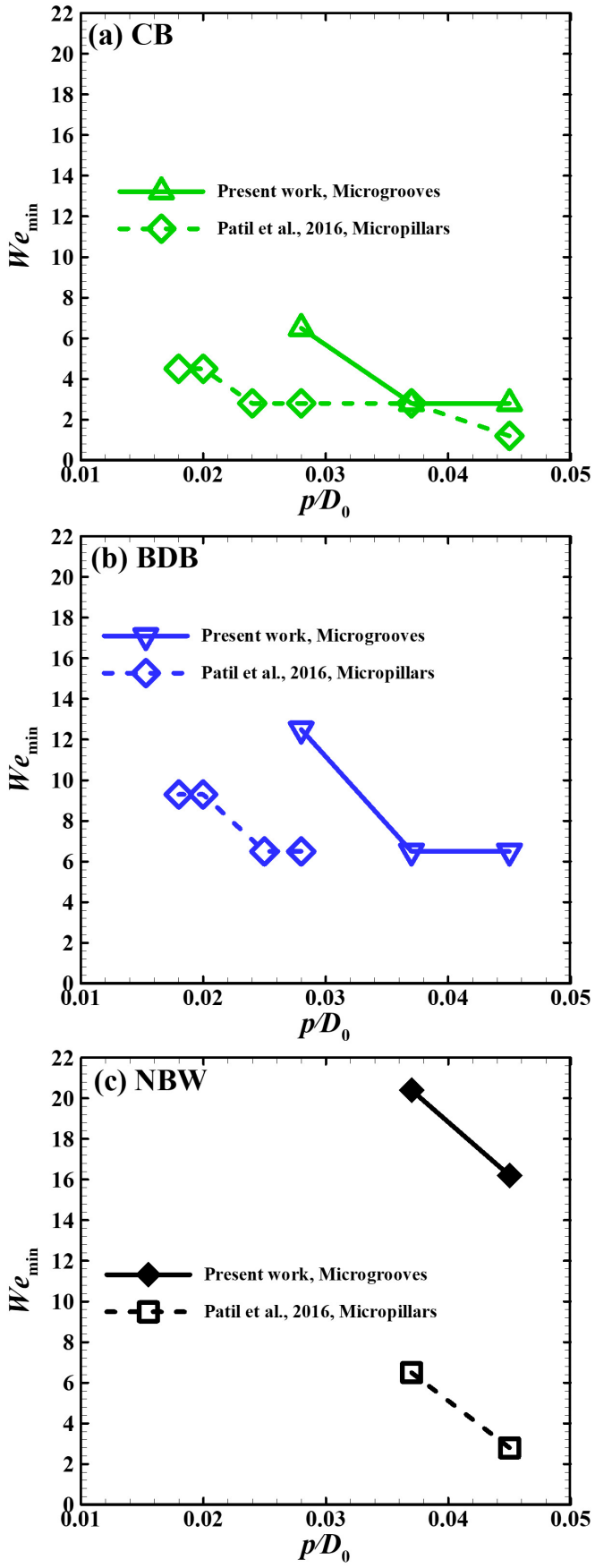

Figure 4.25: Comparison between We_{min} required for different outcomes, CB (a), BDB (b), and NBW (c) on microgrooved and micropillared surfaces for different cases of pitch.

Chapter 5

Conclusions and Future Scope of Work

5.1 Conclusions

5.1.1 Evaporation of a sessile droplet suspended with colloidal particles

In this field, the ring-like deposits obtained after the evaporation of a sessile water droplet containing polystyrene colloidal particles on a glass substrate is studied. On a non-heated substrate, the coupled effect of the particle size (d) and particles concentration (c) on ring dimensions and morphology are investigated. The range of d and c in the experiments are [0.1, 3] μm and [0.001, 1] %v/v, respectively. The measured ring profiles resemble a partial torus-like shape for all cases of d and c. Cracks are visualized on the surface of the ring for $d = 0.1$ μm and $c = 0.1$, and 1.0 %. Cracks are formed because at the final drying stage of the droplet when the receding liquid tries to shrink the ring whereas the pinned particles obstruct such shrinkage. This results in stress inside the deposit and consequently induces cracks. Three types of deposits are classified on particles concentration - particle size plane, namely, discontinuous monolayer ring, continuous monolayer ring, and multiple layers ring. In the case of multiple layers, the ring width and height increases with an increase in particles concentration and relative mass of the particles accumulated in the ring is the largest at the lowest particle size.

The monolayer ring forms due to larger immersion capillary forces among the particles at larger particle size and measured particle motion near the contact line qualitatively confirm the interaction among the particles. A critical particle concentration exists at a given particle size to achieve its formation. The measured dimensions of the ring scale with particles concentration by a power law and in general, the scaling agrees with the predictions of the model. The time-varying ring dimensions comparison with the model shows that a growing ring spreads in the last stage of drying at the expense of its height due to its interaction with shrinking free surface. On a non-heated substrate, evaporation of water droplet containing graphene nanoplatelets is also investigated by varying the graphene

nanoplatelets concentration from [0.01 - 0.1] %v/v. The graphene nanoplatelets are having 2D flakes type structure that remain on the substrate as a coating and thus less ring heights are observed, contrary to the ring heights obtained from polystyrene particles that remain on the substrate as a monolayer or multiple layers.

Then, the colloidal deposit formation on a nonuniform heated glass substrate is studied. The effect of the temperature gradient ($\mathrm{d}T/\mathrm{d}X$) and particles size on the deposit pattern and ring dimensions are investigated. The following temperature gradients were imposed across the substrate - $\mathrm{d}T/\mathrm{d}X = 1.7$, 2.8, and 4.2°C/mm, and the particles diameter considered were as follows - $d = 0.1$, 1.1, and 3.0 μm. The time-varying droplet shapes from the side and the temperature of the liquid-gas interface from the top were recorded using high-speed visualization and infrared thermography, respectively. The dried patterns were visualized under an optical microscope and quantified using an optical profilometer. The ring dimensions are smaller and larger on higher temperature side (T_H) for a smaller particle ($d = 0.1$ μm), and the larger particles ($d = 1.1$ and 3.0 μm), respectively. The displacement of the contact line on the T_H and lower temperature side (T_L) reveals that at d = 0.1 μm, the contact line depins early from the T_H side leading to the stick-slip motion of the contact line and twin asymmetric Marangoni recirculations advect more particles towards the T_L side. At $d = 1.1$, and 3.0 μm, the contact line remains pinned on both the sides for a maximum duration of evaporation. The pinned contact line and the twin asymmetric Marangoni recirculations aid in trapping the particles in the larger stagnation region on the T_H side contact line. Consequently, the ring width is larger on the T_H side in this case. The variation of the temperature gradient across the substrate shows that the ring width significantly increases or decreases on T_H or T_L side, depending on the particle size. This can be attributed to a stronger Marangoni recirculation as the temperature gradient increases.

A mechanistic model is utilized to understand the role of particle size in pinning or depinning of the contact line. It was found that the depinning in case of the smaller particles occurs because the surface tension force on the particles stacked near the contact line overcomes the drag and friction force on them. Finally, a regime map to classify the deposition patterns on a temperature gradient - particles size plane is proposed. Three regimes of deposit pattern are proposed. The first regime is uniform ring width i.e. well-documented coffee-ring effect, corresponds to uniformly non-heated or uniformly heated substrate. The second regime is thicker ring on lower temperature side, explained by asymmetric, twin Marangoni recirculations inside the evaporating droplet and contact line depinning in the presence of the smaller particles. The last and third regime is thicker ring on higher temperature side, attributed to the twin Marangoni recirculation and the contact line pinning with the bigger particles. These results of the evaporation of sessile droplet aid in understanding of the ring formation process and will be useful in guiding the design of self assemblies of the colloidal particles formed by the evaporating droplets. The study

provides fundamental insights into the dependence of the ring profile and dimensions on particle size, particles concentration, and uniform/nonuniform heating of the substrate. The present results will help to design technical applications such as inkjet-printing and manufacturing of bioassays.

5.1.2 Impact dynamics of a pure water droplet

In this field, the impact dynamics of microliter water droplet on a hydrophobic microgrooved surface is studied. The microgrooved surface was manufactured using photolithography. High-speed visualization technique was utilized to record time-varying droplet shapes in longitudinal and transverse direction to the grooves. The range of Reynolds number, Weber number and dimensionless pitch studied are $Re = [429, 1794]$, $We = [1.2, 20.4]$ and $p/D_0 = [0, 0.045]$, respectively. The surfaces exhibit anisotropic wetting characteristic and the droplet spreads more in longitudinal direction and this preferential spreading at low We inversely scales with the pitch.

The following regimes are obtained with increasing pitch at constant Weber number or with increasing Weber number at constant pitch: no bouncing (NB) → complete bouncing (CB) → bouncing with droplet breakup (BDB) → no bouncing due to Cassie to Wenzel wetting transition (NBW). A regime map is proposed on Weber number (We)-dimensionless pitch (p/D_0) plane for demarcations of the impact outcomes. BDB and NBW occur due to partial and full penetration of water into the microgrooves during Cassie to Wenzel wetting transition, respectively. The volume of daughter droplet left on the surface after the droplet breakup for BDB is quantified and the maximum volume corresponds to an optimal pitch and We. The coefficient of restitution for CB and BDB cases is plotted on We - p/D_0 plane and the largest coefficient corresponds to the largest pitch and optimal We for CB.

The measured critical We needed for the wetting transition is compared with an existing mathematical model, based on the balance of capillary pressure, dynamic pressure and water hammer pressure on the liquid-gas interface across the groove. The comparisons are good in all cases of pitch and results suggest that the critical We inversely scales with the pitch. The depinning of the contact line is found to be the possible mechanism for the wetting transition in the present measurements. Comparison between results on microgrooved and micropillared surfaces show that the minimum We required to achieve CB, BDB, and NBW at a given pitch is larger for the former. Hence, the former exhibit better water repelling properties than the latter at larger pitch while the latter is a better choice at lower pitch. The present results provide fundamental insights into droplet impact dynamics on microgrooved surfaces that may help to design technical applications such as self-cleaning and low-drag textured surfaces.

5.2 Scope for future work

1. In droplet impact dynamics, different grooves/pillar geometries can be manufactured using lithography. The height of the pillars can also be given a gradient. Various aspect ratios and different configurations of grooves and pillars can be used to study the bouncing and non-bouncing characteristics of the droplets, which will aid in manufacturing low drag and self-cleaning surfaces.

2. In evaporation of sessile droplet field, the effect of addition of surfactant to the water droplet on a nonuniform heated substrate case can be studied. The orientation of the temperature gradient can also be modified to obtain different Marangoni recirculations inside the droplet. For example, alternate heated and cooled Peltier coolers can be placed underneath the droplet along the perimeter of the contact line. Or a heated Peltier underneath the droplet can be placed as a single point source of heating to get a radial temperature gradient on the substrate.

3. Other aspects in the interfacial transport phenomena field are the droplet formation at T-junction channel and collision of droplets in various atmospheres, which can be explored in a combined manner.

Bibliography

[1] David Quéré. Wetting and roughness. *Annu. Rev. Mater. Res.*, 38:71–99, 2008.

[2] P Wagner, R Fürstner, Wilhelm Barthlott, and Christoph Neinhuis. Quantitative assessment to the structural basis of water repellency in natural and technical surfaces. *Journal of Experimental Botany*, 54(385):1295–1303, 2003.

[3] Nagesh Devidasrao Patil. *Impact and evaportaion dynamics of droplets on surfaces with different wettability: experimental and numerical study*. PhD thesis, Indian Institute of Technology Bombay, 2017.

[4] Sun Choi, Stefano Stassi, Albert P Pisano, and Tarek I Zohdi. Coffee-ring effect-based three dimensional patterning of micro/nanoparticle assembly with a single droplet. *Langmuir*, 26(14):11690–11698, 2010.

[5] Vadim Bromberg, Siyuan Ma, and Timothy J Singler. High-resolution inkjet printing of electrically conducting lines of silver nanoparticles by edge-enhanced twin-line deposition. *Applied Physics Letters*, 102(21):214101, 2013.

[6] Benjamin Sobac and David Brutin. Desiccation of a sessile drop of blood: Cracks, folds formation and delamination. *Colloids and Surfaces A: Physicochemical and Engineering Aspects*, 448:34–44, 2014.

[7] Nagesh D Patil, Rajneesh Bhardwaj, and Atul Sharma. Self-sorting of bi-dispersed colloidal particles near contact line of an evaporating sessile droplet. *Langmuir*, 2018.

[8] Rajneesh Bhardwaj, Xiaohua Fang, Ponisseril Somasundaran, and Daniel Attinger. Self-assembly of colloidal particles from evaporating droplets: role of dlvo interactions and proposition of a phase diagram. *Langmuir*, 26(11):7833–7842, 2010.

[9] Yanshen Li, Cunjing Lv, Zhaohan Li, David Quéré, and Quanshui Zheng. From coffee rings to coffee eyes. *Soft Matter*, 11(23):4669–4673, 2015.

[10] Christophe Clanet, Cédric Béguin, Denis Richard, and David Quéré. Maximal deformation of an impacting drop. *Journal of Fluid Mechanics*, 517:199–208, 2004.

[11] Rajneesh Bhardwaj and Daniel Attinger. Non-isothermal wetting during impact of millimeter-size water drop on a flat substrate: Numerical investigation and comparison with high-speed visualization experiments. *International Journal of Heat and Fluid Flow*, 29(5):1422–1435, 2008.

[12] Ilker S Bayer and Constantine M Megaridis. Contact angle dynamics in droplets impacting on flat surfaces with different wetting characteristics. *Journal of Fluid Mechanics*, 558:415–449, 2006.

[13] Rajneesh Bhardwaj, Jon P Longtin, and Daniel Attinger. Interfacial temperature measurements, high-speed visualization and finite-element simulations of droplet impact and evaporation on a solid surface. *International Journal of Heat and Mass Transfer*, 53(19-20):3733–3744, 2010.

[14] M Reyssat, A Pépin, F Marty, Y Chen, and D Quéré. Bouncing transitions on microtextured materials. *EPL (Europhysics Letters)*, 74(2):306, 2006.

[15] Yahua Liu, Lisa Moevius, Xinpeng Xu, Tiezheng Qian, Julia M Yeomans, and Zuankai Wang. Pancake bouncing on superhydrophobic surfaces. *Nature Physics*, 10(7):515, 2014.

[16] Yan Zhao, Qinghua Lu, Mei Li, and Xin Li. Anisotropic wetting characteristics on submicrometer-scale periodic grooved surface. *Langmuir*, 23(11):6212–6217, 2007.

[17] Susmita Dash, Marie T Alt, and Suresh V Garimella. Hybrid surface design for robust superhydrophobicity. *Langmuir*, 28(25):9606–9615, 2012.

[18] Tingyi Liu and Chang-Jin Kim. Turning a surface superrepellent even to completely wetting liquids. *Science*, 346:1096–1100, 2014.

[19] Jean Berthier. *Micro-drops and digital microfluidics*. William Andrew, 2012.

[20] Nagesh D Patil, Prathamesh G Bange, Rajneesh Bhardwaj, and Atul Sharma. Effects of substrate heating and wettability on evaporation dynamics and deposition patterns for a sessile water droplet containing colloidal particles. *Langmuir*, 32(45):11958–11972, 2016.

[21] Ying-Song Yu, Ming-Chao Wang, and Xianfu Huang. Evaporative deposition of polystyrene microparticles on pdms surface. *Scientific reports*, 7(1):14118, 2017.

[22] Athanasios Milionis, Ilker S Bayer, Despina Fragouli, Fernando Brandi, and Athanassia Athanassiou. Combination of lithography and coating methods for surface wetting control. In *Updates in Advanced Lithography*. InTech, 2013.

[23] Stefano Schiaffino and Ain A Sonin. Molten droplet deposition and solidification at low weber numbers. *Physics of Fluids*, 9(11):3172–3187, 1997.

[24] Nagesh D Patil, Rajneesh Bhardwaj, and Atul Sharma. Droplet impact dynamics on micropillared hydrophobic surfaces. *Experimental Thermal and Fluid Science*, 74:195–206, 2016.

[25] Jungho Park and Jooho Moon. Control of colloidal particle deposit patterns within picoliter droplets ejected by ink-jet printing. *Langmuir*, 22(8):3506–3513, 2006.

[26] Michael Layani, Michael Gruchko, Oded Milo, Isaac Balberg, Doron Azulay, and Shlomo Magdassi. Transparent conductive coatings by printing coffee ring arrays obtained at room temperature. *ACS nano*, 3(11):3537–3542, 2009.

[27] Ethan B Secor, Pradyumna L Prabhumirashi, Kanan Puntambekar, Michael L Geier, and Mark C Hersam. Inkjet printing of high conductivity, flexible graphene patterns. *The journal of physical chemistry letters*, 4(8):1347–1351, 2013.

[28] Haena Kim, Jeong In Jang, Hyun Ho Kim, Geon-Woong Lee, Jung Ah Lim, Joong Tark Han, and Kilwon Cho. Sheet size-induced evaporation behaviors of inkjet-printed graphene oxide for printed electronics. *ACS applied materials & interfaces*, 8(5):3193–3199, 2016.

[29] Lei Zhang, Hongtao Liu, Yan Zhao, Xiangnan Sun, Yugeng Wen, Yunlong Guo, Xike Gao, Chong-an Di, Gui Yu, and Yunqi Liu. Inkjet printing high-resolution, large-area graphene patterns by coffee-ring lithography. *Advanced Materials*, 24(3):436–440, 2012.

[30] Vincent Dugas, Jérôme Broutin, and Eliane Souteyrand. Droplet evaporation study applied to dna chip manufacturing. *Langmuir*, 21(20):9130–9136, 2005.

[31] Jessica T Wen, Chih-Ming Ho, and Peter B Lillehoj. Coffee ring aptasensor for rapid protein detection. *Langmuir*, 29(26):8440–8446, 2013.

[32] Rajneesh Bhardwaj, Xiaohua Fang, and Daniel Attinger. Pattern formation during the evaporation of a colloidal nanoliter drop: a numerical and experimental study. *New Journal of Physics*, 11(7):075020, 2009.

[33] Jun Fukai, Z Zhao, Dimos Poulikakos, Constantine M Megaridis, and O Miyatake. Modeling of the deformation of a liquid droplet impinging upon a flat surface. *Physics of Fluids A: Fluid Dynamics*, 5(11):2588–2599, 1993.

[34] Pierre-Gilles de Gennes, Francoise Brochard-Wyart, and David Quere. Capillarity and wetting phenomenon, 2003.

[35] Gregory D Bixler and Bharat Bhushan. Rice-and butterfly-wing effect inspired self-cleaning and low drag micro/nanopatterned surfaces in water, oil, and air flow. *Nanoscale*, 6(1):76–96, 2014.

[36] Christophe Frankiewicz and Daniel Attinger. Texture and wettability of metallic lotus leaves. *Nanoscale*, 8(7):3982–3990, 2016.

[37] Robert D Deegan, Olgica Bakajin, Todd F Dupont, Greb Huber, Sidney R Nagel, and Thomas A Witten. Capillary flow as the cause of ring stains from dried liquid drops. *Nature*, 389(6653):827, 1997.

[38] Hua Hu and Ronald G Larson. Evaporation of a sessile droplet on a substrate. *The Journal of Physical Chemistry B*, 106(6):1334–1344, 2002.

[39] Ronald G Larson. In retrospect: Twenty years of drying droplets. *Nature*, 550(7677):466, 2017.

[40] Raymond E Goldstein. Coffee stains, cell receptors, and time crystals: Lessons from the old literature. *arXiv preprint arXiv:1811.08179*, 2018.

[41] Robert Brown. Xxiv. additional remarks on active molecules. *The Philosophical Magazine*, 6(33):161–166, 1829.

[42] Robert D Deegan. Pattern formation in drying drops. *Physical review E*, 61(1):475, 2000.

[43] Xiaoying Shen, Chih-Ming Ho, and Tak-Sing Wong. Minimal size of coffee ring structure. *The Journal of Physical Chemistry B*, 114(16):5269–5274, 2010.

[44] Dileep Mampallil and Huseyin Burak Eral. A review on suppression and utilization of the coffee-ring effect. *Advances in colloid and interface science*, 252:38–54, 2018.

[45] Maryam Parsa, Souad Harmand, and Khellil Sefiane. Mechanisms of pattern formation from dried sessile drops. *Advances in colloid and interface science*, 254:22–47, 2018.

[46] Hua Hu and Ronald G Larson. Marangoni effect reverses coffee-ring depositions. *The Journal of Physical Chemistry B*, 110(14):7090–7094, 2006.

[47] Yueh-Feng Li, Yu-Jane Sheng, and Heng-Kwong Tsao. Evaporation stains: suppressing the coffee-ring effect by contact angle hysteresis. *Langmuir*, 29(25):7802–7811, 2013.

[48] Tuan AH Nguyen, Marc A Hampton, and Anh V Nguyen. Evaporation of nanoparticle droplets on smooth hydrophobic surfaces: the inner coffee ring deposits. *The Journal of Physical Chemistry C*, 117(9):4707–4716, 2013.

[49] Maryam Parsa, Souad Harmand, Khellil Sefiane, Maxence Bigerelle, and Raphael Deltombe. Effect of substrate temperature on pattern formation of nanoparticles from volatile drops. *Langmuir*, 31(11):3354–3367, 2015.

[50] S Chandra and CT Avedisian. On the collision of a droplet with a solid surface. *Proc. R. Soc. Lond. A*, 432(1884):13–41, 1991.

[51] Ted Mao, David CS Kuhn, and Honghi Tran. Spread and rebound of liquid droplets upon impact on flat surfaces. *AIChE Journal*, 43(9):2169–2179, 1997.

[52] Prathamesh G Bange and Rajneesh Bhardwaj. Computational study of bouncing and non-bouncing droplets impacting on superhydrophobic surfaces. *Theoretical and Computational Fluid Dynamics*, 30(3):211–235, 2016.

[53] D Richard and D Quéré. Bouncing water drops. *Europhysics Letters (EPL)*, 50(6):769–775, 2000.

[54] Z Zhao, D Poulikakos, and J Fukai. Heat transfer and fluid dynamics during the collision of a liquid droplet on a substrate—ii. experiments. *International journal of heat and mass transfer*, 39(13):2791–2802, 1996.

[55] Nagesh D Patil, Vinesh H Gada, Atul Sharma, and Rajneesh Bhardwaj. On dual-grid level-set method for contact line modeling during impact of a droplet on hydrophobic and superhydrophobic surfaces. *International Journal of Multiphase Flow*, 81:54–66, 2016.

[56] Martin Rein. *Drop-surface interactions*, volume 456. Springer, 2014.

[57] M Pasandideh-Fard, YM Qiao, Sanjeev Chandra, and Javad Mostaghimi. Capillary effects during droplet impact on a solid surface. *Physics of fluids*, 8(3):650–659, 1996.

[58] JM Waldvogel and D Poulikakos. Solidification phenomena in picoliter size solder droplet deposition on a composite substrate. *International Journal of Heat and Mass Transfer*, 40(2):295–309, 1997.

[59] Daniel Attinger, Z Zhao, and D Poulikakos. An experimental study of molten microdroplet surface deposition and solidification: transient behavior and wetting angle dynamics. *Journal of Heat Transfer*, 122(3):544–556, 2000.

[60] ABD Cassie and S Baxter. Wettability of porous surfaces. *Transactions of the Faraday society*, 40:546–551, 1944.

[61] Robert N Wenzel. Resistance of solid surfaces to wetting by water. *Industrial & Engineering Chemistry*, 28(8):988–994, 1936.

[62] Alexander F Routh. Drying of thin colloidal films. *Reports on Progress in Physics*, 76(4):046603, 2013.

[63] Peter J Yunker, Tim Still, Matthew A Lohr, and AG Yodh. Suppression of the coffee-ring effect by shape-dependent capillary interactions. *Nature*, 476(7360):308, 2011.

[64] H Burak Eral, D Mampallil Augustine, Michael HG Duits, and Frieder Mugele. Suppressing the coffee stain effect: how to control colloidal self-assembly in evaporating drops using electrowetting. *Soft Matter*, 7(10):4954–4958, 2011.

[65] Daniel Orejon, Khellil Sefiane, and Martin ER Shanahan. Evaporation of nanofluid droplets with applied dc potential. *Journal of colloid and interface science*, 407:29–38, 2013.

[66] Terry P Bigioni, Xiao-Min Lin, Toan T Nguyen, Eric I Corwin, Thomas A Witten, and Heinrich M Jaeger. Kinetically driven self assembly of highly ordered nanoparticle monolayers. *Nature materials*, 5(4):265, 2006.

[67] Jun Wu, Jun Xia, Wei Lei, and Bao-ping Wang. Generation of the smallest coffee-ring structures by solute crystallization reaction on a hydrophobic surface. *RSC Advances*, 3(16):5328–5331, 2013.

[68] Siddharth Maheshwari, Lu Zhang, Yingxi Zhu, and Hsueh-Chia Chang. Coupling between precipitation and contact-line dynamics: Multiring stains and stick-slip motion. *Physical review letters*, 100(4):044503, 2008.

[69] Byung Mook Weon and Jung Ho Je. Fingering inside the coffee ring. *Physical Review E*, 87(1):013003, 2013.

[70] Hisay Lama, Madivala G Basavaraj, and Dillip K Satapathy. Tailoring crack morphology in coffee-ring deposits via substrate heating. *Soft matter*, 13(32):5445–5452, 2017.

[71] D Kaya, VA Belyi, and M Muthukumar. Pattern formation in drying droplets of polyelectrolyte and salt. *The Journal of chemical physics*, 133(11):114905, 2010.

[72] Chan Hee Chon, Sokwon Paik, Joseph B Tipton, and Kenneth D Kihm. Effect of nanoparticle sizes and number densities on the evaporation and dryout characteristics for strongly pinned nanofluid droplets. *Langmuir*, 23(6):2953–2960, 2007.

[73] Jolke Perelaer, Patrick J Smith, Chris E Hendriks, Antje MJ van den Berg, and Ulrich S Schubert. The preferential deposition of silica micro-particles at the boundary of inkjet printed droplets. *Soft Matter*, 4(5):1072–1078, 2008.

[74] Álvaro G Marín, Hanneke Gelderblom, Detlef Lohse, and Jacco H Snoeijer. Order-to-disorder transition in ring-shaped colloidal stains. *Physical review letters*, 107(8):085502, 2011.

[75] Byung Mook Weon and Jung Ho Je. Self-pinning by colloids confined at a contact line. *Physical review letters*, 110(2):028303, 2013.

[76] Xin Yang, Christopher Y Li, and Ying Sun. From multi-ring to spider web and radial spoke: competition between the receding contact line and particle deposition in a drying colloidal drop. *Soft matter*, 10(25):4458–4463, 2014.

[77] Seul-a Ryu, Jin Young Kim, So Youn Kim, and Byung Mook Weon. Drying-mediated patterns in colloid-polymer suspensions. *Scientific Reports*, 7(1):1079, 2017.

[78] Vignesh U Nayak and Narayan K Prabhu. Wetting behavior and heat transfer of aqueous graphene nanofluids. *Journal of Materials Engineering and Performance*, 25(4):1474–1480, 2016.

[79] Khellil Sefiane. On the formation of regular patterns from drying droplets and their potential use for bio-medical applications. *Journal of Bionic Engineering*, 7:S82–S93, 2010.

[80] Daniel Orejon, Khellil Sefiane, and Martin ER Shanahan. Stick–slip of evaporating droplets: substrate hydrophobicity and nanoparticle concentration. *Langmuir*, 27(21):12834–12843, 2011.

[81] David Brutin. Influence of relative humidity and nano-particle concentration on pattern formation and evaporation rate of pinned drying drops of nanofluids. *Colloids and Surfaces A: Physicochemical and Engineering Aspects*, 429:112–120, 2013.

[82] Tuan AH Nguyen, Anh V Nguyen, Marc A Hampton, Zhi Ping Xu, Longbin Huang, and Victor Rudolph. Theoretical and experimental analysis of droplet evaporation on solid surfaces. *Chemical engineering science*, 69(1):522–529, 2012.

[83] Hau Him Lee, Sau Chung Fu, Chi Yan Tso, and Christopher YH Chao. Study of residue patterns of aqueous nanofluid droplets with different particle sizes and concentrations on different substrates. *International Journal of Heat and Mass Transfer*, 105:230–236, 2017.

[84] F Sondej, M Peglow, A Bück, and E Tsotsas. Experimental investigation of the morphology of salt deposits from drying sessile droplets by white-light interferometry. *AIChE Journal*, 64(6):2002–2016, 2018.

[85] Xin Zhong and Fei Duan. Evaporation of sessile droplets affected by graphite nanoparticles and binary base fluids. *The Journal of Physical Chemistry B*, 118(47):13636–13645, 2014.

[86] Fen Fen Shao, Adrian Neild, and Tuck Wah Ng. Hydrophobicity effect in the self assembly of particles in an evaporating droplet. *Journal of Applied Physics*, 108(3):034512, 2010.

[87] L Pauchard, F Parisse, and C Allain. Influence of salt content on crack patterns formed through colloidal suspension desiccation. *Physical Review E*, 59(3):3737, 1999.

[88] David Brutin, Benjamin Sobac, and Céline Nicloux. Influence of substrate nature on the evaporation of a sessile drop of blood. *Journal of heat transfer*, 134(6), 2012.

[89] Florian Carle and David Brutin. How surface functional groups influence fracturation in nanofluid droplet dry-outs. *Langmuir*, 29(32):9962–9966, 2013.

[90] Yongjian Zhang, Yimeng Qian, Zhengtang Liu, Zhiguang Li, and Duyang Zang. Surface wrinkling and cracking dynamics in the drying of colloidal droplets. *The European Physical Journal E*, 37(9):84, 2014.

[91] Udita Uday Ghosh, Monojit Chakraborty, Aditya Bikram Bhandari, Suman Chakraborty, and Sunando DasGupta. Effect of surface wettability on crack dynamics and morphology of colloidal films. *Langmuir*, 31(22):6001–6010, 2015.

[92] Jin Young Kim, Kun Cho, Seul-a Ryu, So Youn Kim, and Byung Mook Weon. Crack formation and prevention in colloidal drops. *Scientific reports*, 5:13166, 2015.

[93] Venkateshwar Rao Dugyala, Hisay Lama, Dillip K Satapathy, and Madivala G Basavaraj. Role of particle shape anisotropy on crack formation in drying of colloidal suspension. *Scientific reports*, 6:30708, 2016.

[94] F Giorgiutti-Dauphiné and L Pauchard. Drying drops. *The European Physical Journal E*, 41(3):32, 2018.

[95] Byung Mook Weon and Jung Ho Je. Capillary force repels coffee-ring effect. *Physical Review E*, 82(1):015305, 2010.

[96] Peter A Kralchevsky and Kuniaki Nagayama. Capillary forces between colloidal particles. *Langmuir*, 10(1):23–36, 1994.

[97] Manish Kumar and Rajneesh Bhardwaj. A combined computational and experimental investigation on evaporation of a sessile water droplet on a heated hydrophilic substrate. *International Journal of Heat and Mass Transfer*, 122:1223–1238, 2018.

[98] Tohru Okuzono, Masaru Kobayashi, and Masao Doi. Final shape of a drying thin film. *Physical Review E*, 80(2):021603, 2009.

[99] Karnail B Singh and Mahesh S Tirumkudulu. Cracking in drying colloidal films. *Physical review letters*, 98(21):218302, 2007.

[100] Yuri O Popov. Evaporative deposition patterns: spatial dimensions of the deposit. *Physical Review E*, 71(3):036313, 2005.

[101] Robert D Deegan, Olgica Bakajin, Todd F Dupont, Greg Huber, Sidney R Nagel, and Thomas A Witten. Contact line deposits in an evaporating drop. *Physical review E*, 62(1):756, 2000.

[102] Khellil Sefiane. Patterns from drying drops. *Advances in colloid and interface science*, 206:372–381, 2014.

[103] Xin Zhong, Alexandru Crivoi, and Fei Duan. Sessile nanofluid droplet drying. *Advances in colloid and interface science*, 217:13–30, 2015.

[104] Ronald G Larson. Transport and deposition patterns in drying sessile droplets. *AIChE Journal*, 60(5):1538–1571, 2014.

[105] RH Farahi, A Passian, TL Ferrell, and T Thundat. Microfluidic manipulation via marangoni forces. *Applied physics letters*, 85(18):4237–4239, 2004.

[106] WD Ristenpart, PG Kim, C Domingues, J Wan, and Howard A Stone. Influence of substrate conductivity on circulation reversal in evaporating drops. *Physical review letters*, 99(23):234502, 2007.

[107] Xuefeng Xu, Jianbin Luo, and Dan Guo. Criterion for reversal of thermal marangoni flow in drying drops. *Langmuir*, 26(3):1918–1922, 2009.

[108] Anna Trybala, Adaora Okoye, Sergey Semenov, Hezekiah Agogo, Ramón G Rubio, Francisco Ortega, and Víctor M Starov. Evaporation kinetics of sessile droplets of aqueous suspensions of inorganic nanoparticles. *Journal of colloid and interface science*, 403:49–57, 2013.

[109] Fabien Girard, Mickael Antoni, and Khellil Sefiane. Infrared thermography investigation of an evaporating sessile water droplet on heated substrates. *Langmuir*, 26(7):4576–4580, 2010.

[110] Xin Zhong and Fei Duan. Disk to dual ring deposition transformation in evaporating nanofluid droplets from substrate cooling to heating. *Physical Chemistry Chemical Physics*, 18(30):20664–20671, 2016.

[111] Xin Zhong, Chenlong Wu, and Fei Duan. From enhancement to elimination of dual-ring pattern of nanoparticles from sessile droplets by heating the substrate. *Applied Thermal Engineering*, 115:1418–1423, 2017.

[112] Maryam Parsa, Souad Harmand, Khellil Sefiane, Maxence Bigerelle, and Raphael Deltombe. Effect of substrate temperature on pattern formation of bidispersed particles from volatile drops. *The Journal of Physical Chemistry B*, 121(48):11002–11017, 2017.

[113] JB Brzoska, F Brochard-Wyart, and F Rondelez. Motions of droplets on hydrophobic model surfaces induced by thermal gradients. *Langmuir*, 9(8):2220–2224, 1993.

[114] Yuan-Tai Tseng, Fan-Gang Tseng, Yu-Feng Chen, and Ching-Chang Chieng. Fundamental studies on micro-droplet movement by marangoni and capillary effects. *Sensors and Actuators A: Physical*, 114(2-3):292–301, 2004.

[115] Jian Z Chen, Sandra M Troian, Anton A Darhuber, and Sigurd Wagner. Effect of contact angle hysteresis on thermocapillary droplet actuation. *Journal of Applied Physics*, 97(1):014906, 2005.

[116] Huy-Bich Nguyen and Jyh-Chen Chen. A numerical study of thermocapillary migration of a small liquid droplet on a horizontal solid surface. *Physics of Fluids*, 22(6):062102, 2010.

[117] Huy-Bich Nguyen and Jyh-Chen Chen. Numerical study of a droplet migration induced by combined thermocapillary-buoyancy convection. *Physics of Fluids*, 22(12):122101, 2010.

[118] Chirodeep Bakli, Sree Hari PD, and Suman Chakraborty. Mimicking wettability alterations using temperature gradients for water nanodroplets. *Nanoscale*, 9(34):12509–12515, 2017.

[119] Masumeh Foroutan, S Mahmood Fatemi, Farshad Esmaeilian, Vahid Fadaei Naeini, and Majid Baniassadi. Contact angle hysteresis and motion behaviors of a water nano-droplet on suspended graphene under temperature gradient. *Physics of Fluids*, 30(5):052101, 2018.

[120] Safouene Ouenzerfi and Souad Harmand. Experimental droplet study of inverted marangoni effect of a binary liquid mixture on a nonuniform heated substrate. *Langmuir*, 32(10):2378–2388, 2016.

[121] Tapan Kumar Pradhan and Pradipta Kumar Panigrahi. Thermocapillary convection inside a stationary sessile water droplet on a horizontal surface with an imposed temperature gradient. *Experiments in Fluids*, 56(9):178, 2015.

[122] Alexandros Askounis, Yutaku Kita, Masamichi Kohno, Yasuyuki Takata, Vasileios Koutsos, and Khellil Sefiane. Influence of local heating on marangoni flows and evaporation kinetics of pure water drops. *Langmuir*, 33(23):5666–5674, 2017.

[123] Sigma Aldrich colloidal suspensions. https://www.sigmaaldrich.com/content/dam/sigma-aldrich/docs/Sigma/Product_Information_Sheet/2/lb11pis.pdf., 2019. [Online; accessed 22-September-2019].

[124] Armando Maestro, Eduardo Guzmán, Francisco Ortega, and Ramón G Rubio. Contact angle of micro-and nanoparticles at fluid interfaces. *Current opinion in colloid & interface science*, 19(4):355–367, 2014.

[125] A. Mohammadi. *Dynamics of colloidal inclusions in hydrogels*. PhD thesis, McGill University, 2011.

[126] Sigma Aldrich glass slides. https:/www.sigmaaldrich.com/catalog/product/sigma/s8902?lang=en&region=IN, 2019. [Online; accessed 22-September-2019].

[127] Viral H Chhasatia and Ying Sun. Interaction of bi-dispersed particles with contact line in an evaporating colloidal drop. *Soft Matter*, 7(21):10135–10143, 2011.

[128] Stefan Duhr and Dieter Braun. Why molecules move along a temperature gradient. *Proceedings of the National Academy of Sciences*, 103(52):19678–19682, 2006.

[129] Roberto Piazza and Alberto Parola. Thermophoresis in colloidal suspensions. *Journal of Physics: Condensed Matter*, 20(15):153102, 2008.

[130] Alois Würger. Thermal non-equilibrium transport in colloids. *Reports on Progress in Physics*, 73(12):126601, 2010.

[131] Marco Braibanti, Daniele Vigolo, and Roberto Piazza. Does thermophoretic mobility depend on particle size? *Physical review letters*, 100(10):108303, 2008.

[132] Jung-yeul Jung, Young Won Kim, Jung Yul Yoo, Junemo Koo, and Yong Tae Kang. Forces acting on a single particle in an evaporating sessile droplet on a hydrophilic surface. *Analytical chemistry*, 82(3):784–788, 2010.

[133] Tak-Sing Wong, Ting-Hsuan Chen, Xiaoying Shen, and Chih-Ming Ho. Nanochromatography driven by the coffee ring effect. *Analytical chemistry*, 83(6):1871–1873, 2011.

[134] Ying-Song Yu, Xue-Lian Xia, Xu Zheng, Xianfu Huang, and Jin-Zhi Zhou. Quasi-static motion of microparticles at the depinning contact line of an evaporating droplet on pdms surface. *SCIENCE CHINA Physics, Mechanics & Astronomy*, 60(9):094612, 2017.

[135] Menachem Elimelech, John Gregory, and Xiadong Jia. *Particle deposition and aggregation: measurement, modelling and simulation*. Butterworth-Heinemann, 2013.

[136] Laxman K Malla, Rajneesh Bhardwaj, and Adrian Neild. Analysis of profile and morphology of colloidal deposits obtained from evaporating sessile droplets. *Colloids and Surfaces A: Physicochemical and Engineering Aspects*, 567:150–160, 2019.

[137] J Bico, C Tordeux, and D Quéré. Rough wetting. *Europhysics Letters (EPL)*, 55(2):214–220, jul 2001.

[138] Yong Chae Jung and Bharat Bhushan. Dynamic effects of bouncing water droplets on superhydrophobic surfaces. *Langmuir*, 24(12):6262–6269, 2008.

[139] Tao Deng, Kripa K Varanasi, Ming Hsu, Nitin Bhate, Chris Keimel, Judith Stein, and Margaret Blohm. Nonwetting of impinging droplets on textured surfaces. *Applied Physics Letters*, 94(13):133109, 2009.

[140] Dae Hee Kwon and Sang Joon Lee. Impact and wetting behaviors of impinging microdroplets on superhydrophobic textured surfaces. *Applied Physics Letters*, 100(17):171601, 2012.

[141] Denis Bartolo, Farid Bouamrirene, Emilie Verneuil, Axel Buguin, Pascal Silberzan, and Sébastien Moulinet. Bouncing or sticky droplets: Impalement transitions on superhydrophobic micropatterned surfaces. *EPL (Europhysics Letters)*, 74(2):299, 2006.

[142] Z Wang, C Lopez, A Hirsa, and N Koratkar. Impact dynamics and rebound of water droplets on superhydrophobic carbon nanotube arrays. *Applied physics letters*, 91(2):023105, 2007.

[143] Yong Chae Jung and Bharat Bhushan. Wetting transition of water droplets on superhydrophobic patterned surfaces. *Scripta Materialia*, 57(12):1057–1060, 2007.

[144] Aurélie Lafuma and David Quéré. Superhydrophobic states. *Nature materials*, 2(7):457, 2003.

[145] Yong Chen, Bo He, Junghoon Lee, and Neelesh A Patankar. Anisotropy in the wetting of rough surfaces. *Journal of colloid and interface science*, 281(2):458–464, 2005.

[146] Fengxiang Zhang and Hong Yee Low. Anisotropic wettability on imprinted hierarchical structures. *Langmuir*, 23(14):7793–7798, 2007.

[147] Jun Young Chung, Jeffrey P Youngblood, and Christopher M Stafford. Anisotropic wetting on tunable micro-wrinkled surfaces. *Soft Matter*, 3(9):1163–1169, 2007.

[148] H Kusumaatmaja, RJ Vrancken, CWM Bastiaansen, and JM Yeomans. Anisotropic drop morphologies on corrugated surfaces. *Langmuir*, 24(14):7299–7308, 2008.

[149] Jing Yang, Felicity RAJ Rose, Nikolaj Gadegaard, and Morgan R Alexander. Effect of sessile drop volume on the wetting anisotropy observed on grooved surfaces. *Langmuir*, 25(5):2567–2571, 2009.

[150] Olesya Bliznyuk, Vasilisa Veligura, E Stefan Kooij, Harold JW Zandvliet, and Bene Poelsema. Metastable droplets on shallow-grooved hydrophobic surfaces. *Physical Review E*, 83(4):041607, 2011.

[151] Chunhong Ma, Shaoxian Bai, Xudong Peng, and Yonggang Meng. Anisotropic wettability of laser micro-grooved sic surfaces. *Applied Surface Science*, 284:930–935, 2013.

[152] R Kannan and D Sivakumar. Drop impact process on a hydrophobic grooved surface. *Colloids and Surfaces A: Physicochemical and Engineering Aspects*, 317(1-3):694–704, 2008.

[153] John T Pearson, Daniel Maynes, and Brent W Webb. Droplet impact dynamics for two liquids impinging on anisotropic superhydrophobic surfaces. *Experiments in fluids*, 53(3):603–618, 2012.

[154] V Vaikuntanathan and D Sivakumar. Transition from cassie to impaled state during drop impact on groove-textured solid surfaces. *Soft matter*, 10(17):2991–3002, 2014.

[155] Visakh Vaikuntanathan and D Sivakumar. Maximum spreading of liquid drops impacting on groove-textured surfaces: effect of surface texture. *Langmuir*, 32(10):2399–2409, 2016.

[156] Ken Yamamoto, Hideyuki Takezawa, and Satoshi Ogata. Droplet impact on textured surfaces composed of commercial stainless razor blades. *Colloids and Surfaces A: Physicochemical and Engineering Aspects*, 506:363–370, 2016.

[157] Paola G Pittoni, Ya-Chi Lin, and Shi-Yow Lin. The impalement of water drops impinging onto hydrophobic/superhydrophobic graphite surfaces: the role of dynamic pressure, hammer pressure and liquid penetration time. *Applied Surface Science*, 301:515–524, 2014.

[158] Hyuk-Min Kwon, Adam T Paxson, Kripa K Varanasi, and Neelesh A Patankar. Rapid deceleration-driven wetting transition during pendant drop deposition on superhydrophobic surfaces. *Physical review letters*, 106(3):036102, 2011.

[159] Olive G Engel. Waterdrop collisions with solid surfaces. *Journal of research of the national bureau of standards*, 54(5):281–298, 1955.

[160] Yunyun Quan and Li-Zhi Zhang. Numerical and analytical study of the impinging and bouncing phenomena of droplets on superhydrophobic surfaces with microtextured structures. *Langmuir*, 30(39):11640–11649, 2014.

[161] M Reyssat, JM Yeomans, and D Quéré. Impalement of fakir drops. *EPL (Europhysics Letters)*, 81(2):26006, 2007.

[162] Neelesh A Patankar. Consolidation of hydrophobic transition criteria by using an approximate energy minimization approach. *Langmuir*, 26(11):8941–8945, 2010.

[163] CW Extrand. Criteria for ultralyophobic surfaces. *Langmuir*, 20(12):5013–5018, 2004.

[164] Denis Richard, Christophe Clanet, and David Quéré. Surface phenomena: Contact time of a bouncing drop. *Nature*, 417(6891):811, 2002.

List of Publications

Journals

1. Malla, Laxman K., Patil, Nagesh D., Bhardwaj, Rajneesh, and Neild Adrian (2017). Droplet Bouncing and Breakup during Impact on a Microgrooved Surface, *Langmuir*, 33, 9620-9631.

2. Malla, Laxman K., Bhardwaj, Rajneesh and Neild, Adrian (2019). Analysis of Profile and Morphology of Colloidal Deposits obtained from Evaporating Sessile Droplets, *Colloids and Surfaces A: Physicochemical and Engineering Aspects*, 567: 150-160

3. Malla, Laxman K., Bhardwaj, Rajneesh and Neild, Adrian (2019). Colloidal Deposit of an Evaporating Sessile Droplet on a Nonuniform Heated Substrate, *Colloids and Surfaces A: Physicochemical and Engineering Aspects*, doi: 10.1016j.colsurfa2019.124009

Conferences

1. Malla, Laxman K., Bhardwaj, Rajneesh and Neild, Adrian, “Coffee-ring" Width Modification due to Temperature Gradient on the Substrate, *Droplets 2019 conference, Durham, UK.*

2. Malla, Laxman K., Bhardwaj, Rajneesh and Neild, Adrian, Effect of Temperature Gradient on the Substrate on the Coffee-ring Dimensions, *71st Annual Meeting of the APS Division of Fluid Dynamics*, 2018.

3. Malla, Laxman K., and Bhardwaj, Rajneesh , Droplet Impact Dynamics on Hydrophobic Microgrooved Surfaces, *24th National and 2nd International ISHMT-ASTFE Heat and Mass Transfer Conference(IHMTC-2017)*, 2017.

4. Malla, Laxman K. and Bhardwaj, Rajneesh , Evaporation Dynamics of Sessile Droplets of Water-Based Graphene Nanoplatelets: Effect of Concentration and Substrate Heating, *44th National Conference on Fluid Mechanics and Fluid Power*, 2017.